Measurement of the nucleon structure function in iron using 215- and 93-GeV muons

P. D. Meyers,* A. R. Clark, K. J. Johnson,† L. T. Kerth, S. C. Loken, T. W. Markiewicz,‡
W. H. Smith,§ M. Strovink, and W. A. Wenzel
Physics Department and Lawrence Berkeley Laboratory, University of California, Berkeley, California 94720

R. P. Johnson, C. Moore, M. Mugge,** and R. E. Shafer
Fermi National Accelerator Laboratory, Batavia, Illinois 60510

G. D. Gollin, F. C. Shoemaker, and P. Surko††
Joseph Henry Laboratories, Princeton University, Princeton, New Jersey 08544
(Received 6 August 1985)

We have measured the inclusive deep-inelastic scattering of muons on nucleons in iron using beams of 93- and 215-GeV muons. To perform this measurement, we have built and operated the multimuon spectrometer (MMS) in the muon beam at Fermilab. Using the known form of the radiatively corrected electromagnetic cross section, we extract the structure function $F_2(x,Q^2)$ with a typical precision of 2% over the range $5<Q^2<200$ GeV$^2/c^2$. We compare our measurements to the predictions of lowest-order quantum chromodynamics (QCD) and find a best-fit value of the QCD scale parameter $\Lambda_{\rm LO}=230\pm40(\text{stat})\pm80(\text{syst})$ MeV/c, assuming $R=0$ and without applying Fermi-motion corrections. Comparing the cross sections at the two beam energies, we measure $R=-0.06\pm0.06(\text{stat})\pm0.11(\text{syst})$. Our measurements show qualitative agreement with QCD, but quantitative comparison is hampered by phenomenological uncertainties. The experimental situation is quite good, with substantial agreement between our measurements and those of others.

I. PROBING THE STRUCTURE OF MATTER

Since the first decade of this century, the electromagnetic scattering of pointlike particles has shown us the structure of atoms and the existence of the atomic nucleus,[1-3] the structure of the atomic nucleus and its size,[4] and the structure of the nucleon and the existence of partons,[5,6] later to be identified with quarks. More recently, a continuing series of experiments in the deep-inelastic region has been directed toward developing an understanding of the strong interactions of the quarks. The experiment recorded here continues this investigation, using the principle essentially unchanged since 1909, but at a scale 10^5 times smaller.

A. Kinematics

The Feynman diagram for deep-inelastic lepton-hadron scattering in the lowest order of QED is shown in Fig. 1, together with a summary of our kinematical notation. To this order, the process is described as the exchange of one virtual photon. QED allows us to calculate unambiguously what happens at the leptonic (upper) vertex. The goal of our experiment is to uncover what happens in the region surrounding the hadronic vertex. We will be studying inclusive scattering, $\mu N\to\mu X$, with no reference to any particular hadronic final state. This means that the only relevant four-vectors at the hadronic vertex are p and q, and the only Lorentz-invariant quantities are q^2 and $p\cdot q$ (and $p^2=M_N{}^2$). While isolating the hadronic vertex is a productive move toward understanding the scattering process, experimentally it is important to note that these quantities can be measured using only the initial and final muons:

$$Q^2\equiv -q^2=4EE'\sin^2\frac{\theta}{2}\ ,$$
$$\nu\equiv p\cdot q/M_N=E-E'\ , \tag{1}$$

where E, E', and θ are the initial and final muon energies and the muon scattering angle as measured in the laboratory frame (the target rest frame). Terms containing the lepton mass have been neglected. Another useful quantity is the invariant mass of the hadronic final state:

$$W^2=(p+q)^2=M_N{}^2+2M_N\nu-Q^2\ .$$

The elastic limit is $W^2=M_N{}^2$ or $Q^2=2M_N\nu$. Resonances appear at fixed W^2 near this limit. Figure 2 shows the region of the Q^2-ν plane accessible to inelastic scattering at fixed incident energy E.

It is convenient to describe another set of variables that are Q^2 and ν scaled by their maximum values, neglecting lepton masses:

$$x=Q^2/2M_N\nu\le 1\ ,$$
$$y=\nu/E\le 1\ , \tag{2}$$
$$v=Q^2/2M_NE=xy\ .$$

B. Cross section and structure functions

By demanding Lorentz covariance and gauge invariance we can translate[7,8] the diagram of Fig. 1 directly into an expression for the spin-averaged inclusive cross section:

 ©1986 The American Physical Society

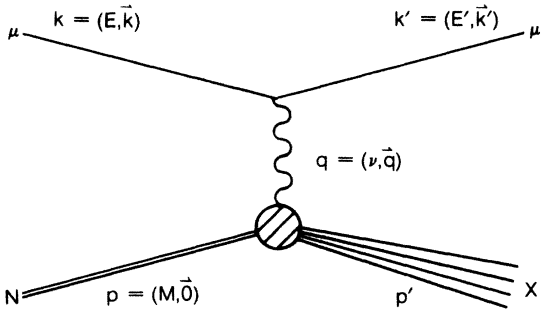

FIG. 1. Deep-inelastic μN scattering, showing our notation for the four-momenta and their representation in the laboratory frame.

$$\frac{d^2\sigma}{dE'd\Omega'}=\frac{EE'}{\pi}\frac{d^2\sigma}{dQ^2d\nu}$$
$$=\frac{4\alpha^2E'^2}{Q^4}\left[2W_1(Q^2,\nu)\sin^2\frac{\theta}{2}+W_2(Q^2,\nu)\cos^2\frac{\theta}{2}\right], \quad (3)$$

in terms of the two unknown "structure functions" W_1 and W_2, scalar functions that describe the hadronic electromagnetic current.

Further enlightenment comes from a complementary approach to the same process.[9] We treat the incident muon as a source of virtual photons and write the cross section as $d\sigma=\sum_\epsilon d\Gamma_\epsilon\sigma_\epsilon$, where Γ_ϵ and σ_ϵ are the flux and absorption cross section, respectively, for virtual photons of polarization ϵ. Using the Feynman rules for the reduced diagram of $\gamma^*N\to X$, we find

$$\sigma_T=\frac{4\pi^2\alpha}{K}W_1,\quad \sigma_L=\frac{4\pi^2\alpha}{K}\left[W_2\left[1+\frac{\nu^2}{Q^2}\right]-W_1\right], \quad (4)$$

where T and L refer to transversely and longitudinally polarized virtual photons and K is a flux factor. Defining $R\equiv\sigma_L/\sigma_T$ we can eliminate W_1 in favor of R in the cross section Eq. (3). The advantages of this substitution will be described in Sec. IC where it is shown that for some cases of interest R is expected to be small. For now we record the cross section in its new form:

$$\frac{d^2\sigma}{dQ^2d\nu}=\frac{4\pi\alpha^2}{Q^4}\left[1-y+\frac{y^2+2M_Nxy/E}{2(R+1)}-\frac{M_Nxy}{2E}\right]\times W_2(Q^2,\nu)$$
$$\approx\frac{4\pi\alpha^2}{Q^4}\left[1-y+\frac{y^2}{2(R+1)}\right]W_2(Q^2,\nu). \quad (5)$$

The approximate form comes from taking the Bjorken limit where energies $(E,Q^2,\nu)\to\infty$ with x and y finite.[10] In the kinematic region covered by our data, making such an approximation has a maximum effect of $<\frac{1}{3}\%$ on our measured structure function.

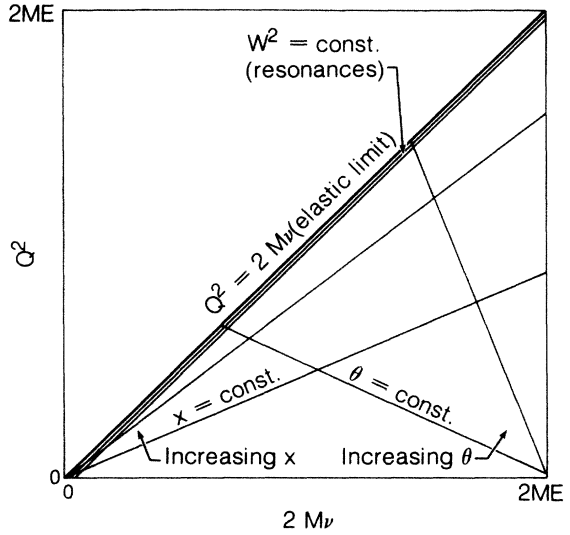

FIG. 2. Deep-inelastic-scattering kinematics. The region below the diagonal is accessible. Lines of constant W^2, x, and θ are indicated.

C. The parton model

In the parton model, the process of Fig. 1 is understood as the incoherent sum of diagrams such as Fig. 3. The nucleon is resolved into a swarm of pointlike partons, one of which is responsible for the scattering. During the scattering the parton is assumed to be free. If the parton has spin $\frac{1}{2}$, the virtual photon-parton vertex is calculated exactly as the lepton vertex was. Our ignorance about strong interactions is now relegated to the processes that determine the spectrum of partons in the nucleon and produce the splash of hadrons in the final state.

The parton model gives an interpretation of the structure functions. We consider the process in the frame where the nucleon momentum is large.[6] We neglect the transverse momentum and mass of the partons and assign to each parton of type i a fraction of the nucleon's momentum x_i from the unknown distribution $f_i(x_i)dx_i$. Because the lepton-parton scatter is elastic, we are left with the elastic-scattering condition in the form

$$\delta(2p_i\cdot q+q^2)=\delta(2x_ip\cdot q-Q^2)=\frac{1}{M_N\nu}\delta(x_i-x), \quad (6)$$

where $x=Q^2/2M_N\nu$ [see Eq. (2)]. The measurable quantity x is thus the fractional momentum of the struck parton.

We now calculate the matrix elements, assuming the partons to be pointlike Dirac particles and find

$$F_1(x)\equiv M_NW_1(Q^2,\nu)=\tfrac{1}{2}\sum_i f_i(x)e_i^2,$$
$$F_2(x)\equiv\nu W_2(Q^2,\nu)=\sum_i xf_i(x)e_i^2. \quad (7)$$

The structure functions F_i are seen to be functions of x only, with e_i the charge of type-i partons in units of the proton charge. This property is known as "scaling"[10] and is observed experimentally.[5]

Another property apparent from Eq. (7) is the relation

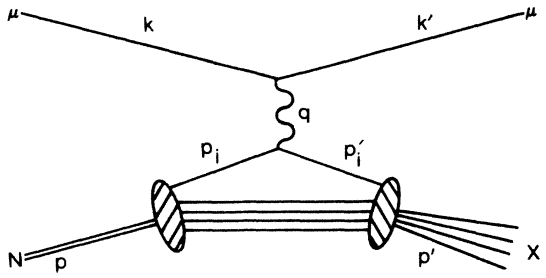

FIG. 3. The parton-model picture of deep-inelastic scattering.

$F_2(x)=2xF_1(x)$. This is known as the Callan-Gross relation.[11] Inspection of Eq. (4) shows that, in the Bjorken limit ($\nu^2/Q^2\to\infty$ with x fixed), the Callan-Gross relation implies $R=0$. For scalar partons, $\sigma_T=0$ and $R=\infty$. Allowing finite parton masses m_i and transverse momenta modifies these conclusions[12] and leads to corrections of order $(m_i^2+p_{i\perp}^2)/Q^2$.

To summarize, in the parton model, a measurement of $F_2(x)$ is a determination of the momentum distribution of partons in the target nucleon—the nucleons's "structure" in momentum space. A measurement of R yields information on the spin of the partons themselves.

D. Quantum chromodynamics

The theory of the strong interactions of partons, now identified with quarks, the numerical building blocks of hadrons, was developed in analogy to QED, with an internal quantum number called "color" taking the part of the electric charge. The resulting theory is known as quantum chromodynamics (QCD). The primary difference between QCD and QED is that, while photons are neutral, the "gluons" of QCD carry color and thus couple directly to one another. As a result, if we include Q^2-dependent terms in the renormalized coupling constant we find

$$\alpha_S(Q^2)=\frac{\alpha_S(\mu^2)}{1+[(33-2N_f)/12\pi]\alpha_S(\mu^2)\ln(Q^2/\mu^2)}\ , \tag{8}$$

where μ^2 is an arbitrary renormalization point and N_f is the number of quark flavors (up, down, strange, etc.). For $N_f<17$, the coupling constant gets weaker as Q^2 increases, a property known as "asymptotic freedom."[13] This expression for α_S is an approximation based on ignoring terms of the order $\ln[\ln(Q^2/\mu^2)]$ and is thus known as the "leading-logarithm" approximation. We can remove the reference to the arbitrary renormalization point μ in Eq. (8) by introducing the parameter Λ such that

$$\alpha_S(Q^2)=\frac{12\pi}{(33-2N_f)\ln(Q^2/\Lambda^2)}\ . \tag{9}$$

While μ was arbitrary, Λ is defined by Eq. (9) and is measurable. Other definitions of Λ differ from this one in the next order of α_S (Ref. 14). Keeping the next-to-leading logarithm gives such a correction. For this reason, Λ as defined in Eq. (9) is sometimes called $\Lambda_{\rm LO}$ for "lowest order."

Asymptotic freedom allows the understanding of the quasifree appearance of partons in nucleons, despite our apparent inability to produce free quarks—as in QED, the renormalized coupling is indeed small. This permits meaningful perturbation series calculations for strong interactions at large Q^2. At the low-Q^2 end, it is thought, but has not been proven, that the increasing α_S is a sign that the QCD interaction between quarks is *confining*, meaning that free quarks cannot be separated from their parent hadrons. Even without such proof, it is clear from Eq. (9) that perturbative QCD cannot work at low Q^2. For this reason, perturbative QCD cannot give predictions for such static properties of hadrons as the x distribution of partons. With low-Q^2 information as input, however, QCD can calculate the Q^2 dependence of such quantities. (Recall that the parton model predicts scaling, that is, no Q^2 dependence at fixed x.)

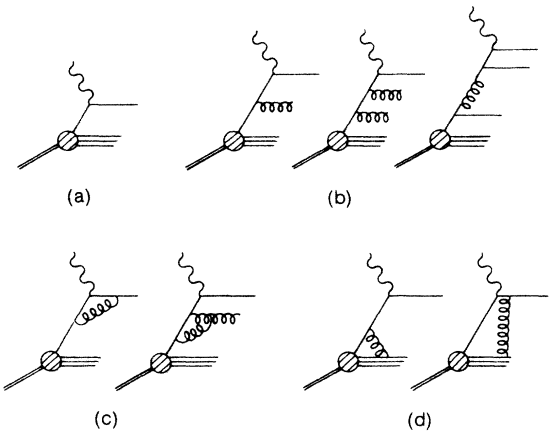

FIG. 4. QCD modifications to the parton model diagram (a) for deep-inelastic scattering. (b) Logarithmic Q^2 evolution; (c) renormalization; (d) "higher twist."

The most direct prediction of QCD (Ref. 15) is not of the Q^2 evolution of parton distributions, but rather of moments of those distributions. Fortunately, Altarelli and Parisi[16] have given a more direct interpretation of QCD's predictions, an interpretation that is a natural ex-

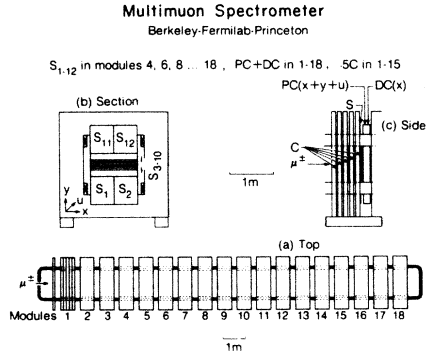

FIG. 5. The multimuon spectrometer (MMS). (a) Top view, showing the arrangement of iron plates into modules and the magnet coils running the length of the stack. (b) Section, looking into the beam, showing the coils in their slots, our coordinate system, and a trigger scintillator hodoscope. Paddles $S_{1,2,11,12}$ are used to signal a scattered muon, while staves S_{3-10} serve as a beam veto. (c) Side view of one module—detailed in Fig. 7.

tension of the parton model. Figure 4(a) shows the parton-model diagram for deep-inelastic scattering via a virtual photon. Allowing the partons to interact generates processes such as those in Figs. 4(b)–4(d). These processes rob from the momentum fraction x carried by the struck parton. We therefore expect that these processes will reduce the structure function at large x and increase it at small x. Increasing Q^2 resolves finer and finer structure of this type, but asymptotic freedom slows the evolution, leaving soft (logarithmic) scaling violations. The method of Altarelli and Parisi accounts for the processes in Fig. 4(b) by writing a set of transportlike differential equations for the parton distribution functions. Starting at some reference $Q^2=Q_0^2$ and defining $t\equiv\ln(Q^2/Q_0^2)$,

$$\frac{d\sum_{i=1}^{2N_f} f_i(x,t)}{dt}=\frac{\alpha_S(t)}{2\pi}\int_x^1\frac{dy}{y}\left[\sum_{i=1}^{2N_f} f_i(y,t)P_{qq}\left[\frac{x}{y}\right]+2N_f G(y,t)P_{qG}\left[\frac{x}{y}\right]\right],$$
$$\frac{dG(x,t)}{dt}=\frac{\alpha_S(t)}{2\pi}\int_x^1\frac{dy}{y}\left[\sum_{i=1}^{2N_f} f_i(y,t)P_{Gq}\left[\frac{x}{y}\right]+G(y,t)P_{GG}\left[\frac{x}{y}\right]\right]. \tag{10}$$

The sum is over quark + antiquark flavors, and couplings are assumed to be flavor independent. $G(x,t)$ is the distribution of gluons in the nucleon as a function of momentum fraction x. We have anticipated our use of a nuclear target with a nearly equal mix of protons and neutrons. This leads to a mixture of quarks which is nearly a flavor singlet. Since the gluon is also a flavor singlet, there is coupling between the quark and gluon evolutions. The interpretation of Eqs. (10) is quite straightforward. The $P(z)$'s represent the probabilities of the processes where a daughter parton (either quark or gluon) is split from a parent parton, taking a fraction z of its momentum. Thus partons of momentum fraction x [the left-hand sides of Eq. (10)] come from partons of larger momentum fraction y with probability $P(x/y)$.

The diagrams of Figs. 4(c) and 4(d) still remain. Those such as that of Fig. 4(c) are taken into account automatically. They either cancel infrared divergences from the emission of soft real gluons and are handled by renormalization, or are contributions to the running coupling constant and thus are included in the leading-logarithm approximation by using $\alpha_S(Q^2)$ (Ref. 17). The diagrams in Fig. 4(d) are another story. Although not calculable in detail, their general behavior is known. Since they involve interactions with more than one target quark, they resemble elastic scattering, where multiple-gluon exchanges are required to keep the recoiling nucleon intact. This leads to a form factorlike suppression which goes as powers of $1/Q^2$. At sufficiently large Q^2, the logarithmic behavior discussed above should dominate these terms, which bear the name "higher twist."

To test the predictions of QCD, one can measure the structure function as a function of Q^2 for various fixed values of x. This Q^2 dependence or scaling violation can be compared to QCD by using the measured x dependence at a fixed $Q^2=Q_0^2$ as the initial condition and integrating Eq. (10) to get predicted values of the structure function for all Q^2. For the singlet case, it is also necessary to have $G(x,Q_0^2)$, the initial condition for the gluon evolution. This distribution is not directly measurable. Neutrinos, however, are sensitive to the difference between quarks and antiquarks. With this essentially nonsinglet information, various QCD and phenomenological parameters can be determined without complications from gluons. With these values fixed, the singlet structure functions can be used to extract the gluon distribution.[18] A hypothetically more direct but experimentally more difficult approach would be to use the production of heavy flavors in the "photon-gluon fusion" process to tag interactions with gluons.[19]

E. Grand unified theories

With the weak and electromagnetic interactions unified and understood as one gauge theory with a spontaneously broken symmetry[20] and with QCD as a candidate for the field theory of the strong interactions, it was immediately hoped that they could be combined into a "grand unified theory" (GUT). In a typical GUT (for a review, see Ref. 21) quarks and leptons are placed in the same representation of a group [SU(5) for the simplest theory[22]]. The mass scale M_X above which symmetry between quarks and leptons is restored is determined by following the various running coupling constants up to the energy where they become equal. Using α and α_S for this determination in one of the simpler models gives[21]

$$M_X\approx 15\times 10^{14}\Lambda\ . \tag{11}$$

The symmetry that allows transitions between leptons and quarks implies that baryon number is not conserved and hence protons are no longer stable. The predicted proton lifetime is

$$\tau_p\propto\frac{1}{\alpha_{\rm GUT}}\frac{M_X{}^4}{M_p{}^5}\approx 5\times 10^{32}[\Lambda\ ({\rm GeV})]^4\ {\rm yr}\ , \tag{12}$$

with over an order of magnitude of theoretical uncertainty. Although GUT's have had some theoretical successes, the prediction of proton decay is one of the few that may be verifiable. Early determinations of Λ indicated values on the order of several hundred MeV. The resulting proton lifetimes were above, but close to, existing experimental lower limits of $\approx 10^{29}$ yrs (Ref. 23). A new generation of proton decay experiments designed to probe the GUT regime is in progress. Results from one of these experiments[24] for the decay mode $p\rightarrow e^+\pi^0$ yield limits in con-

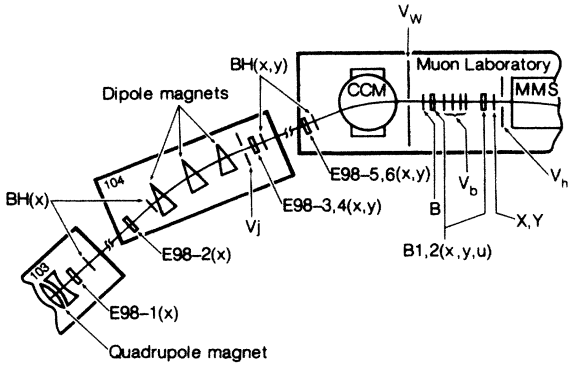

E98-n, B1, B2	Multiwire proportional chambers
BH,X,Y	Beam scintillator hodoscope
V_j	"Jaw" veto counter
V_W	Large veto wall
B	Beam-defining scintillator
V_h	Halo veto hodoscope
V_b	Bucket-occupancy veto counter
MMS	Multimuon Spectrometer
CCM	Chicago Cyclotron Magnet

FIG. 6. The beam-monitoring system used to define a valid beam muon and determine its momentum. Not to scale.

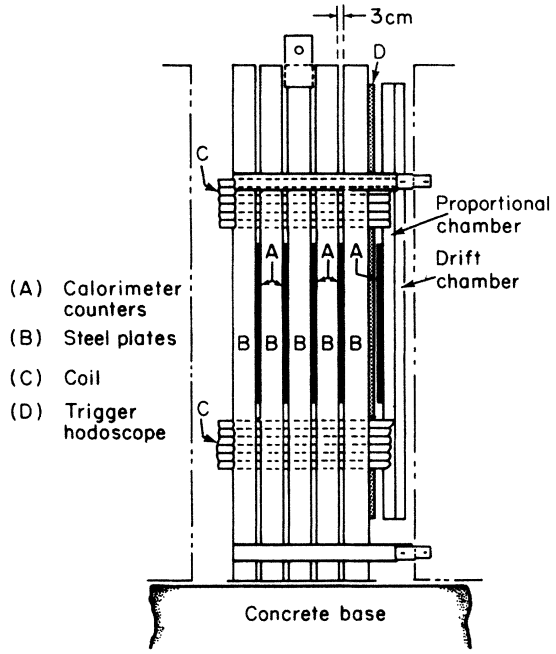

FIG. 7. An MMS module showing the location of the calorimeter scintillators and a large-gap instrumentation package including a trigger hodoscope, a proportional chamber, and a drift chamber.

flict with the simplest GUT models. The fourth-power dependence of τ_p on Λ makes a reliable determination of Λ essential to the confrontation of theory with experiment.

II. THE MULTIMUON SPECTROMETER

A. Design constraints

Our goal is to measure the nucleon structure function $F_2(x,Q^2)$ over as large a range of Q^2 as possible, without being forced to include the nonperturbative very low Q^2 region. The kinematic limit, $Q^2<2M_NE$ [see Eq. (2)], requires us to have a high-energy lepton beam. The desire to reach $Q^2>100$ GeV$^2/c^2$ rules out existing electron beams, so we use the high-energy muon beam at Fermilab. The virtual-photon propagator suppresses the large-Q^2 cross section like $1/Q^4$. To reach high Q^2 we must therefore have high luminosity. We achieve high luminosity by using a beam of moderate intensity incident on a long, heavy target. To maintain high acceptance throughout the long target, the target and the spectrometer used to analyze the final state are integrated into one package. The high magnetic fields required for momentum analysis above 100 GeV/c and the large magnetized volume require an iron magnet.

Along with deep-inelastic scattering, the experiment is designed to observe multimuon final states: $\mu N\rightarrow\mu\mu X$, $\mu\mu\mu X$, etc. This imposes three constraints: suppression of low-mass electromagnetically produced muon pairs; observation at the lower Q^2's typical of multimuon production (a few GeV$^2/c^2$), and thus at smaller scattering angles; and suppression of secondary muons from pion and kaon decay in hadronic showers. To meet the first requirement, we use a Cartesian geometry with a uniform vertical magnetic field for momentum analysis. Muon trajectories bend (and muon pairs separate) in the horizontal plane. For pair mass discrimination we demand a minimum vertical opening angle, which is unaffected by the magnetic separation. When the large ($\approx$20 cm) size of the beam is folded in, the second constraint requires that the spectrometer be active in the beam region and therefore that the magnetic field extend uniformly to the center of the beam. This dictates that the target material be the same iron used in the magnet. This target must be densely packed along the beam direction to suppress π and K decay.

The result is the multimuon spectrometer (MMS) illustrated in Fig. 5. The MMS is a horizontal stack of 91 4-inch-thick steel plates, each 8 ft on a side. The stack is magnetized by coils running the length of the stack through slots cut in the plates. The iron serves as target, analyzing magnet, hadron absorber/muon identifier, and hadron calorimetry medium. The spectrometer is instrumented with multiwire proportional and drift chambers for recording muon trajectories and with plastic scintillation counters for triggering and calorimetry. Also shown in Fig. 5 is our coordinate system, with z in the beam direction, x horizontal, and y up. The various components of the MMS are described in the remaining parts of this section.

B. The muon beam

The Fermilab muon beam has been described elsewhere.[25] Our beam instrumentation is shown in Fig. 6. Experiments using the Chicago cyclotron magnet (CCM) ran simultaneously with the MMS, which was positioned along the CCM-deflected beam line. The last dipole and the CCM were instrumented with multiwire proportional

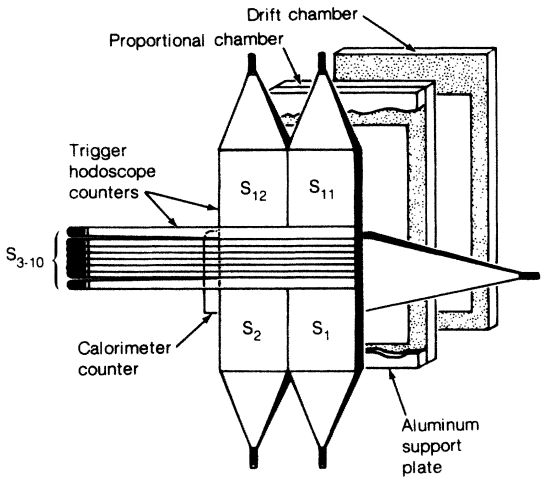

FIG. 8. A large-gap instrumentation package. Trigger hodoscopes were located in even numbered gaps only, starting with module 4.

chambers (MWPC's) and scintillator hodoscopes (E98-1, . . . , 6, BH) giving four horizontal (x) and two vertical (y) measurements. These, in conjunction with two MWPC's (B1 and B2) measuring x, y, and a diagonal (u) coordinate located in front of the MMS, were used to determine the momentum of individual beam muons, ideally to better than 0.5% (σ_p/p). In reality, the situation was complicated by material placed in the beam by the upstream experiment, including borax (to clean up the beam) and a lead-glass shower counter 20.5 radiation lengths thick. With enough MWPC information we could fit the Coulomb scattering angle in the lead glass, but at the cost of redundancy in the momentum fit. Energy loss in material upstream of the MMS could be corrected for in an average sense only. Straggling was accounted for by including it in the simulation used for acceptance and resolution modeling (see Sec. V).

A system of scintillator hodoscopes (see Fig. 6) was used to define the beam size and choose usable beam muons. The last focus of the beam was in the aperture of the last beam line dipole. At the front of the MMS, the counter B and the hodoscopes X and Y defined the beam to be 35.1 cm (x) by 22.9 cm (y). A usable muon was defined to be one unaccompanied by a second muon, either in or out of the beam. The muon beam retained the 53-MHz signature of the synchrotron, leading to a time structure of 18.9 ns "rf buckets." Signals from counter B were put into advanced or delayed anticoincidence to veto muons which had another muon in either the preceding or following bucket. If another muon was in bucket ± 2 or ± 3, the track was used but tagged. Tracks with accompanying muons in the same bucket were rejected on the basis of pulse-height information from scintillators B and V_b, and from hodoscope information from X and Y. A $1.4\times$minimum ionizing signal from any three of the five pulse heights, or more than one count in either hodoscope plane vetoed the track. Muons out of the defined beam area are known as "halo." In the Fermilab muon beam, total intensity outside our defined beam was roughly equal to the intensity in the beam. Beam muons with an in-time halo muon were rejected by three layers of veto scintillators, one at V_W and two at V_h. The signal for a usable beam track was called BV (for "vetoed beam"). BV was required in coincidence with all physics triggers, and a prescaled number, typically 1/350 000, was recorded with no further trigger requirements for calibration and use as an unbiased input for the simulation programs.

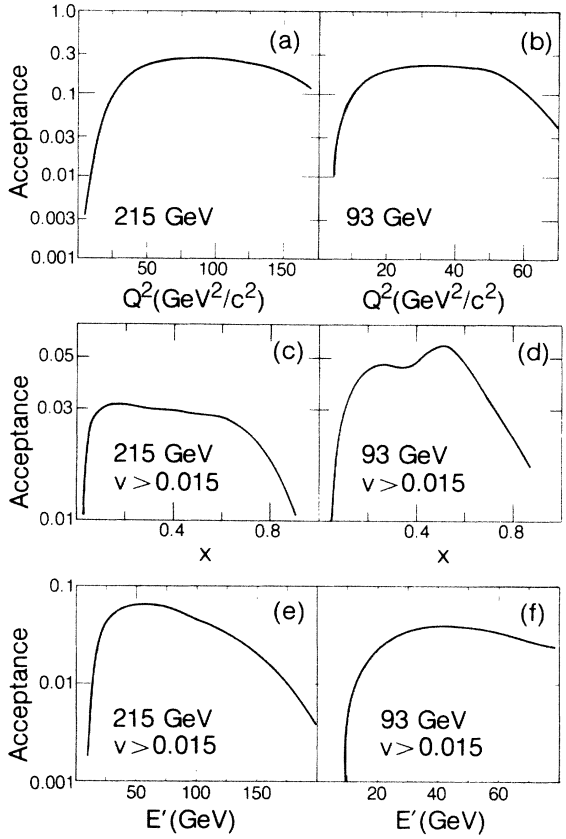

FIG. 9. MMS acceptance at 215 and 93 GeV vs Q^2 (a), (b); x (c), (d); and E' (e), (f).

The intensity of the muon beam was $\approx 3\times 10^6$ muons per pulse or a bucket occupancy probability of 0.07. The vetoes rejected from $\frac{1}{3}$ to $\frac{1}{2}$ of the muons, leaving a usable flux of $(1.5\text{–}2)\times 10^6$ muons per pulse. For μ^- running, the beam intensity was a factor of 3 lower, but the lower intensity meant less veto rejection, giving a usable flux of around 0.9×10^6/pulse.

C. Target and magnet

The 91 steel plates of the multimuon spectrometer had an average thickness of 10.28 cm. The plates were grouped into 18 modules of five, with 3-cm gaps separating the plates. The remaining plate, known as plate 0, was placed at the front of the stack where the last plate of an otherwise nonexistent module 0 would have been. Following each module was a large gap for the insertion of an instrumentation package. This package was designed to be as thin as possible to minimize total module length and thus maximize high-Q^2 acceptance and average target density. The large gaps were typically 25.4 cm thick. This dimension was adjusted to give a module length of 88.90 ± 0.04 cm. A module with instrumentation is shown in Fig. 7. The mass of the entire spectrometer was

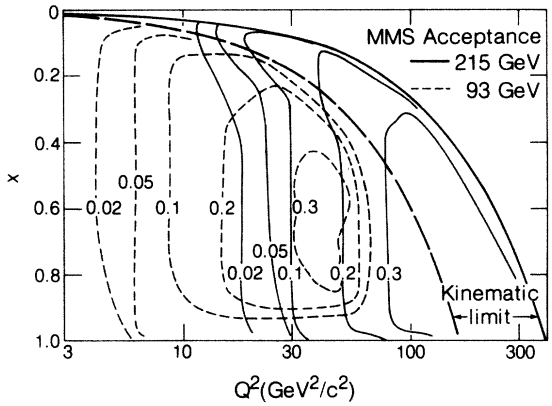

FIG. 10. Contours of constant MMS acceptance vs Q^2 and x. The x axis origin is at the top to facilitate comparison with the $F_2(x,Q^2)$ plots of Sec. VII. Solid (dashed) contours are for a beam energy of 215 (93) GeV.

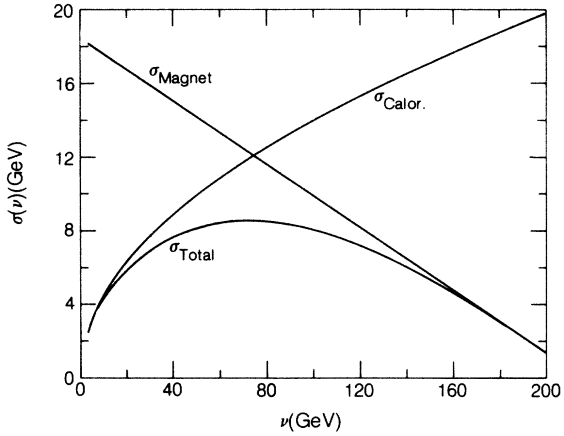

FIG. 11. Calorimeter and magnetic resolution in ν showing the improvement possible at low ν using the direct calorimetric measurement.

4.3×10^5 kg or 475 tons.

The target was restricted by trigger geometry to be the first 13 modules plus plate 0. This gave 678.3 cm or 5.34 kg/cm^2 of iron. Including scintillator, chambers, and support structures gave a total target thickness of 5.61 ± 0.01 kg/cm^2, where the error is combined uncertainty due to measurement error in the plate thickness and an estimate of uncatalogued material in the beam. This target thickness and our integrated flux of muons gave the experiment a sensitivity of nearly 1 event/femtobarn for unit acceptance.

The iron target was magnetized by 4000 A$\times$18 turns of water-cooled copper running the entire length of the MMS through slots cut in the plates. The configuration and shape of the slots were designed to give an approximately uniform vertical magnetic field in the 107-cm wide by 179-cm high active area filling the region between the coils. The MMS was run for roughly equal durations in both field polarities to help cancel any systematic left-right asymmetries in the apparatus. The polarity was typically changed once a day.

The magnetic field was mapped and calibrated using three sets of measured information. Flux loops spanning 12 sections of each module and one large loop enclosing the entire magnet gave absolute measurements of the flux of **H** in the iron. Hall-probe and flip-coil measurements between plates mapped the x and y components of **B** in the air gaps. Precision measurements of iron samples removed from the coil slots gave B vs H (Ref. 26). These measurements were turned into an absolutely calibrated field map for the MMS by constraining the field to agree with both the measurements (used as boundary conditions) and the Maxwell equations.[27] The field integral for an average module was 9.998×10^5 G cm for an average field of 11.25 kG (19.46 kG in the iron). The field was mapped to 0.2% and observed to be uniform to 3% in the active region of the spectrometer.

D. Trigger

Trigger hodoscopes of 12 scintillation counters were located after each even numbered module starting with module 4. There were eight trigger banks in all, separated by 102.8 cm of iron. Figure 8 shows a trigger bank, along with the rest of a large-gap instrumentation package. The central section of each trigger bank was a set of six narrow staves, each 3.9 cm high and extending the width of the active area. These staves covered the beam region and were used primarily for multimuon triggering. Above and below the set of narrow staves was a single wide (15.2-cm) stave. These, along with the narrow staves, made up the beam veto for the deep-inelastic-scattering trigger. The regions above and below the staves were each divided vertically into two "paddles." These paddles, each 60.5 cm high by 52.7 cm wide, signaled the presence of a scattered muon. The deep-inelastic trigger required a signal from any paddle and no signal in the beam veto (staves) in each of three or more consecutive trigger banks. There was no requirement made on hadronic energy deposition. The eight trigger banks made up six overlapping subtriggers of three banks each. These operated independently and a signal from any of them in coincidence with a BV signal from the beam logic created a full trigger signal which initiated the readout of the spectrometer information and the recording of an event. Along with chamber and calorimeter information, the logical status of each trigger and beam counter and each subtrigger were recorded. The trigger rate for the deep-inelastic trigger was 3×10^{-6} per usable beam muon.

The wide staves between the paddles and the beam region imposed a minimum vertical scattering angle requirement of 12 mr. This minimum could be reached only by a scatter in module 1 triggering the last subtrigger. Moving the interaction vertex downstream increased the minimum accepted scattering angle. The acceptance of the MMS in Q^2, x, and E', averaged over the length of the spectrometer, is shown for beam energies of 93 and 215 GeV in Fig. 9. Since the cross section goes to infinity and the acceptance goes to zero as $Q^2\rightarrow0$ the absolute value of the acceptance for a kinematic region that includes very low Q^2 is arbitrary. The plots assume $v>0.015$, or $Q^2>2.5$, 5.9 GeV$^2/c^2$ for the two beam energies. Figure 10 shows the acceptance in the Q^2-x plane. All of these results are from the Monte Carlo simulation discussed in Sec. V.

The deep-inelastic trigger was relatively free from background. The primary source of nonphysics background, that is, triggers not involving an actual scattered muon, was a stopping or decaying beam muon (to give a BV signal, yet avoid the beam-vetoing staves) in coincidence with a halo muon, lobbed over or under the halo veto and entering the MMS from the top or bottom, directly into the paddles. The chief source of this component of the halo was believed to be otherwise harmless halo muons deflected back toward the beam by the return yoke of the Chicago cyclotron magnet. Approximately 1.6% of the triggers were from this source. They were easily eliminated in analysis by the failure of the beam and "scattered" tracks to meet at a consistent vertex.

During the data analysis, we discovered that some of the paddle counters were quite inefficient. Worse, the inefficiency was spatially nonuniform. Since the x and y positions of a track at the back of the MMS translate quite directly into E' and θ due to the Cartesian geometry of the spectrometer, this position-dependent efficiency was a serious problem. Fortunately, the redundant nature of the trigger with its overlapping subtriggers allowed us to use the data to map the trigger efficiency completely (Sec. IV C). The stave counters were measured to be $>99\%$ efficient.

E. Proportional and drift chambers

Muon trajectories in the MMS were determined from positions measured after every module in packages containing three multiwire-proportional-chamber (PC) planes and one drift-chamber (DC) plane (see Figs. 5, 7, and 8). The PC planes measured x, y, and a diagonal u coordinate; the DC's measured x only. There were 19 such packages, including one following plate 0, and the entire system contained over 14 000 channels. The chambers covered an area 106.7 cm wide by 178.8 cm high, slightly larger than that covered by the trigger hodoscopes.

Details on the PC design and construction are given by Markiewicz.[19] A trigger signal opened a 70-ns write gate, and chamber signals arriving during this interval were latched to await readout by the computer. The resolution of the PC's was close to the expected $\sigma=$ (wire spacing$/\sqrt{12}$) or 920 μm and 1500 μm for the sense and induced planes. The sense planes, which measured positions in the magnetic bending direction and thus momentum, were designed to give sufficient position resolution so that the multiple Coulomb scattering (MCS) in the 29 radiation lengths between chambers would limit momentum resolution for average length tracks at the highest momenta. The efficiency of the PC's was $>90\%$ away from the beam. However, at our high intensities the efficiency in the beam suffered, dropping to an average of 83 and 59 % at beam center for x and y, respectively.

High-momentum tracks at large angles can be shorter than average. In order to maintain MCS-limited resolution for these high-Q^2 tracks, the x position measurement was augmented by following each PC with a drift chamber (DC). The measured position resolution of these chambers was better than 250 μm. The efficiency of the drift chambers was good, better than 98% in the beam area, but they were active for 260 ns or 13 rf buckets. Extra beam tracks were often recorded. These were eliminated, and the left-right ambiguities in the cells were resolved, by referring to the PC system. For further discussion of the drift chamber system, see Ref. 28.

The average momentum resolution for deep-inelastic scattering events in the MMS was $\sigma_{p'}/p'=8.6\%$ at a beam energy of 215 GeV and 9.0% at 93 GeV. The average resolution is worse at the lower energy because the tracks are typically shorter.

F. Calorimeter

Although the kinematics of an inclusive deep-inelastic scattering event can be determined entirely from the initial and final four-momenta of the scattered muon [Eq. (1)], there are experimental advantages in measuring $\nu=E-E'$ directly by measuring the energy of the hadronic final state. We used a calorimeter that sampled the hadronic shower in plastic scintillator between the 10.28-cm iron plates. This is helpful because, at low ν, $E'=E-\nu$ with E from the beam system and ν from the calorimeter gives better resolution than the magnetic determination of E'. The energy resolution of the calorimeter is $\sigma_\nu\approx 1.4\sqrt{\nu\,(\mathrm{GeV})}$. Neglecting the beam momentum resolution, the calorimeter gives better E' resolution for $E'>140$ GeV or $\nu<75$ GeV at a beam energy of 215 GeV (see Fig. 11).

Calorimeter counters were placed to cover the beam area after each of the first 75 plates, not including plate 0. The plastic scintillator was 80 cm high by 122 cm wide by 1.9 cm thick. The scintillation light was detected and the resulting signal amplified at one end of each counter by an RCA 6655 photomultiplier tube. Overall uniformity was achieved by inserting the counters from alternate sides of the spectrometer. The anode signal of each photomultiplier was amplified $\times 25$ and sent both to a discriminator for use in the two-muon trigger and to a 1024-count analog-to-digital converter (ADC) for pulse measurement. For larger pulses, the ac signal on the last dynode (about $0.6\times$ the anode signal) was read directly by a second ADC. The amplified-anode and dynode ADC's (LRS 2249's) were known as the low and high ADC's, respectively.

A typical hadronic shower reaches a maximum in the first or second plate following the vertex and extends 5–15 plates, with the mean length depending logarithmically on the shower energy. The individual counters and the calorimeter as a whole were calibrated in terms of "equivalent particles" (EP), the most probable pulse height produced in one counter by a minimum ionizing particle. This, rather than the mean, is used because the most probable pulse height is independent of the energy of the particle at large energies.[29] Our source of minimum ionizing particles is, of course, the muon beam. A single muon gives a most probable signal in each low ADC of about 20 counts. The low ADC thus saturates at ≈ 50 EP, corresponding to the maximum of a 30-GeV shower. The high ADC saturates at ≈ 2000 EP. The analysis of the calorimeter signal is described in Sec. III D. Calibration is discussed in Sec. IV B.

TABLE I. Data sets. Columns (d)–(g) refer to events with reconstructable beam tracks.

(a) Beam	(b) $\langle E \rangle$ (GeV)	(c) Intensity (μ/spill)	(d) Incident μ	(e) Triggers	(f) Track found	(g) Event fit
215 GeV μ^+	209.0	3.0×10^6	1.91×10^{11}	560 872	555 346	531 781
215 GeV μ^-	209.0	1.0×10^6	2.61×10^{10}	58 365	58 110	56 615
215 GeV tot	209.0		2.17×10^{11}	619 237	613 456	588 396
93 GeV μ^+	88.0	2.5×10^6	8.75×10^9	66 533	65 740	61 794

G. Operation of the MMS

The operation of the MMS was synchronized with the beam cycle through timing signals sent by the accelerator control system. Immediately prior to the 1-s beam spill, the on-line computer sent out test pulses and then generated a trigger to record the resulting MMS signals as in a normal event. During a test event, chamber planes were pulsed and, on alternate spills, either a pedestal level or the response to a light-emitting-diode (LED) flash was measured for each calorimeter counter.

During the spill, control of the experiment was handed back and forth between trigger and computer. The more complicated multimuon triggers, notably the dimuon trigger which required input from the calorimeter, necessitated a two-level structure of pretrigger and full trigger. For the deep-inelastic trigger, pre- and full trigger were identical. An event which satisfied the deep-inelastic trigger generated a pretrigger signal which initiated the latching of chamber information and the digitization of calorimeter pulses and started the drift-chamber clock. The pretrigger signal also inhibited further pretriggers for 3 μs. If during that time no confirming full trigger signal arrived, digitization was aborted and the latches cleared. For deep-inelastic events, a full trigger always arrived. This signal blocked further triggers for 300 μs and informed the computer that there was an event to record. At this point, the computer took over, ignoring triggers until it was through reading out the chamber systems, the ADC's and the trigger latches ($\approx$1 ms). At full intensity, typically 50 events were recorded per spill of which four were deep-inelastic triggers. Total deadtime was under 10%. Events were stored in computer memory during the spill, then written to tape during the approximate 10 s between spills.

As a measurement of the beam flux, we use the number of recorded BV triggers (Sec. II B), a quantity that identically matched the lifetime of the physics triggers. When multiplied by the known prescale value, this number, which was typically about the same as the number of deep-inelastic triggers, provided the normalization for the experiment.

III. EVENT RECONSTRUCTION

A. Data sets

During three and a half months of muon running, 1239 magnetic tapes were written. A typical tape contained one run of approximately 13 000 events, about 1200 of which were deep-inelastic triggers. General analysis of the data began at the end of the run and concluded with production running of the final versions of the track-finding and momentum-fitting programs on all analyzable data. Results of the multimuon analysis were published first.[30–33] A brief report on the deep-inelastic analysis was published as Ref. 34.

The deep-inelastic-scattering analysis used a somewhat restricted data sample, corresponding to about 70% of the analyzable data. Of concern was our ability to simulate and make corrections for data with marginal analyzability or resolution. Runs were rejected due to various forms of hardware failure, primarily in two classes. The first included data taken without drift chambers. The drift chambers contributed to the resolution of the MMS not only through their superior spatial resolution, but also by filling gaps in tracks due to PC inefficiency. The second class of rejected data included runs where the E98 beam chambers (Fig. 6) were operating poorly. The use of measured beam tracks as the parent beam distribution for our simulation required confidence that the measured parameters of reconstructed beam tracks were negligibly different from the true values. For this reason, in the runs retained for analysis, we eliminated events where the beam track was missing more than one of the possible four x hits in the E98 chambers (a 10% loss) or for which no beam track could be reconstructed at all (8%). Events of the latter type were mostly background, with an off-axis muon entering the MMS.

The data sets comprising events with good beam tracks as defined in the previous paragraph are summarized in Table I. At 215 GeV, for both μ^+ and μ^-, roughly equal amounts of data were taken with each MMS magnet polarity. At 93 GeV, bending the muons to the west in the MMS was prohibited by radiation-safety considerations and all data were taken with the east-bending magnet polarity. Column (b) shows the average energy of beam muons at the interaction vertex. It differs from the nominal beam energy by the average energy loss (1.35 GeV/module at 215 GeV) suffered by beam muons in the MMS before scattering. Column (c) is the total number of muons penetrating the MMS in the beam area during a spill. Columns (d) and (e) are the totals of incident and scattered muons used in this analysis. Columns (f) and (g) show the fates of these events up to the beginning of physics analysis and will be discussed below.

B. Track finding

Track finding was the most difficult part of the analysis of the experiment. It was complicated by several

factors, some inherent to the distributed-target design of the MMS and some due to imperfections in the instrumentation. In the MMS muons travel in nearly solid iron. We must therefore allow for substantial multiple Coulomb scattering and energy loss between position measurements. The energy-loss distribution has a tail which extends all the way up to the muon energy. In more than 20% of our single-muon events either the beam or scattered track suffered an energy loss of over 5 GeV in a single plate. This energy appeared as an electromagnetic shower, fouling the calorimeter and chambers. Delta rays which escape into a chamber without showering can degrade track finding by giving signals on wires adjacent to the one hit by the muon. These complications are compounded by instrumental effects, primarily the lifetime and inefficiency of the proportional chambers. The 70-ns PC write window extended beyond the ± 1 rf-bucket beam veto. This permitted the recording of out-of-time "ghost tracks," $\approx 20\%$ of which showered.

The PC inefficiency was a more serious problem. To allow for missing hits, it was necessary to allow projection through more than one module in extending a candidate track. The momentum uncertainty (initially very large) and multiple Coulomb scattering then demanded large search windows, increasing the probability of picking an incorrect hit to add to the track. Inclusion of a nearby wrong hit was often sufficient to derail the extension of the track. Figure 27(a) shows a typical deep-inelastic scattering event. Although its overall pattern is unambiguous, there is clearly a fair amount of electromagnetic hash obscuring the tracks.

The track-finding algorithm was basically a brute force trying of combinations of hits. In limiting the number of tested combinations, a large number of decisions regarding, for example, the multiple usage of chamber hits, had to be made. These are described in Ref. 35. For completeness, we will describe here the general operation of the track finder and discuss its limitations.

The search for hits to attach to beam and scattered tracks was limited along the beam direction by a preliminary vertex z position found using individual calorimeter pulse heights to locate the beginning of the hadronic shower. The determination of this vertex was begun by finding the largest single pulse height. In large hadronic showers, the mean location of the shower maximum occurs after more than 10 cm of iron. More important, hadronic showers have notorious fluctuations. It was therefore necessary to look upstream of the maximum to find the beginning of the shower. With A the maximum pulse height, a threshold of $0.08A$ was chosen empirically to define shower activity. To avoid missing the beginning of a shower with a large downward fluctuation in pulse height before the maximum and also to avoid incorporating electromagnetic splashes from the beam track into the shower, all pulse heights upstream of the maximum were compared to the threshold. The vertex was placed in the middle of the plate that maximized $N=$(the number of pulse heights $<0.08A$)$-$(the number of pulse heights $>0.08A$) upstream of the vertex. The operation of this algorithm is illustrated in Fig. 12.

The most frequent failure of the calorimeter vertex

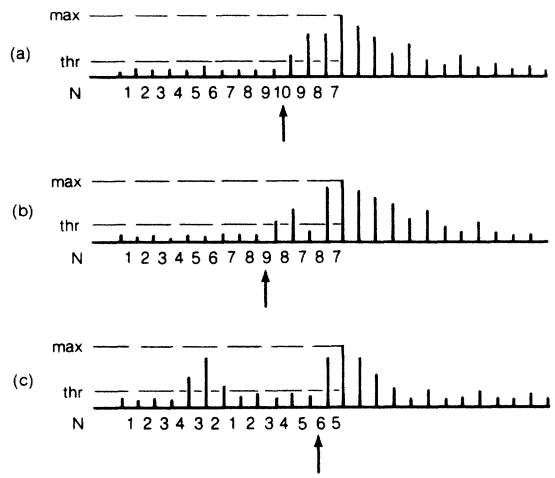

FIG. 12. The calorimeter vertex-finding algorithm. The vertical bars indicate the pulse heights in individual counters. Each pulse height is compared to a threshold of 0.08 times the maximum pulse height. The result for each counter of the algorithm discussed in the text is shown as N. The vertex is assigned to the plate following the maximum of N (arrow). The point of the algorithm is to allow for fluctuations before the shower maximum (b), without including separate electromagnetic showers (c).

finder occurred when the largest single pulse height was due to an electromagnetic shower away from the true vertex. Electromagnetic showers give more pulse height per GeV than hadronic showers. They are also shorter, and thus can have very large maxima. When the vertex finder was fooled by an electromagnetic shower, either the beam or scattered track finding was stopped short. Even if the vertex was moved to the proper location during fitting (see Sec. III C), the event was sometimes rejected for having a large gap in the track. Approximately 0.6% (1.3%) of the 215 (93) GeV events were lost in this way.

With the calorimeter vertex dividing the event into two sections, track finding proceeded with the separate reconstruction of the beam and scattered tracks. The beam track was begun in the beam chambers upstream of the MMS. Its momentum and trajectory in x and y (including, if possible, the scattering in the lead glass) were fitted. The track was then projected to the front of the MMS and the momentum was corrected for energy loss in the lead glass and other material in the beam. From there, the beam track was extended, one module at a time, by using the track as reconstructed up to that point to predict a central position in the next proportional chamber. The position, angle, and momentum uncertainties for the track and the predicted magnitude of multiple scattering were used to open a search window. A PC hit within the window was added to the track, and this was continued until the last chamber before the vertex. Only one beam track was sought.

From the back of the spectrometer, starting combinations of three hits were investigated. One empty chamber was allowed between hits, but the combination had to meet angle and linearity requirements in y and angle and minimum momentum requirements in x. Valid starting

combinations were pursued upstream module by module in the same fashion as for the beam track until the vertex was reached. The track was then projected to pick up hits downstream of the starting segment. Accepted tracks had x and y hits in at least four chambers, separated by no more than two consecutive empty chambers. At least two of the (x,y) pairs were required to be tied together by matching u hits. All possible starting combinations made up from hits downstream of the calorimeter vertex were investigated. All valid tracks of either charge were retained.

For all valid tracks, including the beam track, drift chamber hits were added after track finding was complete. In each drift chamber, the two hits closest to the track position were saved. These two hits could be the left-right options of the same hit. The choice of which to use was postponed until a better fit of the trajectory could be performed.

C. Momentum fitting

Our momentum-fitting algorithm took the measured positions of a found track and calculated the three-momentum of the track at some reference point (usually the vertex) and a detailed trajectory of the track through the spectrometer. The calculated trajectory included the effects of magnetic deflection, energy loss, and multiple Coulomb scattering (MCS). The magnetic deflection was treated as a single transverse impulse between position measurements. It used the detailed field map produced during the MMS calibration, which included the small-x component of the field. Energy loss was included as a continuous correction to the muon energy along the track. For a muon of energy E (GeV), the energy loss in MeV/(g cm^{-2}) is

$$\frac{dE}{dx}=1.825+0.0716\ln\left[\frac{E^2}{E+10.9}\right]+0.0045E\ . \tag{13}$$

Besides the ionization loss, this expression includes terms due to δ rays, bremsstrahlung, and pair production. The terms for these processes, which do not occur smoothly, represent averages integrated up to some maximum allowed energy loss. It is presumed that energy losses larger than this maximum would disrupt the track and confound the track finder, and thus would not appear within a single found track.

MCS is handled by actually fitting the residual deflections between chambers after removing those due to the magnetic field. With N measured positions, there are thus $N+2$ unknowns (the initial position, slope, and curvature, and $N-1$ MCS deflections θ_i). This distasteful situation is rectified by the constraint that the average MCS $p_\perp$ is zero. This constraint is applied by adding $N-1$ "measurements" $\theta_i=0$ with a "measurement uncertainty" equal to the expected rms value of the MCS $p_\perp$, $\delta=15\sqrt{X}$ MeV/c, with X the path length in radiation lengths. This algorithm is described in Ref. 36.

In the first fit of each track, only proportional chamber hits were used. Using the initial fitted trajectory as a guide, the x view of each track was refitted, this time with the routine choosing the best hit in each chamber from the one PC and two DC hits provided by the track finder. Outgoing tracks were then compared to check if they were segments of the same track. If so, they were rejoined. We then required that the trigger counters, which had output pulse lengths less than the width of an rf bucket, register the passage of all fitted tracks. This eliminated out-of-time muons.

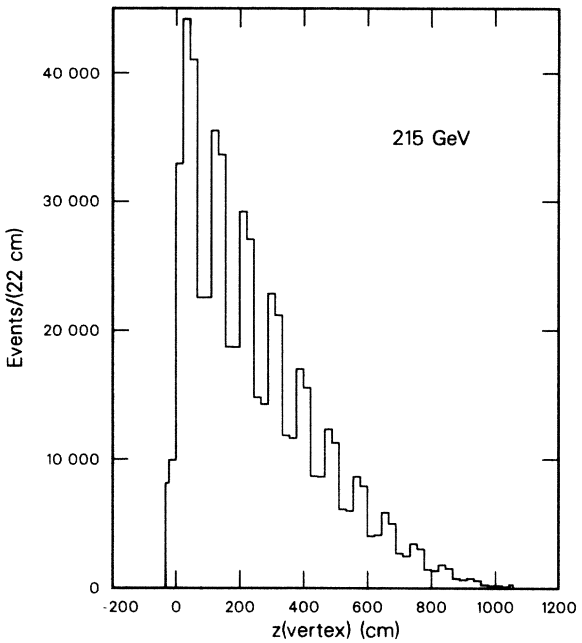

FIG. 13. The distribution of event vertices along the beam direction for the 215-GeV data.

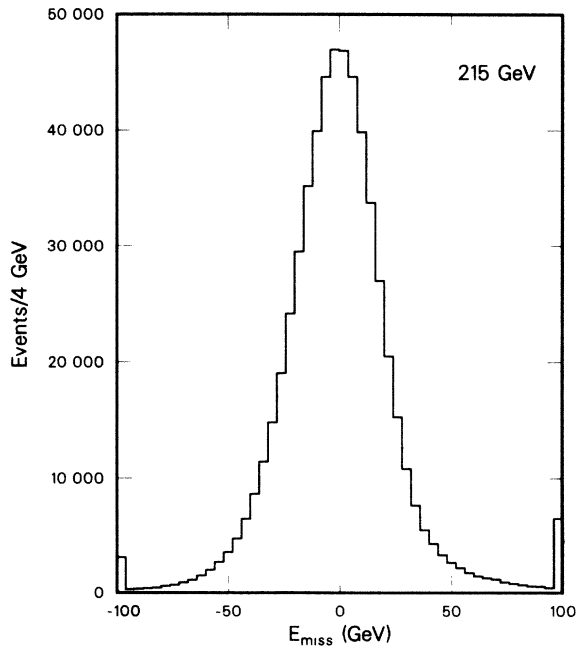

FIG. 14. The missing-energy distribution of the 215-GeV data. The mean is calibrated to be zero, and the width ($\sigma=21$ GeV) is consistent with our expected beam, momentum, and calorimeter resolution.

The next step in event fitting was to require that all tracks intersect at a common vertex. For each outgoing track, the point of closest approach to the beam track was calculated. Tracks with too large an impact parameter were eliminated. The vertex was constructed from the remaining tracks and the calorimeter vertex by finding the z position which minimized the weighted rms distance of the outgoing tracks from the beam track and the distance of z from the calorimeter vertex. If this distance was too large, the calorimeter vertex was ignored and, if necessary, tracks were eliminated. The x and y positions of the vertex were then the weighted averages of the positions of the surviving tracks at z_{vertex}. All tracks were then refit with the new requirement that they pass through the vertex. The distribution of vertex z positions from our 215-GeV data set is shown in Fig. 13. Note that the gaps between modules are easily resolved.

D. Calorimetry

Once the vertex was located, the pedestal-subtracted signals (calibrated in equivalent particles, see Sec. IV B) from calorimeter counters in the surrounding region were summed to give a direct measurement of ν, the energy of the hadronic final state. The summed region started five counters upstream of the estimated vertex position and extended to ten counters downstream of the vertex. This interval was extended if the counters at the ends showed more pulse height than expected from a single muon. In the sum, each counter signal had subtracted from it the mean pulse height from a single muon ($\approx$2.6 EP). This summed pulse height was turned into GeV via the calibration procedure described in Sec. IV B. The conversion was approximately 6 EP/GeV.

With ν determined independently, we could measure the missing energy of events, $E_{\text{miss}}=E=E'-\nu$ (Fig. 14). For deep-inelastic scattering events, this was due entirely to instrumental resolution. As discussed in Sec. II F, the otherwise redundant calorimeter information can be used to improve the E' resolution of individual tracks. The procedure assumed that the resolution of the beam energy measurement was negligible. E', previously determined from the momentum fit, was redefined to be the weighted average of the original value and $E-\nu$. The individual components of p' were then adjusted using the correlations determined in the momentum fit. Events with large $|E_{\text{miss}}|$ were suspect. Large positive E_{miss} could mean that the shower was missed completely. Large negative E_{miss} could accompany a wide-angle bremsstrahlung event with an electromagnetic shower (see Appendix A). For this reason, the calorimeter information was used only in events with $|E_{\text{miss}}|<52$ (26) GeV for the 215- (93-) GeV data sets. These cuts correspond to approximately 2.5–3σ in E_{miss}, independent of E'.

E. Performance

In Table I, columns (e), (f), and (g) summarize our success in reconstructing events. All entries refer to events with successfully reconstructed beam tracks. For the 215- (93-) GeV data sets, the scattered track was found in 99.1% (98.8%) of the events. Of these events, 95.9% (94.0%) were successfully momentum and vertex fitted. Losses through this stage of the analysis were thus 5.0% (7.1%), of which inspection showed 1.9% (1.3%) to be background.

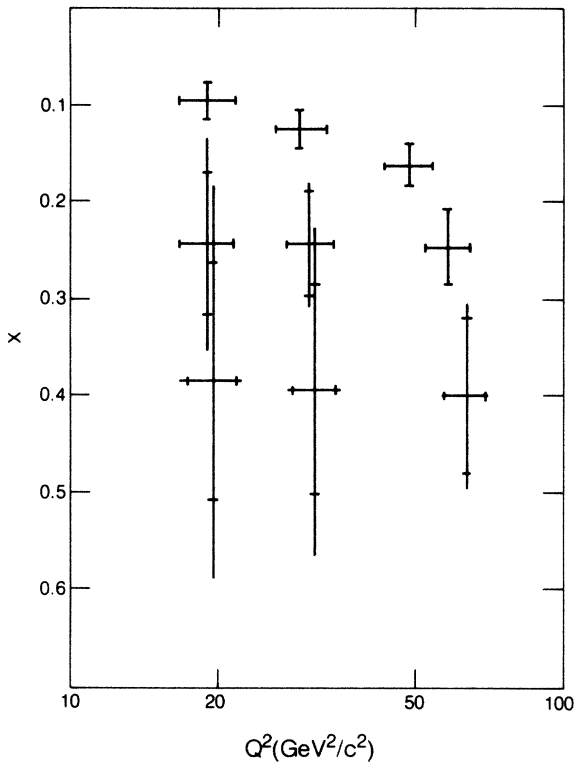

FIG. 15. MMS resolution in x and Q^2. The inner and outer bars indicate the resolution ($\pm\sigma$) with and without the use of the calorimeter. Note that the origin in x is at the top.

Momentum resolution in the MMS was limited by multiple Coulomb scattering to about 8%. The resolution for short, low-momentum tracks was somewhat worse—about 10%. Using the calorimeter improved the resolution at high E' dramatically. In the 215-GeV data, the resolution for $E'>150$ GeV without the calorimeter was $\sigma_{E'}=0.08E'$. Using the calorimeter improved the resolution to $\sigma_{E'}=0.05E'$. Figure 15 shows our resolution in Q^2 and x at various locations in the Q^2-x plane. The inner and outer bars indicate σ with and without calorimetry. The largest improvement occurs at low ν, that is, the lowest Q^2 for each value of x. This figure includes the effects of radiative corrections which, in effect, change the internal kinematics of an event without changing its appearance to the outside world. The Q^2 resolution was roughly constant at 13%. The x resolution varied between 13 and 30%.

These values for the resolution come from a program which simulates deep-inelastic scattering events in the MMS. At 215 GeV, the width (σ) of the distribution of $(E'_{\text{measured}}-E'_{\text{generated}})/E'_{\text{generated}}$ is between 0.074 and 0.083, depending on how much of the tail is included. Another estimate of the resolution comes from the momentum uncertainty calculated by the fitting routine, combined with the calorimeter resolution. For the same simulated events, the mean uncertainty is 0.077. This is a useful quantity because it can also be calculated for real

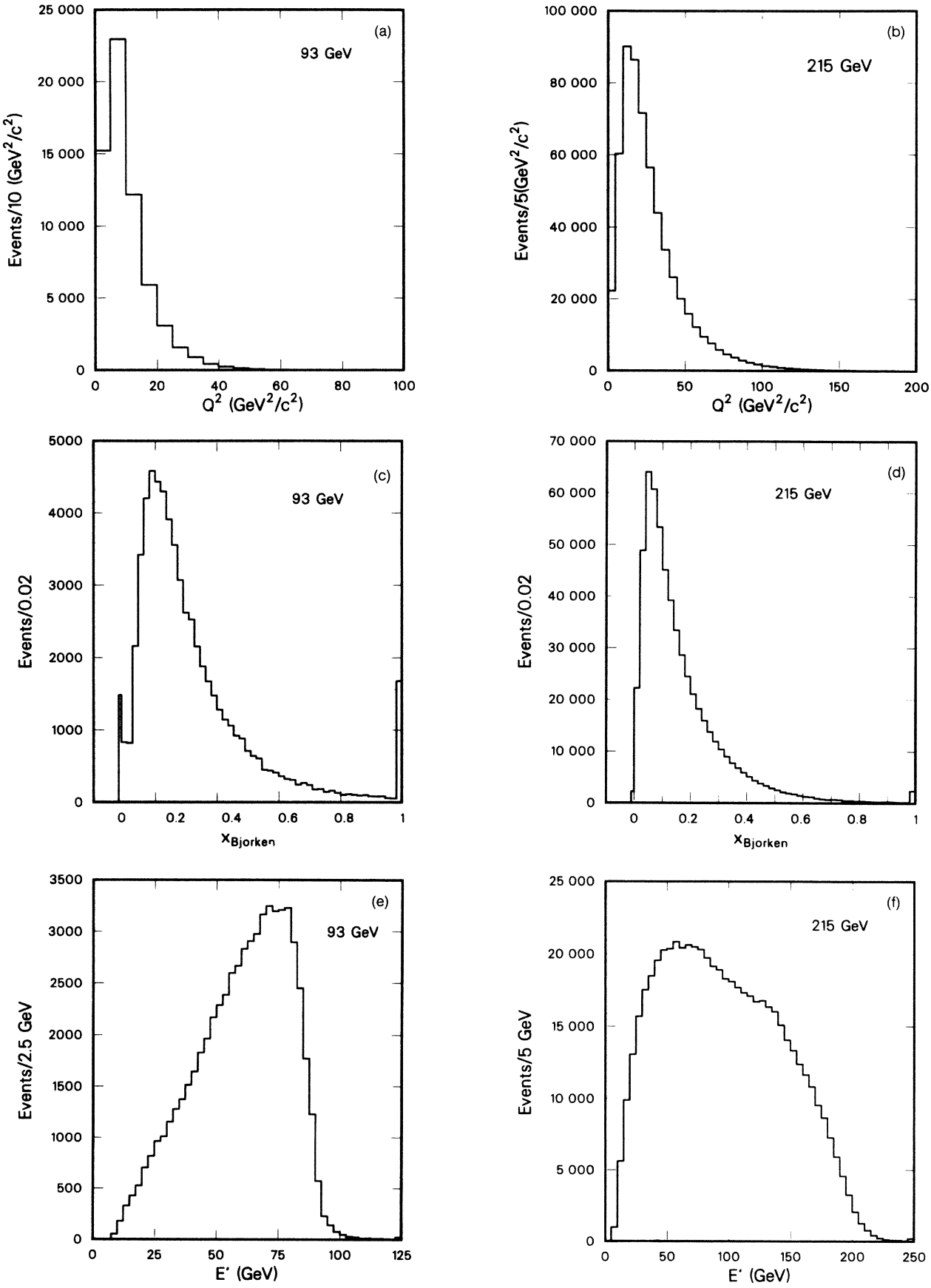

FIG. 16. Spectra of all reconstructed events in Q^2, x, and E'.

events, where the result is 0.076.

The results of the data reduction are shown in Fig. 16, where the measured spectra of reconstructed events in Q^2, x, and E' are plotted for both the 215- and 93-GeV data samples. The production running of the event reconstruction routines on our large amount of data was an arduous task that was performed only once on the full set of analyzable data. The effects of minor mistakes found after that point were corrected by subjecting the simulated events used in the acceptance calculation to the same errors in reconstruction.

IV. CALIBRATION

A. Spectrometer calibration

Surveying instruments were used to align both proportional and drift chambers in the MMS to an estimated 130-μm accuracy. The alignment was checked and improved during data reduction by using muon trajectories from BV triggers to determine alignment constants, offsets to be added to raw coordinates in each chamber. The drift chambers were aligned to about 80-μm accuracy for the event reconstruction. After the production running of the analysis, the drift chamber offsets were remeasured to 20 μm and these locations were put into the apparatus simulation, the events from which reconstructed with the same set of constants used on the real data.

With the position, angle, and curvature (momentum) of the tracks left free in the fit, constant systematic offsets in alignment or those that go as z or z^2 are not detectable in the residuals. The assumption used in the alignment procedure was that there were no such effects and the mean offset, angle, and curvature of the alignment constants was zero. Yet it is precisely the last of these terms that can systematically affect the momentum measurement. In fact, after the initial alignment, it was found that the average fitted momenta for east- and west-bending 215-GeV tracks differed by 1.06 GeV, indicating that a finite curvature did exist in the alignment, corresponding to a radius of curvature of 214 miles. A quadratic correction was thus applied to the drift chamber offsets. This correction was everywhere less than 60 μm.

The possibility that the chambers were rotated about their centers also had to be investigated. To be affected by chamber rotation, a track must have both a large scattering angle and a high momentum. Fortunately, the kinematic limit $Q^2 \leq 2M_N\nu$ (or Bjorken $x \leq 1$) gives a maximum scattering angle that varies inversely with p'. Given our survey precision, this restricts the possible systematic effect on the momentum at 215 GeV to less than 0.1%.

The absolute calibration of the MMS magnet was described in Sec. II C. In the beam system, both the last dipole and the Chicago cyclotron magnet (CCM) were used for the momentum measurement of beam muons and had to be calibrated. The field integrals of the last dipole and CCM magnets were numerically integrated from flip coil measurements of the field along the path of the beam. At 215 GeV, the dipole magnet was operated at 4515 A, giving a field integral of 205.9 kG m. The CCM field integral at 3100 A was 59.70 kG m. At 93 GeV, the field integrals were 88.4 kG m and 29.60 kG m.

The beam chambers were aligned in a similar fashion to those in the spectrometer. Here we were aided by the fact that some of the chambers were on a direct unobstructed line and could be aligned with magnets off and no bending. With both the beam and spectrometer aligned and calibrated, BV triggers could be used to compare the two systems. Using equal amounts of 215-GeV east- and west-bending MMS data, a discrepancy of $p_{\text{beam}} - p_{\text{MMS}} = 2.39$ GeV/c was found, a value that was constant throughout the experiment. This 1.1% difference was attributed to calibration or alignment errors in the beam system. There were two pieces of evidence backing this interpretation. The first was the estimated error in the MMS magnet calibration of 0.2%. This was confirmed at a level smaller than 1% by our measurement of the ψ mass using muon pairs in the MMS (Ref. 19). For the elastic, inelastic, and total ψ samples, the differences between the measured and true mass were 0.7, −0.9, and 0.2%, with statistical errors of about 0.2%. We thus applied −2.39 and −1.67 GeV/c corrections to the measured momenta of individual beam tracks in the beam system for the 215 and 93 GeV/c beams.

B. Calorimeter calibration

Using the definition of equivalent particles (EP), the single-muon pulse-height spectrum for each calorimeter counter was inspected by eye to determine the location of the peak, after pedestal subtraction. As a preliminary study revealed no time variation of this calibration, only one set of constants was used. Single muons gave no appreciable signal in the high ADC's. The high scale was calibrated by comparing large low ADC signals from showers with their high ADC counterparts.

The energy calibration was performed in two steps, each of which compared the summed calorimeter signal to ν_{mag}, the value of the shower energy measured magnetically as $E - E'$. The first calibration simply fit $S = c\nu_{\text{mag}}$ where S is the sum of calorimeter signals in EP described in Sec. III D. The value found for c was 5.965 EP/GeV. This linear fit was adequate only as a starting point. Problems with it included a possible offset due to inadequacies in the muon pulse-height subtraction and an observed nonlinearity (faster than 5.965 EP/GeV at large ν). The muon subtraction used the mean pulse height for 215-GeV muons. Unlike the most probable pulse height, the mean is energy dependent, and a correct subtraction should depend on ν. The antisaturation is believed to be due to radiative corrections, especially wide-angle bremsstrahlung events, which add a large-pulse-height electromagnetic component to the showers and which trigger the MMS only at large ν. The final energy calibration was also the catch-all for curing the deficiencies in the previous calibration stages.

The final calibration was a correction derived from another comparison of ν_{calor} with ν_{mag}, which necessarily has its worst resolution where we need the calorimeter the most. At low ν [or high E', see Fig. 16(f)] the spectrum of triggered events drops off rapidly. Thus a bin of low

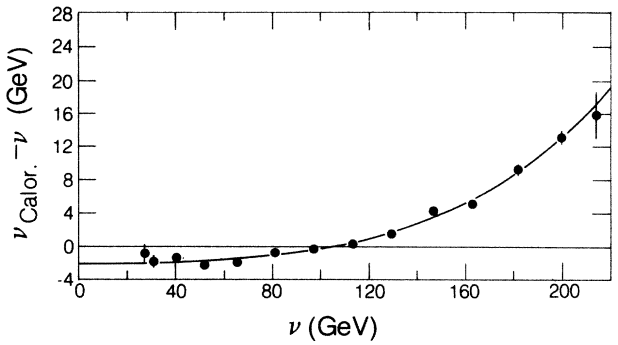

FIG. 17. Typical calorimeter final calibration plot. Uncorrected ν (calorimeter)—ν (true) is plotted vs ν (true) determined bin by bin using our Monte Carlo simulation. The curve is the fit to be subtracted from the uncorrected measurements to give the final calorimeter energy.

measured ν_{mag} has $\langle \nu_{true} \rangle > \langle \nu_{mag} \rangle$ due to smearing. This bias must be removed from the calorimeter calibration. This was done using the apparatus simulation (see Sec. V) which produced events with known values of both ν_{true} and ν_{mag}.

The final calorimeter calibration began with samples of real and simulated data, each divided into bins of measured ν_{mag}. For each bin, we produced histograms of ν_{calor} for the real data and ν_{gen}, the true value of $E - E'$, for the simulated data. We then plotted $\langle \nu_{calor} \rangle - \langle \nu_{gen} \rangle$ vs $\langle \nu_{gen} \rangle$. One such plot is shown in Fig. 17. These points were then fit, using a fourth- or sixth-order polynomial with only even powers of $\langle \nu_{gen} \rangle$. The fit was then used to correct the original linear calibration. Inspection of the calibration plots for different blocks of data showed significant time dependence. Much of this was found to be synchronized with the field reversals of the MMS, an effect tracked to magnetic field sensitivity in individual photomultiplier tubes. These effects were corrected in an average sense only by separately calibrating blocks of data, each spanning only one MMS polarity. We also looked for the effects of transverse shower containment on the calibration. Fortunately, large shower recoil angles are correlated with small shower energies and thus shorter showers. A look at the least favorable combinations of ν, θ_{shower}, and the vertical position of the vertex showed no visible effect. An empirically motivated search for Q^2 dependence showed an effect at large ν, beyond where the calorimeter contributes to the ν resolution. This effect, visible also in the simulated data sample, is due to radiative events which occur preferentially at large ν and low Q^2.

By methods similar to those used in the calibration, we determined the resolution of the calorimeter. Using the same binned data, we used the widths of the histograms to compute

$$(\sigma_{calor})^2 = (\sigma_{\nu_{calor}})^2 - (\sigma_{\nu_{gen}})^2 . \quad (14)$$

The results are plotted as $\sigma_{calor}/\sqrt{\nu_{gen}}$ vs $\langle \nu_{gen} \rangle$ in Fig. 18. This procedure was very susceptible to disruption by tails in the histograms. For this reason, in Fig. 18 we show also for comparison σ_{calor} extracted by this method

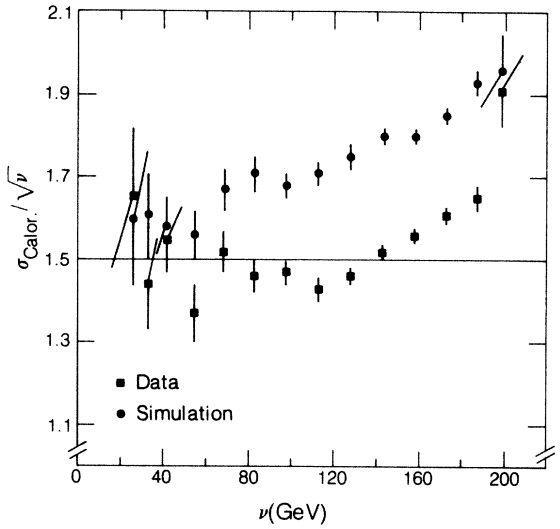

FIG. 18. Calorimeter resolution. The circles show the results of the calculation when applied to simulated events generated with $\sigma_{calor} = 1.5\sqrt{\nu}$. The method thus somewhat overestimates the resolution. The simulated resolution was later adjusted to match that of the data.

from simulated data generated with $\sigma_{calor} = 1.5\sqrt{\nu\ (\text{GeV})}$. From measurements such as this we estimate that $\sigma_{calor}/\sqrt{\nu} = 1.35$–$1.7$ at $\nu \leq 80$ GeV for various blocks of data, with a typical value of 1.4, substantially worse than the current state-of-the-art of 0.9, a value which we approached in early small-scale tests in a pion beam. The reasons for this degradation are thought to lie primarily in the early calibration stages (counter to counter and ADC high to low), but include also an inherent component from fluctuations in the background energy loss of the muon (or muons).

The use of the calorimeter information to improve the energy resolution of the MMS was described in Sec. III D. The relative values of the calorimetric and magnetic resolutions in ν naturally restrict the effect of the calorimeter to low values of ν (see Fig. 11). At large ν, several problems appeared in the calorimetry including the radiative effects mentioned above, other poor calibration behavior, and lack of agreement between real and simulated calorimeter resolution. For these reasons, we quenched the calorimeter's contribution to ν by unweighting the contribution of the calorimeter by a further factor of $(\nu/\nu_c)^2$ for $\nu \geq \nu_c$. For the 215- (93-) GeV data, ν_c was 80 (40) GeV.

C. Trigger-counter efficiency

The discovery of a large, position-dependent inefficiency in some of the paddle counters that make up the deep-inelastic trigger was a crucial one. The systematic pattern of inefficiency, largest near the beam and decreasing (improving) toward the top and bottom was almost exactly that needed to create spurious Q^2 dependence—a disaster for an experiment attempting to measure precisely logarithmic scaling violations. Fortunately, the existence of parallel subtriggers in the deep-inelastic trigger allowed this discovery and also the measurement and mapping of

the inefficiency with triggered (i.e., recorded) events.

The method used to measure the efficiency took advantage of the fact that, for a muon penetrating more than three paddles, those paddles outside of any satisfied subtrigger are redundant and can be checked in an efficiency measurement. Thus the events satisfying any subtrigger provide an unbiased sample for the study of the five other trigger banks. Using such events, most of the active region of the paddles could be mapped. The exceptions were those regions which could not be penetrated by a muon that also lit three other counters. There were two such regions: the outer edges (away from the beam) of paddles in the first three trigger banks, and, more importantly, the inside edges of the last three trigger banks. Of these, the most crucial was the inside edge of bank 6, through which every low-Q^2 event in the experiment passed. These regions were filled in by using multimuon events after a -0.5% correction determined by comparing the regions where multi- and single-muon events each give a good measurement.

Using the entire sample of analyzed events, efficiency maps of each paddle counter were prepared on a grid with 6 cm spacing in x and five cells in y ranging from 3 cm high near the beam to 18 cm high at the top and bottom of the spectrometer. Since time dependence was observed in the efficiency of several counters, the data set was divided into three blocks and three separate maps were produced. Where no time dependence was noticeable, the total sample was used for each map. The efficiency in each cell was typically measured to better than 5%. Figure 19 is a contour map of a trigger bank, showing typical good and bad counters. The completed maps were included in the apparatus simulation for the calculation of the acceptance of the MMS.

Knowing the trajectory of a scattered muon, one can calculate the trigger efficiency for that track using the information from the maps. For muons penetrating more than the required three paddles, the efficiency, of course, goes up. The statistical uncertainties attached to the penetrated map cells can be similarly combined to give an uncertainty in the trigger efficiency for a single event. The distributions of trigger efficiency and uncertainty for the events used in the deep-inelastic analysis are shown in Fig. 20. The mean efficiency and uncertainty are 0.83 and 0.057, respectively, with the efficiencies of 94.5% of the events known to be better than 10%. Although expecting averaging to smooth statistical errors in the paddle maps is risky, one can count on at least a fourfold averaging from the four quadrants of the MMS which, after adding the two magnet polarities, are identical except for paddle inefficiency. (For the 93-GeV sample, the symmetry is only twofold because only one MMS polarity was permitted.) Looking at events from individual x-Q^2 bins used in the F_2 analysis shows that at least five map bins in each quadrant of each trigger bank are illuminated in the worst (lowest Q^2) case. Thus, even in the worst case, the efficiency measurements for events in a single x-Q^2 bin are uncorrelated enough to reduce the effects of statistical errors by a factor of 4 or 5. Allowing for different combinations of map cells in different trigger banks reduces the correlation further. The residual uncertainty in our

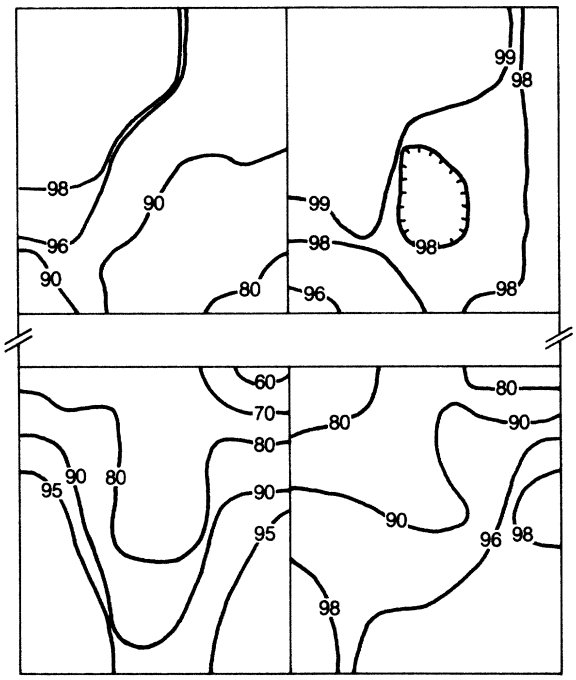

FIG. 19. Efficiency contour map of one trigger hodoscope showing counters of varying quality.

results due to trigger-counter efficiency will be discussed further in the section on systematic errors.

V. THE APPARATUS SIMULATION

A. Acceptance calculation

The acceptance A of the MMS is primarily a geometrical quantity depending on what range of angles and energies will project scattered muons into the paddle counters of the trigger banks. It also includes the efficiency of the trigger counters and can be extended to include the efficiency of the reconstruction programs. A Monte Carlo calculation is used to integrate over variables that determine the acceptance such as trigger geometry, beam phase space, multiple scattering, and chamber efficiency. To do this, simulated events are generated and propagated through a computer representation of the MMS.

With the acceptance known, the cross section can be calculated from

$$d\sigma(x,Q^2)=\frac{D(x,Q^2)}{ITA(x,Q^2)}\ , \tag{15}$$

where I and D are the numbers of incident and triggered muons and T is the number of target nucleons per unit area. There is a more convenient form of this expression that allows full advantage to be taken of the details of the simulation. Using the definition of A as it is calculated in the simulation,

$$d\sigma^{\rm meas}(x,Q^2)=\frac{nD(x,Q^2)}{M(x,Q^2)}d\sigma^{\rm gen}(x,Q^2)\ . \tag{16}$$

In this expression, $d\sigma^{\text{meas}}$ is our measured cross section, $d\sigma^{\text{gen}}$ is the cross section used to generate the simulated events, D and M are the numbers of triggered data and triggered Monte Carlo–generated events, and n is the normalization, the ratio of incident muons in the simulated and real samples. Equation (16) is the basis of our analysis. Its convenience stems from the fact that no reference is made to untriggered events, either real or simulated. Only triggered simulated events have to be saved, and they can then be recorded and reconstructed in the same format as data. This equation is also used to make important corrections for resolution smearing. This procedure is described in Sec. VI C.

It is absolutely crucial that our simulation accurately model in detail the behavior of muons in the MMS. We have no "clean" data sample. Our acceptance and resolution have long tails due to occurrences that would be unlikely anywhere but in 5.34 kg/cm^2 of iron. In kinematic regions of small cross section, these tails can dominate the observed population of events. It is essential that we have confidence in our ability to model not just typical behavior, but these tails as well.

B. Beam and target

The rapidly rising deep-inelastic cross section as $Q^2 \to 0$ makes us quite sensitive to the details of the beam phase space. Our trigger makes us especially sensitive to the spatial and angular distributions of the beam in the vertical (y) coordinate. For this reason, and also because frequent adjustments were made in the beam line settings to improve the yield of muons, we did not try to simulate the beam. We instead used the random selection of untriggered beam tracks recorded in each run as the parent sample of incident muons for the simulation of that run. For each event, the real beam chamber hits are copied to the simulation output tape and the beam track *as reconstructed* in position, angle, and momentum at the front of the MMS is propagated to the interaction vertex by the same routine used for scattered muons (see below). This method, the use of reconstructed values as actual values, supposes that the resolution of the beam system is negligible compared to the width of the beam in all relevant variables. This is calculated to be the case normally. The elimination of data suspect under this criterion was discussed in Sec. III A.

In the simulation the vertex z position is chosen randomly in the material of the first 13 modules, including plate zero. The scatter may take place in any of the elements of the spectrometer (iron, scintillator, chamber windows, etc.). Because 95% of the scatters take place in the iron plates, the target is always treated as a nucleon in an iron nucleus.

C. Event generation

When the beam muon reaches the z position of the vertex, its energy (after dE/dx losses) is handed to the event generator which will determine the kinematics of the interaction and the three-momentum of the scattered muon. The generator uses the deep-inelastic cross section in the form [see Eqs. (2) and (5)]

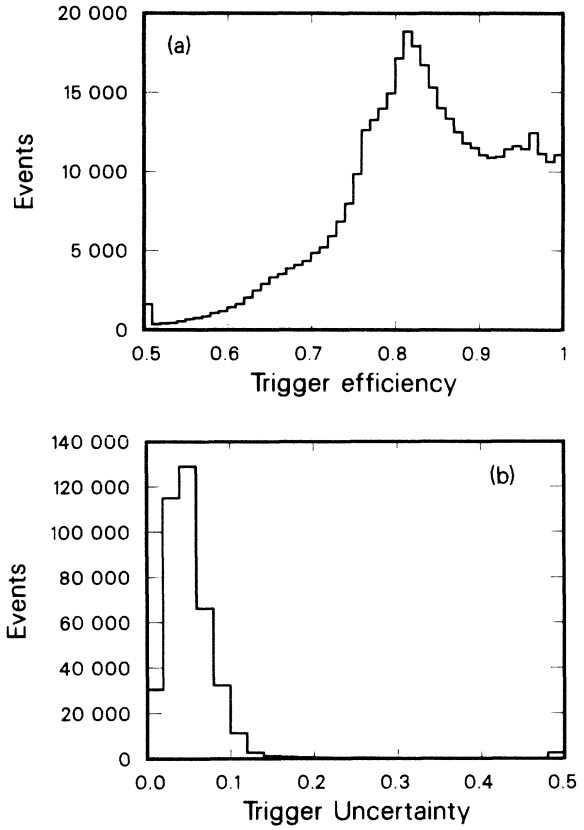

FIG. 20. Total triggering efficiency (a) and its uncertainty (b) calculated for individual events in the 215-GeV data.

$$\frac{d^2\sigma}{dv\,dy} = \frac{4\pi\alpha^2}{2M_N E}\frac{1}{v^2 y}\left[1-y+\frac{y^2}{2(1+R)}\right] \times F_2(x=v/y, Q^2=2M_N E v)\ . \tag{17}$$

It first chooses $v > v_{\min}$ and $y > v$. We use $v_{\min}=0.015$, low enough so that the acceptance is nearly zero below $v_{\min}$. This $v_{\min}$ corresponds to $Q_{\min}{}^2=5.9$ (2.5) at the average energies at the vertex of the 215- (93-) GeV data sets. The cross section at this v and y is then calculated using a nominal beam energy of 200 GeV and $R=0$. For

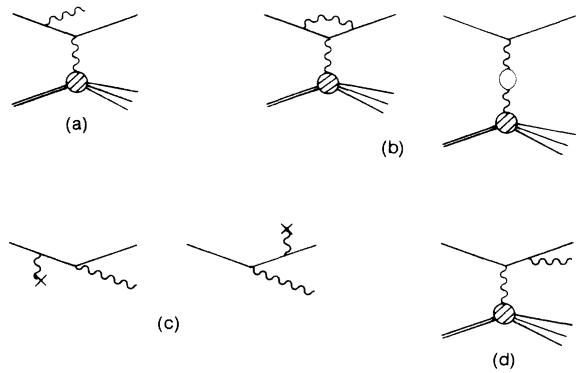

FIG. 21. Radiative corrections. (a), (d) Internal bremsstrahlung; (b) vertex and vacuum polarization; (c) wide-angle bremsstrahlung.

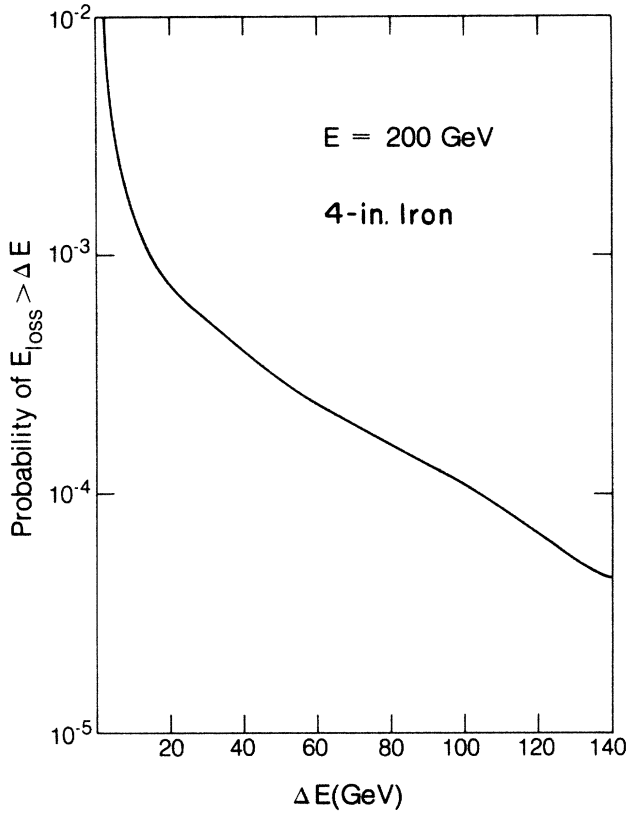

FIG. 22. Energy-loss spectrum for 200-GeV muons in 4 inches of iron.

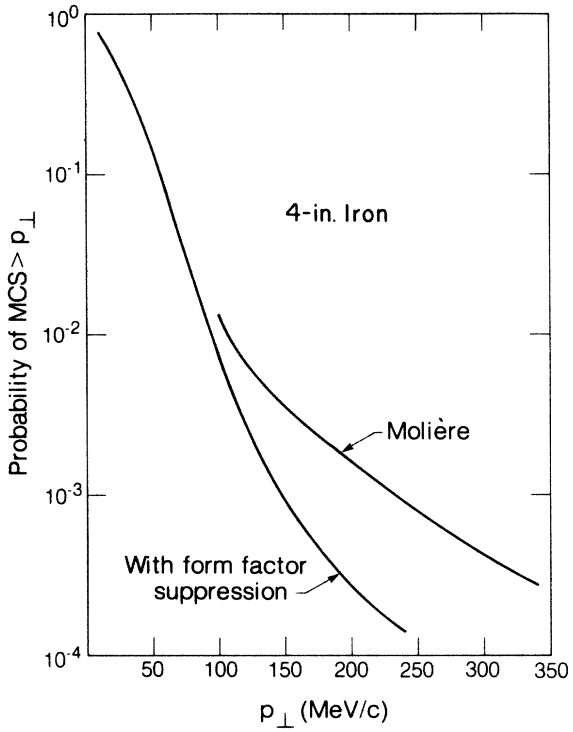

FIG. 23. Multiple Coulomb scattering $p_\perp$ spectrum for 4 inches of iron. The tail with and without form-factor suppression of single scattering is shown.

$F_2(x,Q^2)$ we use the parametrization of Buras and Gaemers.[37]

Once v and y are chosen and the nominal ($E=200$ GeV) cross section for the event is known, the distribution is shaped to take into account the actual energy of the beam muon at the vertex and radiative corrections. Radiative corrections are treated in four parts, corresponding to the diagrams of Fig. 21. The first and last diagrams contain the radiation of a real photon in conjunction with the deep-inelastic scattering. These are handled using the peaking approximation which assumes that the radiation leaves the muon direction unchanged and the method of equivalent radiators which treats the radiation as a separate energy loss due to a Q^2-dependent number of radiation lengths.[38] A new cross section is calculated for the actual beam energy, including energy loss in the target before the vertex and in the initial equivalent radiator. This cross section is then corrected for the contribution from the vertex and vacuum-polarization diagrams of Fig. 21(b) (Ref. 38). To this cross section is added the cross section for the wide-angle bremsstrahlung (WAB) process of Fig. 21(c) (Ref. 39). This can be viewed either as a background process or as a correction to the peaking approximation—a quasielastic scatter with most of the deflection of the muon occurring at the radiative vertex. WAB makes its largest contribution ($\approx 3\%$ after cuts) at large y and low Q^2. Radiative corrections are discussed further in Appendix A.

For events successfully passing the final shaping, the outgoing muon's energy and polar angle with respect to the beam track are

$$E'=E(1-y)(1-y_f)\,,$$
$$\theta=2\arcsin\left[\frac{M_N v}{2E(1-y)}\right]^{1/2}\,, \tag{18}$$

where y_f is the fractional energy loss in the final equivalent radiator. The azimuthal angle ϕ is chosen randomly. Finally, the outgoing track is rotated from the coordinate system of the beam track to that of the spectrometer and its three-momentum is handed to the propagation routine.

D. Muon propagation

The propagation routine constructs the trajectory of the beam muon from the front of the spectrometer to the vertex, and that of the scattered muon from the vertex to where it exits the spectrometer. It projects the path through one element of the MMS at a time. In active elements (chambers, trigger counters, and calorimeter counters) the position of the trajectory is recorded. In these elements and in the air gaps the muon path is a straight line. In each iron plate the muon is subjected to energy loss, magnetic deflection, and multiple scattering. Although these processes are treated as occurring only in the iron, the net amounts assigned to each plate include contributions from the gaps.

The energy lost by the muon in an iron plate is calculated as the sum of five terms: average ionization losses

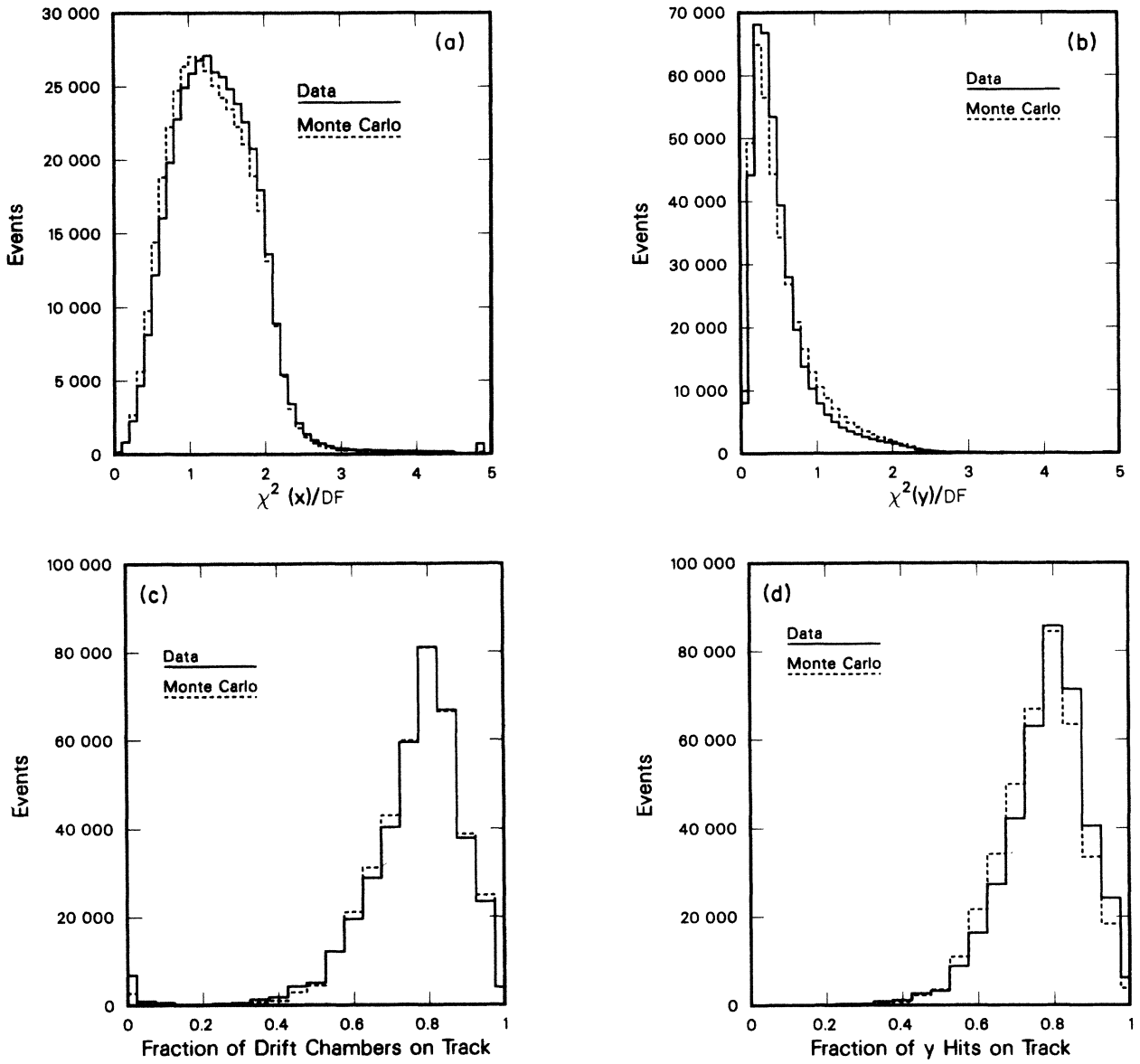

FIG. 24. Comparisons of real data and simulation in (a), (b) momentum-fit χ^2/DF and (c), (d) fraction of chamber hits on tracks.

(below $0.01E$), stochastically chosen ionization losses (to knock-on electrons above $0.01E$), average and stochastic losses to pair production (below and above $0.001E$, respectively), and stochastic losses to bremsstrahlung.[40] The probability distribution of energy losses above 5 GeV for a 200-GeV muon in one 4-inch iron plate is shown in Fig. 22. Muons are allowed to lose energy until the range in iron is less than one plate thickness. The subsequent decay is not simulated. For use in the propagation routine, the energy loss in a plate is divided in half and the halves are applied before and after the deflections due to the magnet and MCS.

The magnetic deflection in each plate is calculated from the detailed field maps produced during the MMS calibration. Both the x and y components of the deflection are included. Each is treated as a single transverse impulse halfway through the plate.

Multiple Coulomb scattering $p_\perp$'s are chosen from a distribution calculated using the method of Molière as illuminated by Bethe.[41] In 4 inches of iron the Rutherford scattering formula predicts a significant probability for scattering at quite large $p_\perp$'s, much larger than the $p_\perp$'s anticipated by Molière and Bethe. While the single scattering law used by these gentlemen includes a screening suppression at small $p_\perp$, it lacks the high $p_\perp$ roll-off due to the nuclear form factor. The Molière distribution thus has a tail extending to very large $p_\perp$ which is dominated by single scattering well beyond where the form factor should suppress it (see Fig. 23). To cure this, we subtract from the distribution the absolutely normalized Rutherford cross section for single scattering multiplied by $(1-|F(p_\perp{}^2)|^2)$. The form factor we use is a Gaussian for the nucleus plus an incoherent sum of terms for the protons. The resulting suppression of the tail is also

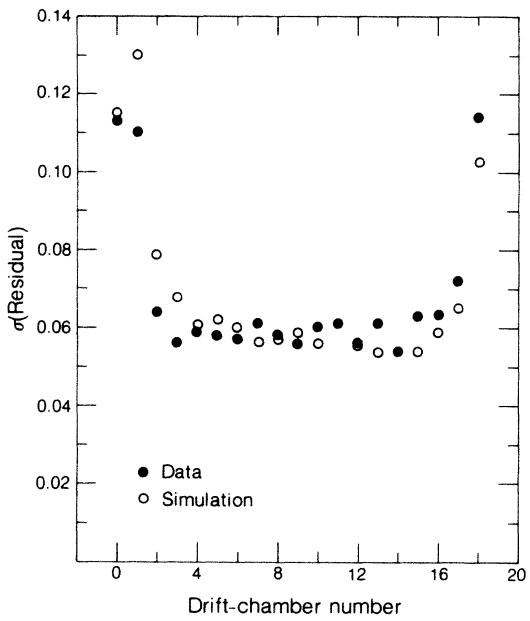

FIG. 25. Widths of the residual distributions in each drift chamber.

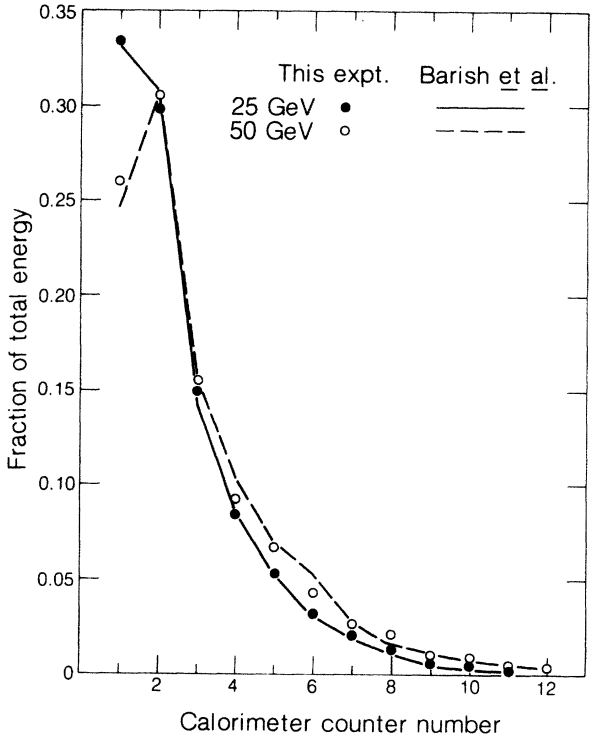

FIG. 26. Mean longitudinal distribution of hadronic-energy deposition in the calorimeter at $\nu=25$ and 50 GeV. At the higher energy, shower maximum is typically after more than 4 inches of iron. The curves show similar measurements from Ref. 29.

shown in Fig. 23. This procedure is only approximate because it does not deal correctly with the plural scattering region.

The propagation of the scattered muon continues until the muon leaves the spectrometer. The position of the muon in each trigger bank is inspected. If the counter is a paddle, the position is used to look up the efficiency in the maps constructed from the data. Only the appropriate fraction of penetrations result in latched counters. The pattern of latched counters is then tested against the deep-inelastic trigger requirement.

E. Data simulation

Events which satisfy the trigger are turned over to a routine which simulates the information produced by the MMS, including its defects and blemishes. These blemishes—chamber hits from showers, missing hits, adjacent wires hit by δ rays, etc., are important. As an example, the track-finding failure rate doubles in data taken with any one of the proportional chambers in the middle half of the spectrometer switched off. The results of this routine are shown in Fig. 24 and 25. Figures 24(a) and 24(b) show distributions of χ^2 per degree of freedom for fits of real and simulated tracks in the x and y views. Figures 24(c) and 24(d) show an overall measure of chamber and track finding efficiency, the fraction of hits present on individual tracks in the DC's and the y view of the PC's. A value of 1.0 corresponds to a hit in every chamber penetrated by a track. In Fig. 25 we show the widths (σ) of the residual distributions ($x_{\text{meas}}-x_{\text{fit}}$) in the drift chambers, where the fit has been performed ignoring the information in each chamber in turn. These distributions give us confidence that our modeling of the resolution of the MMS is adequate.

Every deep-inelastic event has a hadronic shower which produces a distribution of pulse heights in the calorimeter and also creates a splash of hits in nearby chambers. The response of the calorimeter must be modeled to give data and simulation the same resolution at low ν. The splash in the chambers must also be included in the simulation because it affects track finding and vertex resolution. The shower simulation was based on a parametrization of showers from our deep-inelastic data. An example of the data used in the parametrization is shown in Fig. 26. There was no physics input whatsoever.

Electromagnetic showers were parametrized and simulated in a similar fashion. The sample of real showers used to determine the parameters was found in BV (random) triggers using the calorimeter. The showers showed about 10% more pulse height per GeV than hadronic showers, with a resolution of $\sigma_\nu \approx 2.3\sqrt{\nu}$. An electromagnetic shower was simulated for each energy loss exceeding 5 GeV in an iron plate. For wide-angle bremsstrahlung events, an electromagnetic shower replaced the hadronic shower at the vertex.

F. Operation and performance

The use of real beam tracks as the beam sample for the simulation provided an automatic normalization, both between simulated samples and with the data, through the known sampling fraction in the BV trigger. The total Monte Carlo–simulated data sample corresponds to $1\times$ the 215-GeV data and $2\times$ the 93-GeV data. These events

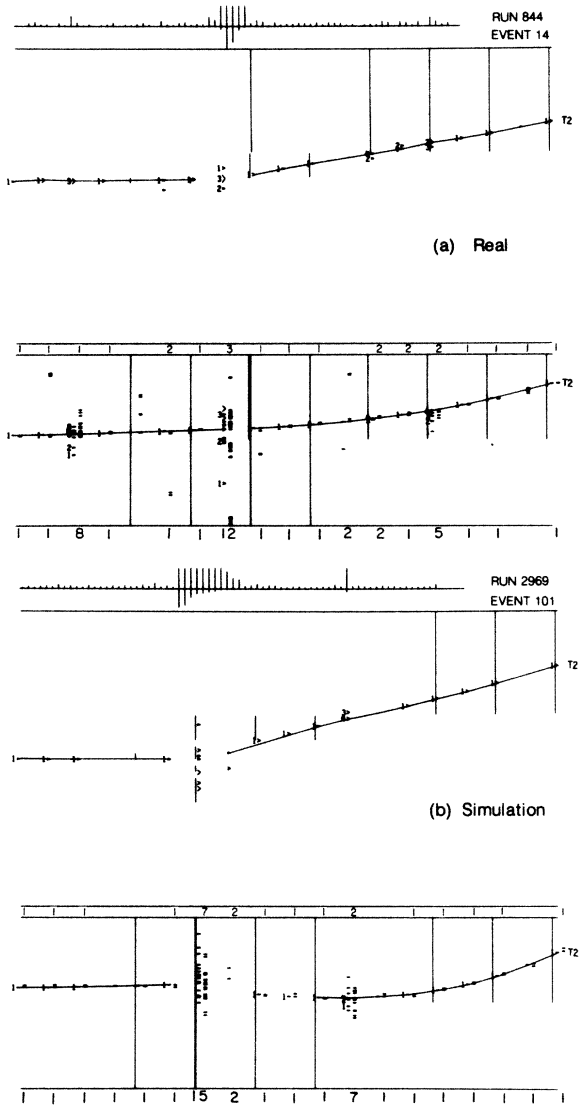

FIG. 27. Typical real (a) and simulated (b) event. Shown are computer displays of raw data from the track-finding program with line segments connecting PC hits assigned to tracks. From top to bottom are a bar graph of calorimeter pulse heights, low ADC above and high ADC below, the side view of the spectrometer, and the top view. The beam enters from the left. Vertical lines are hit trigger counters. In each chamber, the width of the caret indicates the span of consecutive hit wires. In the top view, the upstream and downstream hits in each module are those in the PC and the DC, where both of the left-right ambiguous solutions are shown. Note the electromagnetic splashes in both the chambers and the calorimeter, and the dense distribution of hits in the hadronic shower.

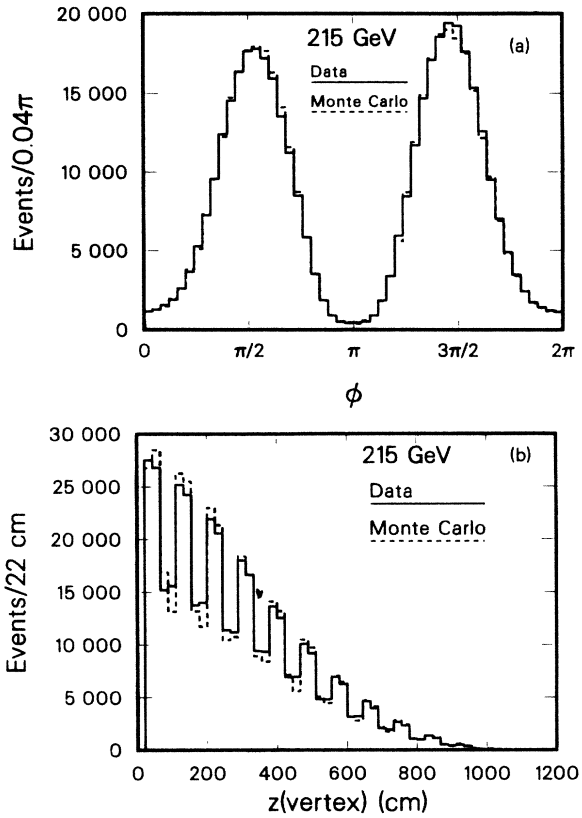

FIG. 28. Comparison of real and simulated distributions in (a) azimuthal scattering angle and (b) vertex position along the beam.

were then reconstructed using the same routines used on the real data. Generating and reconstructing the total simulated sample consumed one week of CDC 7600 central processor time.

The remaining figures in this section are evidence of the success with which we can model the complex acceptance and resolution of the MMS. Figures 27(a) and 27(b) show typical real and simulated events. The simulation reproduces all the features of a real event except for hits not related to the beam or scattered muons and the details of low-level fluctuations in the single-muon pulse heights in the calorimeter. Distributions of real and simulated events in two variables that depend only indirectly on the details of the cross section are shown in Fig. 28. In the figure, the samples are those which result from the application of the analysis cuts and shaping procedure described in Sec. VI A. The numbers of events in the two samples have been normalized. Figure 28(a) is the distribution of events in ϕ, the azimuthal angle of the scattered muon with respect to the beam track's direction at the vertex. Bending of the beam in the spectrometer before the vertex correlates this coordinate system to that of the spectrometer and the distribution has peaks at $\pi/2$ and $3\pi/2$ corresponding to the vertical scatters required by the trigger. Distributions of vertex z locations are shown in Fig. 28(b). The mean z positions are 281.0 ± 0.3 cm and 280.7 ± 0.4 cm for the real and simulated samples.

VI. ANALYSIS

A. Cuts and the final data sample

Our analysis is based on the comparison of distributions of reconstructed real and simulated events with all differences attributed to differences between the actual cross section and that used in the simulation. In doing this, we are assuming that the effects of the apparatus and reconstruction on the distributions are adequately modeled. We

TABLE II. Kinematic cuts. Those in parentheses remove a negligible number of events.

Variable	93 GeV	215 GeV
E	$75<E<96$ GeV	$196<E<217$ GeV
ν	>10 GeV	>20 GeV
E'	(>10 GeV)	>10 GeV
W^2	[>8 (GeV/c^2)^2]	[>16 (GeV/c^2)^2]
E_{miss}	<48 GeV	<96 GeV

apply cuts simultaneously to the real and simulated samples to ensure that this is the case.

Our cuts fall into two general categories. The first set of cuts includes those that are necessary because of known limitations in the simulation. The event generator chose events only above $v_{\min}=0.015$ ($v\equiv Q^2/2M_N\nu$). We must therefore eliminate regions which in the data have a contribution from $v<v_{\min}$. We choose a cut of $v>0.025$. The data include events with scattering vertices upstream of the MMS. These are eliminated by a cut in z_{vertex} corresponding to the front of plate 0. Muons which penetrate a paddle counter near the edge adjoining the staves can veto themselves by producing a δ ray which hits a stave. While some of the effects of δ rays on track finding and resolution were empirically modeled, the effect on the trigger was neglected. For this reason an aperture cut of 0.5 cm was applied to the inside edges of the paddle counters. A study of real events whose muons passed near the edge of one paddle and triggered in three other paddles further downstream showed this to be adequate. These cuts remove about 20% of the data.

Additional cuts not absolutely required by the simulation are applied to remove events that are likely to have been badly misanalyzed or come from regions of poor resolution. We require that there be one and only one scattered track and that the reconstructed track be consistent with the recorded pattern of hit counters that triggered the event. Because there was no calorimeter counter in the gap following plate 0, the calorimeter cannot be used to improve ν resolution for events with vertices in plate 0. We eliminate these events and also, to allow for our finite vertex resolution, those in the first plate of module 1. Table II shows the set of kinematic cuts applied before analysis. Cuts in parentheses removed only an infinitesimal number of events. The regions removed are populated by the extreme tails of the resolution and energy-loss distributions. As an example, large missing energy indicates a catastrophic energy loss by the beam muon before scattering. Although such losses were included in our simulation, these events are badly misanalyzed. This second set of cuts removes about 20% of the events surviving the first set. There remain 394 522 (39 061) events in the 215- (93-) GeV sample.

B. Normalization correction and uncertainty

The normalization of the data is determined by the fixed relation between data and simulation achieved through the use of the prescaled sample of real beam tracks in the simulation. Deficiencies in the simulation are revealed by different losses to reconstruction failures and cuts in the real and simulated samples. This necessitates small corrections to the normalization. Before comparing real and simulated event losses, the number of rejected real events itself had to be corrected. This is because some rejection categories are dominated by background events which do not appear in the simulation. Thus samples of rejected events from each loss category had to be hand scanned to determine what fraction were real deep-inelastic-scattering events. Losses to cuts were also investigated in the same way. Of course, no correction to the normalization was made for the losses due to the "necessary" cuts discussed in Sec. VI A, that were expected to be different for the real and simulated samples. The final corrections to the 215- and 93-GeV samples were 0.020 ± 0.002 and 0.028 ± 0.003, respectively.

The uncertainty in this correction was but one of the systematic uncertainties in the normalization. Others include uncertainties in the target thickness, magnetic field calibration, beam energy, and trigger counter efficiencies. Some of these are discussed in more detail in Sec. VII C. We estimate that in total the normalization uncertainties for the 215- and 93-GeV samples are each 3%. Since some of these uncertainties are common to both samples, the uncertainty in the relative normalization between the two samples is smaller and is estimated to be 2.5%.

C. Extraction of $F_2(x,Q^2)$

The basis for the extraction of $F_2(x,Q^2)$ from the raw population of measured events is Eq. (16). Since our $d\sigma^{\text{gen}}$ includes radiative corrections, with an assumption

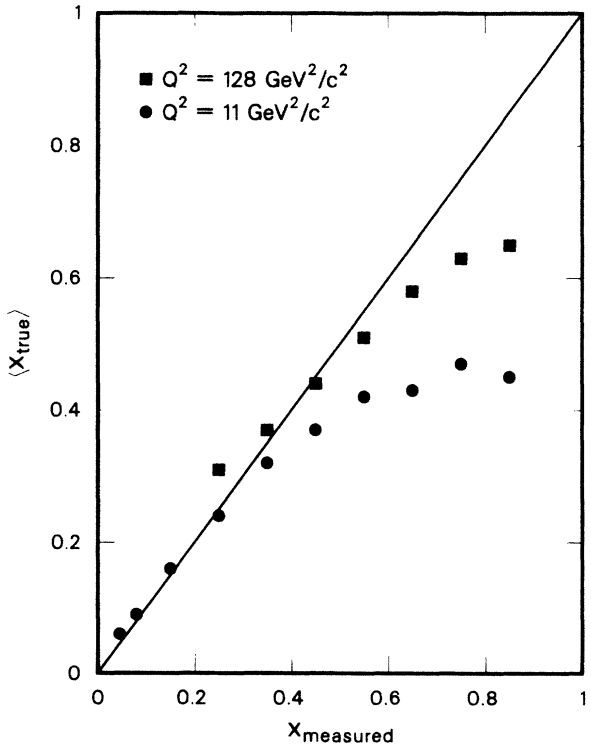

FIG. 29. Limiting effects of x resolution. Plotted is the average value of x_{true} for bins of x_{measured} as calculated in our apparatus simulation.

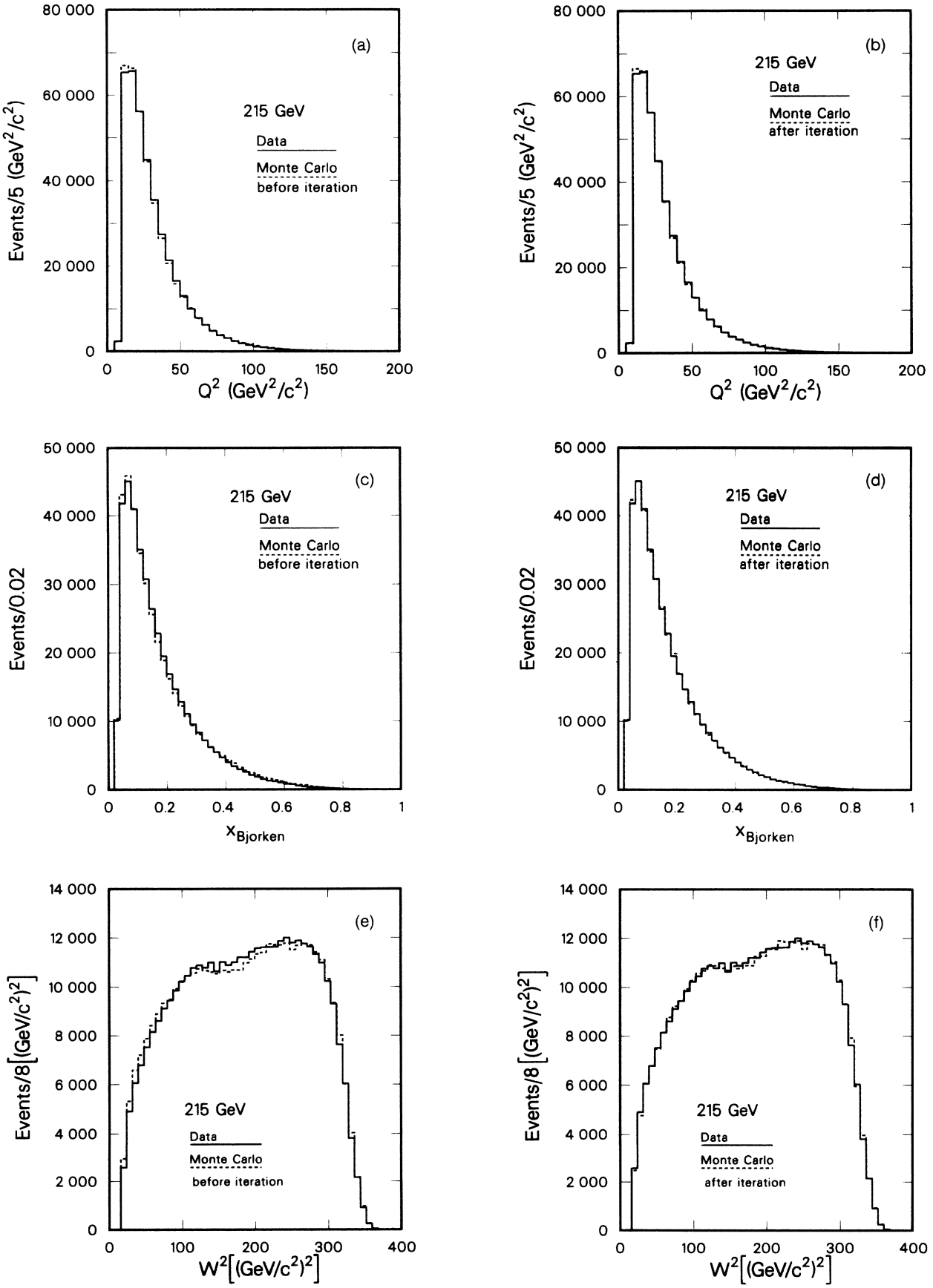

FIG. 30. Distributions of real and simulated events before and after the F_2^{gen} iteration procedure described in the text.

about R we can cancel all the kinematic factors in Eq. (16) and are left with an expression for F_2

$$F_2^{\text{meas}}(x,Q^2)=\frac{nD(x,Q^2)}{M(x,Q^2)}F_2^{\text{gen}}(x,Q^2)\ . \tag{19}$$

The normalization n now includes the corrections of the previous section. Besides providing the acceptance and radiative corrections to the data, Eq. (19) is also used to correct for resolution smearing effects. The rapidly varying cross section and the poor x resolution at low ν (see Figs. 15 and 16) make this resolution correction essential. This is illustrated in Fig. 29 where the knowledge of the true kinematics of Monte Carlo–generated events is used to show the average value of x_{true} for bins of x_{measured}. From this figure one can easily determine where data points will and will not appear in our final F_2 plots. For example, we cannot determine F_2 at $Q^2=128$ GeV$^2/c^2$, $x=0.75$, even though we have hundreds of events with (unsmeared) Q^2 and x in this bin and the acceptance of the MMS in this region is at its maximum. The resolution-induced feed down from the more populous low-x region [see Fig. 16(d)] makes it impossible to isolate a subset of the data at this Q^2 with an average true x of 0.75. Even at smaller x, there is a discrepancy between the measured and average true values of x for the same reason.

We correct for this feed down by using Eq. (19) and information of the type used to make Fig. 29. With real and simulated data divided into bins of measured x and Q^2, $(x_m,{Q_m}^2)$, the simulated events in each bin are used to determine $\langle x_{\text{true}}\rangle$ and $\langle {Q_{\text{true}}}^2\rangle$ for that bin. F_2^{gen} is calculated at these average true values of x and Q^2 and the resulting F_2^{meas} is assumed to refer to these same values. Equation (19) thus actually reads

$$F_2^{\text{meas}}(x({x_m},{Q_m}^2),Q^2({x_m},{Q_m}^2)) = \frac{nD({x_m},{Q_m}^2)}{M({x_m},{Q_m}^2)}F_2^{\text{gen}}(x({x_m},{Q_m}^2),Q^2({x_m},{Q_m}^2))\ , \tag{20}$$

where x and Q^2 are the average true values for the bin of measured variables $({x_m},{Q_m}^2)$.

The presence of F_2^{gen} in Eqs. (19) and (20) suggests that the F_2^{meas} yielded by this procedure is model dependent. Considering the simulation as merely an acceptance calculation or noting that $M(x,Q^2)$ is proportional to $F_2^{\text{gen}}(x,Q^2)$, demonstrates that, to first order, this is not the case. However, changing the model sufficiently could change the shapes of distributions enough to affect the smearing or the distribution of events within finite-sized bins. We remove this model dependence by empirically fitting F_2^{meas} and using this as the F_2^{gen} for a next iteration. This is done by weighting the existing simulated events by the ratio of new to old F_2^{gen}. The normalization correction due to the final set of cuts must be recalculated for each iteration. The values presented above are for the final iteration. The signals that the iteration has converged are (1) stability against further change and (2) identical distributions of data and simulation in many variables. In practice, one iteration satisfies both requirements. In Fig. 30 we show comparisons of data and Monte Carlo–simulated events in several variables before and after this iteration for the 215-GeV sample. Only the x and Q^2 dependence is explicitly changed. Most of the effect in all three variables shown is due to changing the x dependence of F_2. Note that the shaping is done in real (unsmeared) variables and that agreement in the resolution-dominated tails of measured distributions such as at large x depends on the accuracy of the apparatus simulation. The 93-GeV sample is done separately using the same procedure. When the iteration is complete, our parametrization is in fact a determination of F_2 over the entire x range, since true values of x from the entire range are smeared to yield agreement with the measured distribution. Away from the directly measured region, however, this determination is limited by the form of the parametrization and is not very sensitive.

Table III lists our measured values of F_2 in the raw form produced by Eq. (20), that is, with each point referred to its own average true x and Q^2. The entries have passed a final set of three cuts. We have eliminated points whose statistical uncertainty in F_2 is greater than 40%. We have eliminated points from regions with acceptance less than about 0.1 of the maximum, which corresponds to retaining the region $x>0.06$ and $Q^2>15$ (5) GeV$^2/c^2$ for the 215- (93-) GeV data. We have also eliminated measurements with minimal sensitivity in x by rejecting points for which smearing from other bins contributes greater than 90% of the events finally appearing in the bin. The correction to F_2 due to resolution smearing in the retained points is typically 10%, increasing at large x. Our results are not sensitive to the exact values of these cuts. The interpolation to our final grid of x and Q^2 is described in Sec. VII A.

VII. RESULTS

A. $F_2(x,Q^2)$

The raw F_2 measurements of Table III are interpolated onto a grid of fixed true x and Q^2 using the final fit (see Sec. VII B) as an interpolating function. The grid is chosen to be the same as that used to bin the events initially in measured x and Q^2. In Q^2 the effects of resolution smearing, and thus of the interpolation, are minor. This is aided by the approximate scaling of F_2. However, $\langle x_{\text{true}}\rangle$ may bear little resemblance to the corresponding measured x bin. For this reason the F_2 measurements were interpolated to the center of the bin in the final grid which contained $\langle x_{\text{true}}\rangle$ for that point, independent of which bin of measured x the point came from. Thus a point from a bin of measured x between 0.6 and 0.7 with $\langle x_{\text{true}}\rangle=0.42$ would be interpolated to $x_{\text{true}}=0.45$. This procedure can result in several bins producing measurements at the same true x and Q^2. A minimum requirement on our extraction method is that these measurements give the same value of F_2, that is, that they have the same ratio of real to simulated events. Figure 31 shows that $x=0.45$ section of our 215-GeV data. The agreement between points at the same Q^2 (originally from different bins of measured x) is good. These points are averaged after fitting to create our final $F_2(x,Q^2)$ results.

The resulting measurements of $F_2(x,Q^2)$ are presented separately for the two beam energies in Table IV and in

TABLE III. Raw $F_2(x,Q^2)$. For each measured bin, $F_2(x,Q^2)$ is presented at the average true x and Q^2 of that bin. Errors are statistical.

x	Q^2 (GeV$^2/c^2$)	$F_2(x,Q^2)$	x	Q^2 (GeV$^2/c^2$)	$F_2(x,Q^2)$
		93 GeV			
0.0965	5.30	0.3890±0.0105	0.3299	24.19	0.1722±0.0082
0.0992	7.13	0.3766±0.0099	0.3355	32.99	0.1601±0.0098
0.1050	9.53	0.3661±0.0114	0.3542	42.67	0.1187±0.0168
0.1161	12.36	0.3729±0.0228	0.3554	7.60	0.2337±0.0294
0.1591	5.29	0.3375±0.0092	0.3719	9.49	0.1773±0.0093
0.1584	7.26	0.3600±0.0084	0.3825	12.81	0.1602±0.0089
0.1575	9.78	0.3478±0.0074	0.3946	17.83	0.1495±0.0085
0.1601	13.30	0.3227±0.0077	0.4049	24.11	0.1374±0.0088
0.1703	17.67	0.3207±0.0104	0.4162	32.33	0.1169±0.0090
0.1904	22.25	0.2716±0.0201	0.4199	42.87	0.0964±0.0112
0.2343	5.33	0.2923±0.0111	0.4101	9.87	0.1240±0.0132
0.2384	7.15	0.2867±0.0088	0.4269	12.61	0.1141±0.0085
0.2401	9.74	0.2666±0.0075	0.4551	17.40	0.1092±0.0090
0.2398	13.28	0.2574±0.0073	0.4646	23.62	0.0911±0.0085
0.2403	17.94	0.2578±0.0080	0.4768	32.27	0.0764±0.0086
0.2435	24.22	0.2436±0.0091	0.4951	43.11	0.0542±0.0082
0.2647	31.06	0.2259±0.0163	0.5146	56.97	0.0499±0.0176
0.2802	5.69	0.2677±0.0344	0.4871	17.09	0.0888±0.0096
0.3067	7.16	0.2257±0.0103	0.5091	23.22	0.0830±0.0105
0.3131	9.62	0.2144±0.0083	0.5235	31.05	0.0550±0.0090
0.3189	13.13	0.2021±0.0081	0.5332	42.23	0.0467±0.0093
0.3284	17.94	0.1986±0.0083	0.5801	56.65	0.0444±0.0138
		215 GeV			
0.0736	16.31	0.3852±0.0053	0.3920	24.60	0.1416±0.0045
0.0781	18.13	0.3967±0.0652	0.4049	33.48	0.1319±0.0036
0.0925	18.29	0.3794±0.0028	0.4091	45.32	0.1276±0.0033
0.1026	23.70	0.3667±0.0028	0.4149	61.01	0.1086±0.0028
0.1175	30.61	0.3603±0.0045	0.4163	82.30	0.1073±0.0032
0.1326	34.22	0.2972±0.0306	0.4303	111.10	0.0927±0.0035
0.1563	18.68	0.3261±0.0037	0.4431	136.49	0.0788±0.0095
0.1564	25.06	0.3246±0.0029	0.4175	19.48	0.1282±0.0129
0.1575	33.56	0.3257±0.0027	0.4313	24.12	0.1188±0.0054
0.1686	43.68	0.3146±0.0030	0.4514	33.04	0.1047±0.0041
0.1917	55.67	0.2765±0.0055	0.4684	44.44	0.0919±0.0035
0.2438	18.68	0.2466±0.0044	0.4855	60.45	0.0720±0.0028
0.2439	25.25	0.2428±0.0034	0.4822	80.84	0.0661±0.0027
0.2415	33.85	0.2469±0.0030	0.4933	109.42	0.0672±0.0035
0.2427	45.74	0.2446±0.0029	0.5148	143.17	0.0407±0.0037
0.2470	61.64	0.2336±0.0030	0.4815	32.60	0.0892±0.0052
0.2670	78.30	0.2113±0.0045	0.5159	44.07	0.0670±0.0037
0.2922	92.56	0.2120±0.0410	0.5255	59.27	0.0566±0.0033
0.3220	18.45	0.1940±0.0052	0.5353	79.92	0.0492±0.0030
0.3255	24.91	0.1852±0.0040	0.5575	107.94	0.0394±0.0029
0.3306	33.82	0.1830±0.0034	0.5812	142.99	0.0382±0.0040
0.3307	45.67	0.1762±0.0031	0.6056	186.69	0.0394±0.0161
0.3352	61.68	0.1644±0.0030	0.5880	79.71	0.0393±0.0036
0.3421	83.72	0.1589±0.0033	0.6187	107.23	0.0296±0.0031
0.3598	106.28	0.1427±0.0054	0.6026	137.44	0.0285±0.0042
0.3780	18.58	0.1514±0.0063	0.6511	182.23	0.0120±0.0043

Fig. 32. We have assumed $R=0$ and have made no correction for Fermi motion. The F_2 values thus represent $F_2^{Fe}/56$. The effects of Fermi motion and nonzero R are discussed below. As a consequence of the above procedure, the measurements refer to F_2 at the indicated true x and Q^2 and are not bin averages. Because of this a few of the points appear to have $y>1$. This occurs when the center of the Q^2 bin lies above the kinematic limit and the original $\langle Q_{\text{true}}{}^2\rangle$ was near the lower edge of the bin. If the y dependence is important, these points can be ignored or the raw measurements of Table III can be used. The listed and plotted errors are statistical. Systematic errors are discussed in detail in a later section. As systematic errors caused correlated shifts

TABLE IV. The structure function $F_2(x,Q^2)$ for iron on a fixed grid of x and Q^2. $R=0$ is assumed and no Fermi-motion correction has been applied.

x	Q^2 (GeV$^2/c^2$)	F_2 (93 GeV)	F_2 (215 GeV)	F_2 (combined)
0.08	5.54	0.3997±0.0108		0.3997±0.0108
	7.52	0.3905±0.0103		0.3905±0.0103
	10.2	0.3855±0.0120		0.3855±0.0120
	18.8		0.3894±0.0026	0.3894±0.0026
	25.6		0.3906±0.0030	0.3906±0.0030
0.15	5.54	0.3430±0.0094		0.3430±0.0094
	7.52	0.3657±0.0085		0.3657±0.0085
	10.2	0.3531±0.0075		0.3531±0.0075
	13.9	0.3321±0.0074		0.3321±0.0074
	18.8	0.3364±0.0109	0.3309±0.0037	0.3315±0.0035
	25.6	0.3017±0.0223	0.3296±0.0030	0.3291±0.0030
	34.8		0.3330±0.0023	0.3330±0.0023
	47.2		0.3303±0.0031	0.3303±0.0031
	64.1		0.3148±0.0062	0.3148±0.0062
0.25	5.54	0.2811±0.0102		0.2811±0.0102
	7.52	0.2764±0.0085		0.2764±0.0085
	10.2	0.2576±0.0072		0.2576±0.0072
	13.9	0.2480±0.0070		0.2480±0.0070
	18.8	0.2481±0.0077	0.2413±0.0043	0.2429±0.0038
	25.6	0.2365±0.0088	0.2373±0.0033	0.2372±0.0031
	34.8	0.2351±0.0170	0.2386±0.0029	0.2385±0.0029
	47.2		0.2370±0.0029	0.2370±0.0029
	64.1		0.2300±0.0029	0.2300±0.0029
	87.1		0.2253±0.0048	0.2253±0.0048
	118.3		0.2479±0.0479	0.2479±0.0479
0.35	7.52	0.1961±0.0084		0.1961±0.0084
	10.2	0.1874±0.0059		0.1874±0.0059
	13.9	0.1791±0.0058		0.1791±0.0058
	18.8	0.1808±0.0061	0.1729±0.0039	0.1752±0.0033
	25.6	0.1578±0.0076	0.1686±0.0030	0.1671±0.0028
	34.8	0.1500±0.0091	0.1692±0.0031	0.1672±0.0029
	47.2	0.1192±0.0168	0.1628±0.0029	0.1615±0.0029
	64.1		0.1545±0.0028	0.1545±0.0028
	87.1		0.1534±0.0032	0.1534±0.0032
	118.3		0.1475±0.0056	0.1475±0.0056
0.45	10.2	0.1009±0.0107		0.1009±0.0107
	13.9	0.0989±0.0074		0.0989±0.0074
	18.8	0.1092±0.0071	0.1082±0.0109	0.1089±0.0059
	25.6	0.1032±0.0055	0.1062±0.0048	0.1049±0.0036
	34.8	0.0929±0.0059	0.1035±0.0022	0.1022±0.0021
	47.2	0.0756±0.0070	0.1009±0.0022	0.0986±0.0021
	64.1		0.0882±0.0019	0.0882±0.0019
	87.1		0.0844±0.0020	0.0844±0.0020
	118.3		0.0833±0.0025	0.0833±0.0025
	160.7		0.0739±0.0089	0.0739±0.0089
0.55	25.6	0.0611±0.0077		0.0611±0.0077
	34.8	0.0444±0.0072		0.0444±0.0072
	47.2	0.0403±0.0080	0.0522±0.0028	0.0509±0.0026
	64.1	0.0443±0.0105	0.0469±0.0027	0.0467±0.0026
	87.1		0.0457±0.0023	0.0457±0.0023
	118.3		0.0412±0.0030	0.0412±0.0030
	160.7		0.0353±0.0025	0.0353±0.0025
0.65	118.3		0.0210±0.0022	0.0210±0.0022
	160.7		0.0171±0.0025	0.0171±0.0025
	218.3		0.0137±0.0039	0.0137±0.0039

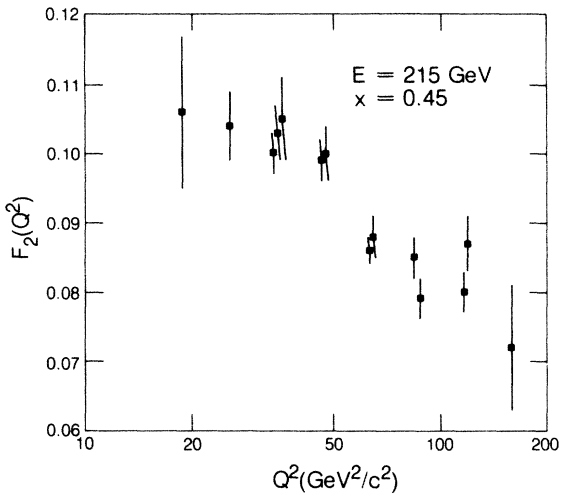

FIG. 31. The $x=0.45$ bin of our 215-GeV $F_2(x,Q^2)$ measurement, after interpolation to the grid of true x and Q^2, but prior to averaging of measurements assigned to the same point. Values at the same point have been displaced slightly in Q^2 for clarity.

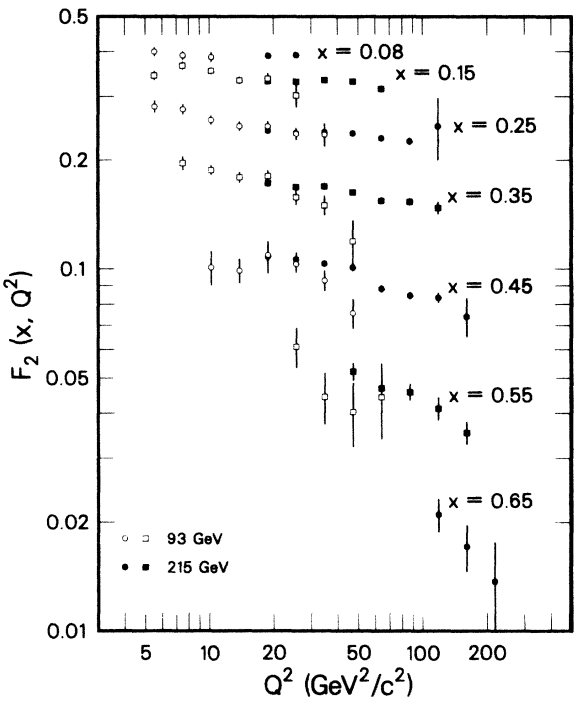

FIG. 32. F_2 for nucleons in iron as a function of Q^2 at various fixed values of x. 93- and 215-GeV data are shown separately. Errors are statistical.

in the data we do not attach systematic uncertainties to individual points. One powerful test of the internal consistency of our data is the quite good agreement of the 93- and 215-GeV measurements (Fig. 32). Although the χ^2 for the overlap is 33 for 15 degrees of freedom (DF), over half of this comes from two points. When these are ignored, the χ^2 drops to 14/13 DF. In these data the scaling violation is plainly visible at $x>0.2$. We treat this quantitatively below using lowest-order quantum chromodynamics.

B. Comparison to lowest-order QCD

Fits are performed to the data of Table III prior to the interpolation and coalescence of points in x. For convenience in fittings, the more gentle interpolation to Q^2 bin centers is performed before fitting. The core of our fitting program was modified from a routine kindly provided by R. M. Barnett. Its operation and use are described in Ref. 42 and summarized here.

The fitting program uses the Altarelli-Parisi method[16] to calculate the Q^2 dependence of F_2 at fixed x predicted by lowest-order QCD for the flavor-singlet case. No correction is made for the neutron excess in iron. Starting from parametrizations of $F_2(x)$ and $G(x)$ at a reference value of $Q^2\equiv Q_0^2$ and an initial estimate of the QCD scale parameter Λ, the routine numerically integrates the set of simultaneous differential equations of Eq. (10) from Q_0^2 to each Q^2 at which there are F_2 measurements. There is one singlet-quark and one gluon equation for each bin of x with bin center x_i. At each Q^2, the predictions for $F_2(x_i,Q^2)$ are interpolated using a cubic spline to the average true x of each measured point at that Q^2. The predicted and measured values are compared and the minimization program MINUIT (Ref. 43) is used to vary Λ and the Q_0^2 parametrization so as to minimize the χ^2. Note that operationally Q_0^2 is largely symbolic, as the data at all Q^2 are used to determine all the parameters.

Our parametrization at $Q_0^2=5.535\ \text{GeV}^2/c^2$ is

$$F_2(x,Q_0^2)=\frac{5}{18}\sum_{i=1}^{2N_f} xf_i(x)$$

$$=Ax^{\alpha}(1-x)^{\beta}(1+ax)+B(1-x)^{\gamma}\ , \qquad (21)$$

$$G(x,Q_0^2)=C(1-x)^{\delta}\ .$$

The two terms of the F_2 parametrization are inspired by the conceptual division of the quarks into "valence" and "sea" distributions. The $\frac{5}{18}$ is the average charge squared of the SU(2)-singlet (valence) or SU(4)-singlet (sea) quarks. This interpretation is not essential, however, and all we actually demand of Eqs. (21) is that they be sufficiently general. In our standard fit, we fix $a=0$, $\gamma=8$, and $\delta=5$. The variation of these parameters is discussed below. The parameter α, β, A, B, and Λ are fitted. The parameter C determines the fraction of the nucleon's momentum that is carried by gluons. With the other parameters known, C is fixed by normalization of the fractional-momentum distributions:

$$\int_0^1 [\tfrac{18}{5}F_2(x)+G(x)]dx=1 \qquad (22)$$

which gives

$$C=(1-\gamma)\left\{1-\frac{18}{5}\left[A\mathrm{B}(1+\alpha,1+\beta)\times\left[1+\frac{a(1+\alpha)}{2+\alpha+\beta}\right]+\frac{B}{1-\delta}\right]\right\}. \qquad (23)$$

TABLE V. Results of lowest order QCD fits to $F_2(x,Q^2)$. $F_2(x,Q_0^2)=Ax^{\alpha}(1-x)^{\beta}(1+ax)+B(1-x)^{\gamma}$; $G(x,Q_0^2)=C(1-x)^{\delta}$; a, γ, δ fixed; C from momentum sum rule; α, β, A, B, and Λ fitted. Errors are statistical and represent $\Delta\chi^2=1$ excursions in the fit.

Fit	Λ (MeV/c)	α	β	A	B	a	χ^2/DF	Comment
(a) Standard: $\gamma=8$, $\delta=5$, $a=0$	225±43	1.00 ±0.10	3.80 ±0.15	2.74 ±0.44	0.410 ±0.036		154/91	$Q_0^2=5.535$ GeV$^2/c^2$
(b) Fit a	225±43	0.51	3.97	0.84	0.948	3.24	153/90	
(c) $\gamma=12$	230±44	0.71	3.56	1.92	0.350		153/91	
(d) $\alpha=B=0$, fit a	217±43		3.43	0.37		3.73	160/92	
(e) Fit 93 GeV normalization	176±43	0.99	3.83	2.67	0.409		148/90	Normalized lowered by 2.0±0.8%
(f) Standard, EMC data (Ref. 52)	159±25	0.65	3.29	1.41	0.258		230/153	$Q_0^2=5.50$ GeV$^2/c^2$

B is the beta function, $B(z,w)=\Gamma(z)\Gamma(w)/\Gamma(z+w)$. We find that 48% of the nucleon's momentum is carried by gluons at Q_0^2.

The result of the standard fit applied simultaneously to the 215- and 93-GeV measurements is shown in Fig. 33. The family of curves traces the Q^2 variation of F_2 at various values of x from the single global fit. We find a value for Λ of 225 MeV/c with a statistical error of 43 MeV/c. The values of the other fitted parameters and their statistical errors are listed as entry (a) of Table V. Each error represents the allowed excursion of the parameters for a unit increase of χ^2. The marginal χ^2 of the fit (154/91 DF) implies that this is an underestimate of the actual uncertainties, either due to the inadequacy of lowest-order QCD, to our structure of assumptions, or to the presence of systematic errors. As discussed below, the uncertainties due to these possibilities outweigh those of a purely statistical origin. Entries (b)—(d) of Table V show the minor effects of changing the form of the parametrization. The parameters are sufficiently correlated to allow a restructuring of the parametrization to give nearly the same $F_2(x,Q_0^2)$, without affecting Λ. Changing Q_0^2 from 5.535 to 25 GeV$^2/c^2$ has no effect on Λ.

C. Systematic uncertainties

We define systematic uncertainties to mean uncertainties whose origins are purely experimental and affect the measured cross section. Uncertainties that affect the interpretation of the measured cross section, say in terms of Λ, will be discussed in Sec. VII D. Neither the estimation nor the presentation of systematic effects is an exact sci-

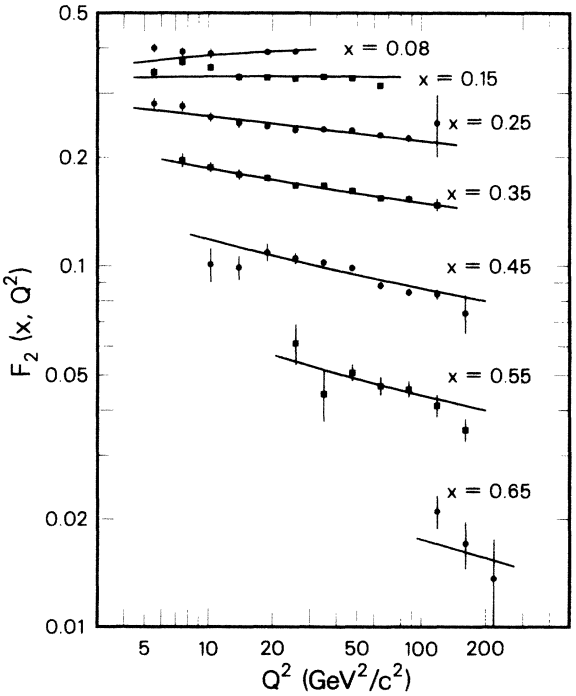

FIG. 33. Results of the lowest-order QCD fit applied simultaneously to the 93- and 215-GeV measurements of $F_2(x,Q^2)$. These measurements have been averaged after fitting. The curves represent the Q^2 dependence of F_2 at various fixed values of x predicted by the single global fit.

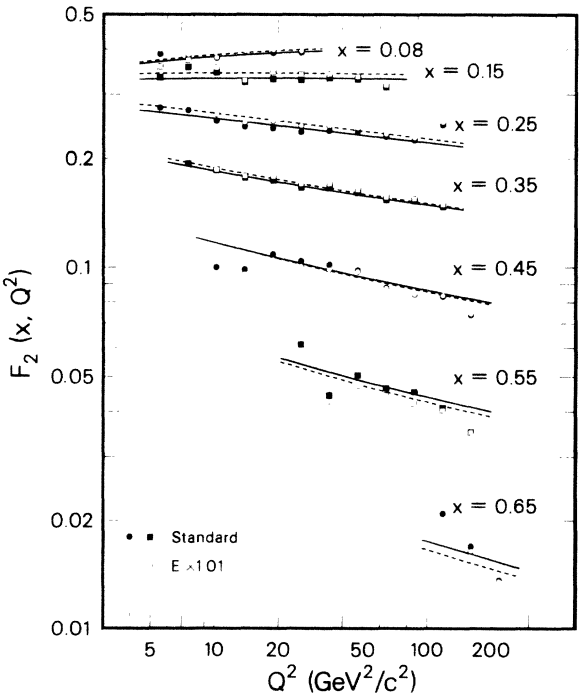

FIG. 34. Systematic effects of a 1% shift in beam energy ($\approx 2\times$ the estimated uncertainty). The normalization of the 93-GeV data has been allowed to float in each case. The solid (dashed) curves are the QCD fit to the standard (shifted) data. The difference in Λ between the fits is 20 MeV/c.

TABLE VI. Systematic uncertainties in Λ. The total indicates the sum of the other entries in quadrature.

Source	Uncertainty	δΛ (MeV/c)
MMS B-field calibration	0.5%	< 10
Beam energy	0.5%	10
Trigger efficiency (systematic)	0.5%	16
Trigger efficiency (statistical)	(see text)	10
Resolution smearing	(see text)	50
93/215-GeV normalization	2.5%	60
Total		82

ence. We begin by making a catalog of possible sources of experimental uncertainty. An example would be the MMS magnetic-field calibration. We next estimate the magnitude of the uncertainty in each source and how it would affect our analysis. We then reanalyze the data with each source in turn changed to reflect its uncertainty, and we observe the effect on our measured and fitted $F_2(x,Q^2)$. We also make various tests of internal consistency to reveal possible problems. The changes to $F_2(x,Q^2)$ from systematic effects are typically correlated. Thus assigning errors to individual measured points is misleading. Showing bands of uncertainty on our F_2 plots is also unsatisfactory—the top of one band may correspond to the bottom of another. We will thus give only a representative example of the effect on $F_2(x,Q^2)$, but concentrate on the global effects on our fitted results, notably on Λ. Our catalog of systematic effects is listed in Table VI.

The first source of systematic uncertainty to be checked was the MMS magnetic-field calibration. From the evidence presented in Sec. IV A we conclude that the uncertainty in the field is, conservatively, ±0.5%. Since both the beam system and the calorimeter were calibrated to the spectrometer, the effect of a 0.5% MMS miscalibration would be an overall shift in the measured energy scale. This would be easy to simulate—change the incident beam energy and MMS field by 0.5% in the simulation and analyze with the original values—but time consuming and expensive. Instead, we reason backward from the existing simulated events, a procedure to be used often in this section. By using the existing simulated events we have fixed the trajectory, that is, the angle, curvature, and triggering probability of each track in the MMS. We reinterpret the true momentum of both the incident and scattered tracks in accordance with the new assumed field value. If $\bar{B}=\epsilon B$ (with $\epsilon=1.005$), we find $\bar{Q}^2=\epsilon^2 Q^2$, $\bar{x}=\epsilon x$, and $\bar{y}=y$. Had we actually redone the simulation, this change in kinematics would have caused a corresponding change in the cross section for each event. We therefore assign each simulated event a new true x and Q^2 and a weight given by

$$\frac{\overline{d\sigma}}{d\sigma}=\frac{1}{\epsilon^3}\frac{F_2(\epsilon x,\epsilon^2 Q^2)}{F_2(x,Q^2)} \tag{24}$$

as implied by Eq. (17). This method is not exact. Radiative corrections, MCS, etc., are left at the old energy scale and $\bar{x}=\epsilon x$ must break down at the kinematic limit. For small adjustments in B, however, it should be adequate. It has the advantage that by using the same events, the modified results are highly correlated to the original set, and thus small changes are readily visible in spite of statistical fluctuations. The most notable change caused by the adjustment in B is the shift in normalization. This, as well as the other effects of this section, has been taken into account in the estimate of the normalization uncertainty quoted earlier. The changes in shape are minor, as expected from an overall scale change. As indicated in Table VI, the uncertainty in Λ from this source is less than 10 MeV/c.

We expect more substantial effects from a differential shift of the beam energy (measured exclusively in the beam system) relative to that of the scattered track. The precision of the calibration of beam to spectrometer rules out such a relative shift of greater than a few tenths of a percent. We consider a total uncertainty of ±0.5% to allow for uncertainty due to the discrepancy between the two MMS polarities and for possible effects in the

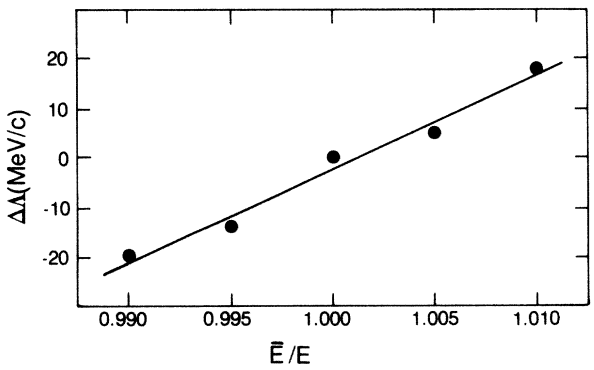

FIG. 35. The dependence of Λ on systematic error in the beam energy calibration relative to that of the MMS. The estimated uncertainty is 0.005. The line is a fit to the points with slope (19 MeV/c) per (1% shift).

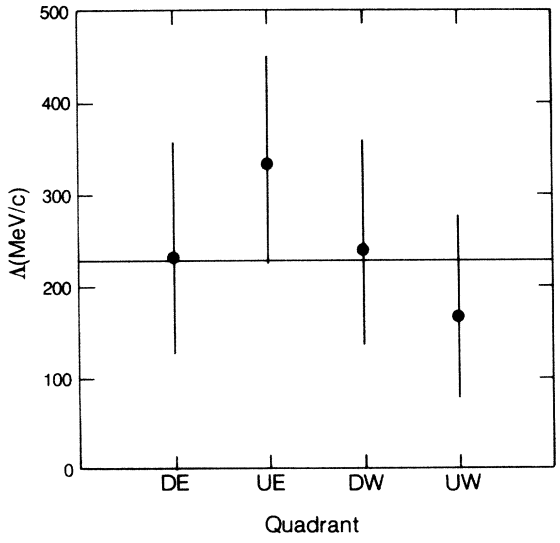

FIG. 36. Λ by quadrant. The 215-GeV data has been sorted by quadrant and $F_2(x,Q^2)$ extracted and fit separately for each. The line shows the value of Λ fit to the total 215-GeV sample (227 MeV/c).

analysis of the average energy loss of the beam muon en route to the vertex. The effect of beam energy shifts was determined in the same fashion as the previous case. Figure 34 shows the effect of such an energy shift, magnified to $\bar{E}/E=1.01$ for clarity. We have allowed the 93-GeV normalization to adjust to that of the 215-GeV data. As mentioned above, the corresponding points of each set are highly correlated and only their separation is meaningful. The error bars have thus been suppressed. The curves show the fit to each case. They also demonstrate the effect of changing Λ, in this case by 20 MeV/c, on the slope of $F_2(Q^2)$. Figure 35 shows the response of Λ to beam energy miscalibration. Our estimate of the uncertainty in Λ from this source is ± 10 MeV/c.

After mapping the efficiency of the trigger counters, there are residual uncertainties, both statistical and systematic. We can estimate the global systematic uncertainty in the trigger efficiency by comparing events that trigger in different parts of the spectrometer or events that penetrate different numbers of paddle counters. We feel that any global efficiency offset is limited to $\pm 0.5\%$. Even a uniform offset in efficiency can affect the shape of the cross section because the number of paddles penetrated, and thus the sensitivity to the efficiency of individual paddles, varies with Q^2. We find that a 0.5% change in efficiency changes Λ by 16 MeV/c. Even if there is no systematic offset in the efficiency maps, the statistical errors in the maps may affect our results. In any kinematic region with a large geometrical acceptance, the statistical errors in many map cells are averaged and there is no effect. However, at low Q^2 only small portions of the spectrometer are illuminated and only a limited amount of averaging takes place. We probed this possibility by varying by one statistical standard deviation the efficiency of the single most critical map cell (or rather, the four cells, one in each paddle of trigger bank 6). From this worst case we estimate that the statistical uncertainty in the efficiency maps leads to an uncertainty in Λ of ± 10 MeV/c. As an overall check, we compare results extracted separately from the events entering the four quadrants of the apparatus as seen by the beam. In Fig. 36 we show Λ as separately fitted in the four quadrants using our 215-GeV data. This figure should be considered in the light of Fig. 19, which indicates how different the quadrants actually are.

Another source of systematic uncertainty is resolution smearing, or rather our ability to model and correct for it. Included here are effects due to the use of the calorimeter for resolution improvement, and thus possible calorimeter miscalibration. We study this by varying the degree to which the calorimeter is used. The two extreme cases are relaxing the missing energy requirement (see Sec. III D), thus using the calorimeter in all events (with the same weighting scheme as before), and ignoring the calorimeter information totally. The kinematic cuts described in the previous section were chosen to minimize the effects of these changes. The uncertainty in Λ from this source is estimated to be ± 50 MeV/c.

The major source of uncertainty in Λ is the relative normalization of our 93- and 215-GeV data sets. Since Λ determines the slope of the Q^2 dependence of F_2 at fixed x, and our low-Q^2 data comes from one set and high Q^2 from the other, this is no surprise. We estimate the uncertainty in the relative normalization to be $\pm 2.5\%$. This causes a ± 60 MeV/c uncertainty in Λ. We can also allow the relative normalization to float in the global fit. Table V, entry (e) shows the result of this fit. The result is to lower the 93-GeV normalization by $(2.0\pm 0.8)\%$, within the estimated uncertainty. Alternatively, we can normalize directly by comparing the 15 points where the data sets overlap. The first normalization check is, of course, model dependent; the second is more sensitive to R. The direct normalization indicates that the 93-GeV event sample should be increased by $(2.9\pm 1.5)\%$. Eliminating the same two points that contributed the most to the χ^2 of the comparison between the two data sets reduces the normalization shift to $1.5\pm 1.5\%$. Unless otherwise indicated, all results of this section refer to the original (separate, absolute) normalizations, including the corrections discussed in the previous section.

As another consistency check, we can separately fit the 93- and 215-GeV measurements. Unfortunately, the resulting smaller Q^2 ranges and our limited 93-GeV statistics reduce the significance of this comparison. The results are not terribly satisfying. The fit of the 93-GeV data gives $\Lambda=633\pm 148$ MeV/c, 2.6 statistical standard deviations higher than the 215-GeV value of 227 ± 55 MeV/c. Inspecting Fig. 32, it is apparent that the slopes of the 93-GeV data are somewhat steeper. In fact, there has been some attempt[44] to attribute physical significance to a similar effect in the data of the European Muon Collaboration (EMC) (though not by the experimenters). Our opinion is that systematic errors must be reduced in all of the experiments before such effects are to be considered significant. On the positive side, the agreement between the result of the combined fit and that of the 215-GeV data alone is excellent. The effects of shifting the relative normalization indicate that this agreement is not simply due to the 215-GeV data dominating the combined fit.

Table VI concludes with an estimate that our total systematic uncertainty in Λ is 82 MeV/c, the sum in quadrature of the individual entries. This estimate is obviously accurate only to the extent that our catalog of sources is complete. It is apparent, however, that the systematic uncertainty already dominates the statistical uncertainty.

D. Phenomenological uncertainties affecting Λ

Beyond the experimental uncertainties discussed in the previous section lie questions of interpretation. We have measured Λ by assuming that the cross section [Eq. (17) with $R=0$], the parametrization [Eq. (21)], and lowest order perturbative QCD are a complete description of deep-inelastic scattering. In this section we explore the effects of relaxing or varying the various pieces of this assumption. Table VII summarizes the results.

We start with the cross section and begin by varying R. In this exercise, the measured cross section remains constant; the measurement is simply apportioned differently between F_2 and R. We choose $R=0.1$ as an upper limit based on the measurements of R to be discussed below. Even this small change decreases Λ by 100 MeV/c.

TABLE VII. Effects of various phenomenological assumptions on the fitted value of Λ.

Assumption	ΔΛ (MeV/c)	χ^2/DF
Standard	(Λ=225)	154/91
$R=0.1$	−100	142/91
Fermi motion correction	+20 to +60	149 to 151/91
$x>0.15$	+5	134/81
Gluon exponent =6	−25	152/91
Higher-order QCD	+50 (estimated)	
Target mass correction	+15	155/91
Include $1/Q^2$ term	−25 or more (see text)	152/91

Another matter of interpretation concerns Fermi motion. As we have defined it in Eq. (17), our measured $F_2(x,Q^2)$ refers to an average over the nucleons in an iron nucleus. To translate this into F_2 for a free nucleon, we can try to remove the known effects of the nuclear environment such as binding energy and its manifestation as Fermi motion. This correction has been demoted in importance by the discovery[45] of another nucleus-dependent effect which is larger in the x region covered by our data. This "EMC effect" is discussed in Sec. VII E. The situation of Fermi motion itself is surprisingly murky. The models we use are described in Appendix B. In brief, Fermi motion is primarily an x dependent phenomenon, and thus has a limited effect on Λ. Depending on the model used, we find that Λ increases by 20—60 MeV/c when Fermi motion corrections are applied. Above the low-Q^2 region ($Q^2<10$ GeV$^2/c^2$), the EMC effect has no observed Q^2 dependence.[46,47]

Our data extend into the kinematic region known to contain scaling violations due to the crossing of the charm threshold.[33] We have made no detailed attempt to correct for this, but rather observe the effect of removing the region in question. Before the interpolation to x bin centers, we eliminate all measurements with $x<0.15$. This results in an increase in Λ by only 5 MeV/c.

We have already discussed the minor effects of varying some of the more arbitrary features of our parametrization at Q_0^2. One feature, however, has an unambiguous physical interpretation. This is the exponent δ which determines the "hardness" of the gluon momentum spectrum. In inclusive muon scattering we cannot directly measure the gluons. This is unfortunate, because it has been noted[48] that Λ and this exponent can be strongly correlated. As mentioned earlier, the nonsinglet information available from neutrino scattering allows a more constrained determination of the gluon sector. The CERN-Dortmund-Heidelberg-Saclay (CDHS) neutrino collaboration[18] has found the exponent δ to lie in the range 5—7, but the actual precision of this result has been questioned.[49] Our standard fit uses $\delta=5$. Raising this to $\delta=6$ decreases Λ by 25 MeV/c. Figure 37 traces further the dependence of our best fit value of Λ on the assumed value of δ.

As discussed in Sec. I D, our lowest-order QCD fits neglect the contribution of higher powers of $\ln Q^2$ and powers of $1/Q^2$ in the Q^2 dependence of F_2 at fixed x. This is known as the "leading-logarithm, leading-twist" approximation. The next-to-leading-logarithm contribution can be incorporated into the Altarelli-Parisi evolution equations, but we have not done so. From the work of others[49,50] we estimate that these higher-order corrections increase Λ by approximately 50 MeV/c. The $1/Q^2$ terms are, in general, not calculable. An exception is the "target-mass correction" which can be taken into account[51] by replacing the variable x with

$$\xi=\frac{2x}{1+(1+4x^2M_N^2/Q^2)^{1/2}} . \tag{25}$$

In our Q^2 and x ranges, this effect should be small. When this transformation is made we find that Λ in-

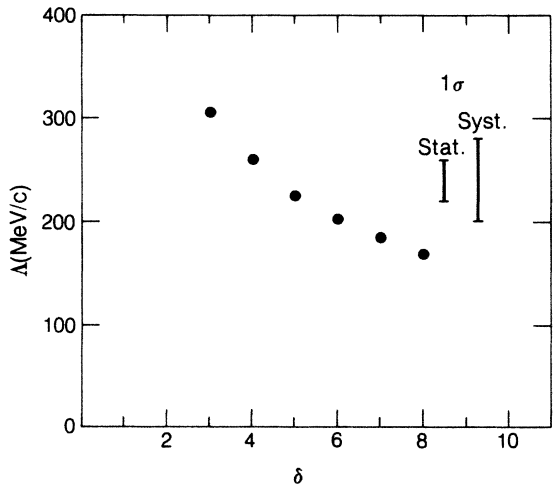

FIG. 37. The correlation between our best-fit value of Λ and the value assumed for δ, the exponent of $(1-x)$ in the gluon distribution. For comparison, the statistical and systematic uncertainties in our standard fit of Λ are shown.

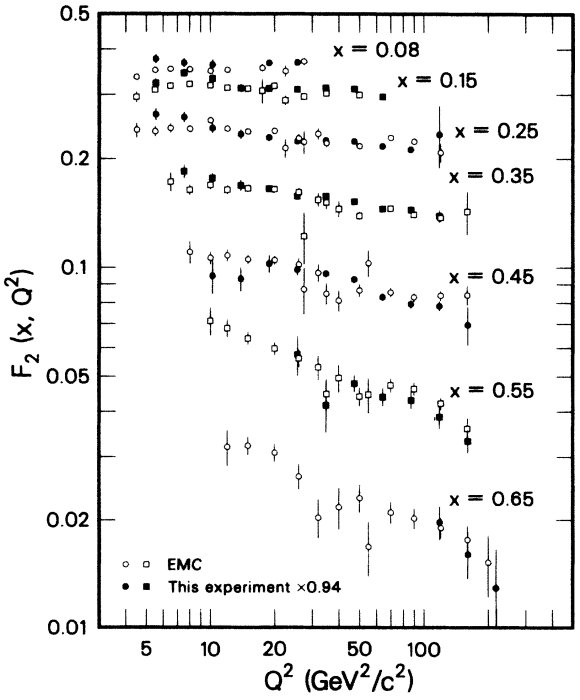

FIG. 38. A comparison of our measured $F_2(x,Q^2)$ (multiplied by 0.94) to the EMC's iron-target measurement (Ref. 52).

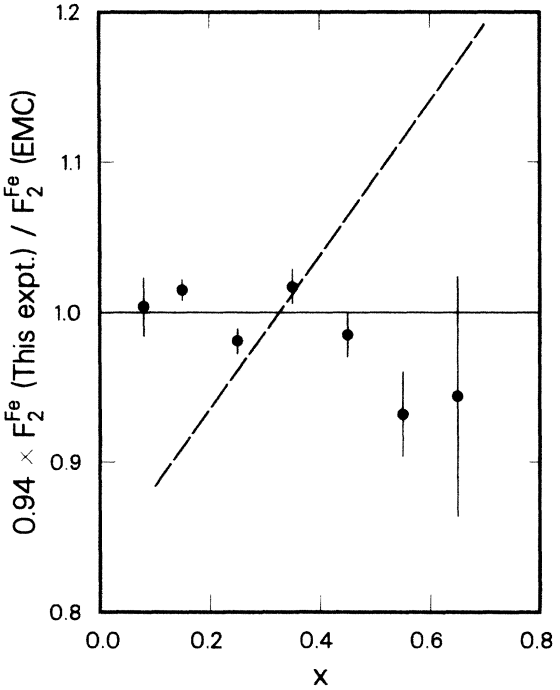

FIG. 39. The ratio of our F_2(Fe) measurements (multiplied by 0.94) to the EMC's (Ref. 52) as a function of x, for $Q^2>20$ GeV$^2/c^2$, interpolated to $Q^2=50$ GeV$^2/c^2$. The dashed line shows the trend of EMC's F_2 (deuterium)/F_2(Fe) from Ref. 45.

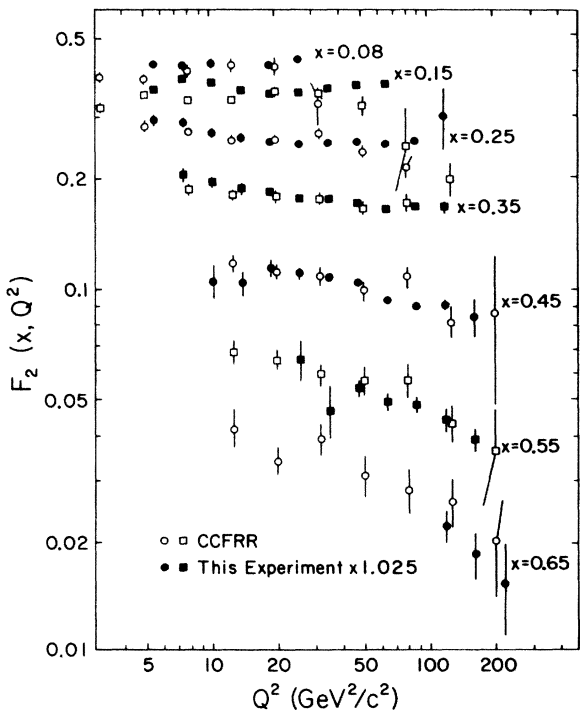

FIG. 40. Our measured $F_2(x,Q^2)$ (multiplied by 1.025) compared to F_2^ν from CCFRR (Ref. 53), modified as suggested by the quark model [Eq. (26)]. Both data sets assume $R=0.1$ and neither has been corrected for Fermi motion.

creases by 15 MeV/c. Considerably more freedom in Λ is allowed if we include an arbitrary $1/Q^2$ dependence in our parametrization. We first simply multiply our F_2 parametrization by $(1+k/Q^2)$ with k determined by the fit. Λ drops by 100 MeV/c, with an improvement in χ^2 from 154/91 DF to 130/90 DF. To gain sensitivity, the EMC investigated $1/Q^2$ terms by combining their muon-proton data with lower-Q^2 electron-proton data from SLAC (Ref. 50). They allowed the x dependence of the $1/Q^2$ term to vary and found that this dependence was consistent with $kx^2(1-x)^2$. If we use this form and fix $k=0.45$, which is the approximate level observed by the EMC, Λ drops by 25 MeV/c with a negligible improvement in χ^2. If we instead try to use our data to determine k, we find $k\approx 4$, $\Lambda=30$ MeV/c, and $\chi^2=144/90$ DF. It is not clear that anyone is doing anything but quantifying systematic errors with these fits. The fact remains that our experiment alone cannot rule out large $1/Q^2$ corrections to lowest-order QCD.

E. Comparison with other experiments

The most direct comparison we can make is to data from the European Muon Collaboration (EMC) (Ref. 52). Part of their data was taken on an iron target at beam energies similar to ours. Their spectrometer, however, was completely different from the MMS, and thus we can hope that some of the sources of systematic errors are different for the two experiments. Figure 38 shows a comparison of our results with the EMC's iron-target measurements. Both measurements are averaged over the various beam energies, both assume $R=0$, and neither has been corrected for Fermi motion. For purposes of this comparison only, our values of F_2 have been multiplied by a factor of 0.94, determined from the x dependence comparison discussed below. This normalization is consistent with the 3% systematic uncertainty quoted by each experiment. Except for the region of $Q^2<10$ GeV$^2/c^2$, the agreement is excellent. Table V includes an entry for a fit to the EMC's data using our fitting routine and assumptions. These fitted parameters are consistent with the EMC's published results,[50] although the assumptions made here are slightly different. It should be noted that while the individual parameters of $F_2(x)$ at Q_0^2 appear different in fits (a) and (f), the actual values of $F_2(x,Q_0^2)$ are quite similar after the 6% shift indicated above.

In Fig. 39 the ratio of our F_2^{Fe} (multiplied by 0.94) to that of the EMC for $Q^2>20$ GeV$^2/c^2$ is displayed as a function of x. Fits (a) and (f) of Table V have been used to interpolate each data point to $Q^2=50$ GeV$^2/c^2$ prior to averaging. The errors shown are statistical; systematic uncertainties from our data alone are of comparable magnitude. The EMC has reported differences of up to 15% between deuterium and iron in the x dependence of F_2 (Ref. 45). The existence of these discrepancies, not explained by Fermi motion, have been confirmed at SLAC (Refs. 46 and 47). The dashed line in Fig. 39 shows the trend of $F_2(d)/F_2$(Fe) for the EMC's measurements. We, of course, cannot make the deuterium-iron comparison directly. However, from the evidence of Fig. 39, we can provide support for the existence of the discrepancy by noting that our iron measurements agree quite well with the EMC's iron measurements, but are distinctly different from their deuterium measurements. This is true even at

$x < 0.3$ where a lower-Q^2 experiment sees no deuterium-iron difference.[47]

We can also compare our results to those of charged-current neutrino experiments. Here the comparison is somewhat less direct, due to the difference in the coupling to quarks between the weak and electromagnetic probes used. The parton model predicts that

$$F_2^{\mu N}(x) \approx \tfrac{5}{18} F_2^{\nu N}(x) \left[1 + \frac{3}{5} \left[\frac{s+\bar{s}}{q+\bar{q}} \right] \right] , \tag{26}$$

where the $\frac{5}{18}$ factor is the average electric charge squared of the quarks and q, $\bar{q}$, s, and $\bar{s}$ are the momentum distributions of all quarks, all antiquarks, strange quarks, and strange antiquarks in a nucleon. This relation is only approximate because of the threshold behavior in the neutrino interaction where an s quark must be turned into a massive c quark. Figures 40 and 41 show our results compared to those from the Caltech-Columbia-Fermilab-Rochester-Rockefeller (CCFRR) neutrino experiment, which also has an iron target.[53] For the comparison, CCFRR's F_2 has been modified as directed by Eq. (26) and our F_2 has been multiplied by 1.025. Because CCFRR has presented their results assuming $R = 0.1$ and has made a correction for the neutron excess in iron, our F_2 has been modified to be consistent with these assumptions. Neither data set has been corrected for Fermi motion. The CCFRR group fits a value of Λ consistent with ours.[53]

We can compare our measurement of $\Lambda_{\rm LO} = 225 \pm 43(\text{stat}) \pm 82(\text{syst})$ MeV/c to the results of other investigations of the strong coupling constant $\alpha_S(Q^2)$. In e^+e^- annihilation, α_S appears whenever gluons are present. For example, the value of α_S can be determined by observing the modifications due to gluon emission to the two-jet structure of events. There are various methods of characterizing this modification, but all appear to be subject to substantial uncertainties from the (nonperturbative) fragmentation of the primary quarks and gluons into the observed hadrons. At a center-of-mass energy $\sqrt{s} \approx 30$ GeV, values of α_S typically between 0.13 and 0.20 are found.[54] If we use Eq. (9) with $Q^2 = s$ and $N_f = 5$ to turn these results into measurements of $\Lambda_{\rm LO}$, we find $\Lambda_{\rm LO} = 60$–400 MeV/c. The expectation that the hadronic decay of the Υ is dominated by $\Upsilon \to 3$ gluons allows a determination of α_S from the observed decay widths of the Υ (Ref. 55). It is found that $\alpha_S(M_\Upsilon) = 0.158 \pm 0.011$. This translates into $\Lambda_{\rm LO} = 80 \pm 30$ MeV/c. One of the interpretational difficulties here is the appropriateness of using M_Υ as the argument of α_S. It is apparent that in e^+e^- annihilation, as in deep-inelastic scattering, the confrontation of theory with experiment is limited as much by questions of interpretation as by experimental precision.

F. Measurement of R

Although our results discussed previously have assumed that $R (\equiv \sigma_L/\sigma_T)$ is fixed (usually $R = 0$), our overlapping measurements of $F_2(x,Q^2)$ taken at different beam energies allows us to measure R. At fixed Q^2 and ν (i.e., at fixed Q^2 and x) we have fixed the four-momentum of the virtual photon, independent of the muon beam energy. However, this does not exhaust the photon's quantum numbers; it also carries polarization. We can isolate the dependence on the virtual-photon polarization and write[9]

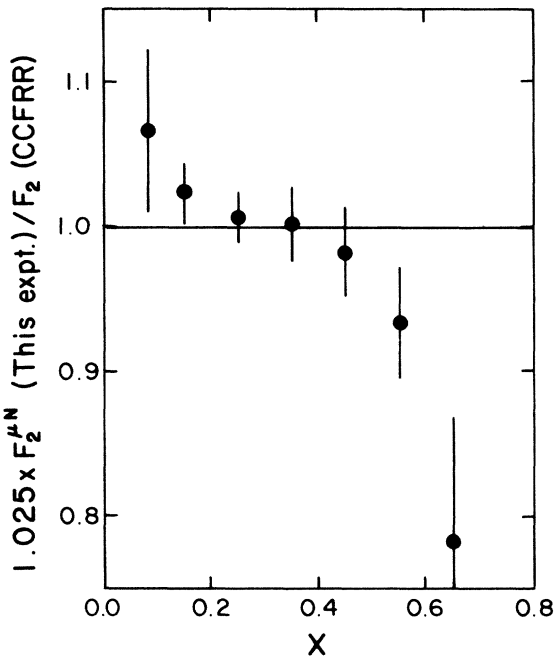

FIG. 41. A comparison of the x dependence of our $F_2^{\mu\text{Fe}}$ and $F_2^{\nu\text{Fe}}$ from CCFRR (Ref. 53). Measurements for $Q^2 > 18$ have been averaged after interpolation to $Q^2 = 50$ GeV$^2/c^2$.

$$S \equiv \frac{1}{\Gamma_T} \frac{d^2\sigma}{dQ^2 d\nu} = \sigma_T (1 + \epsilon R) , \tag{27}$$

with Γ_T and σ_T the flux and cross section for transversely polarized virtual photons, and the polarization

$$\epsilon = \frac{1 - (\nu/E) - (Q^2/4E^2)}{1 - (\nu/E) + (\nu^2/2E^2) + (Q^2/4E^2)} . \tag{28}$$

At fixed ν and Q^2, varying the muon beam energy changes the polarization of the "beam" of virtual photons, and R is obtained from the slope of S vs ϵ. To extract R, we recall that our measurement of F_2 is actually a measurement of the cross section that is independent of R, coupled to an assumption about R. Using this cross section, we get a measurement of R for each point where the two data sets overlap:

$$R(x,Q^2) = \frac{S_2 - S_1}{S_1\epsilon_2 - S_2\epsilon_1} = \frac{F_2^{\,2}(x,Q^2) - F_2^{\,1}(x,Q^2)}{F_2^{\,1}(x,Q^2)\epsilon_2 - F_2^{\,2}(x,Q^2)\epsilon_1} , \tag{29}$$

where the indices 1 and 2 refer to the 93- and 215-GeV beam energies, respectively, and F_2^i is the measured F_2 with $R = 0$.

It is clear that this measurement of R will be sensitive to systematic experimental differences between the data sets. Beginning with the F_2 measurements of Table III we find that the average true x and Q^2 can be different

TABLE VIII. R measurements. Errors are statistical. The final entry is a global average.

x	Q^2 (GeV$^2/c^2$)	ϵ(93 GeV)	ϵ(215 GeV)	R
0.1633	18.18	0.5870	0.9464	−0.057±0.085
0.2421	18.31	0.8359	0.9772	−0.160±0.185
0.3252	18.20	0.9184	0.9880	−0.378±0.291
0.3863	18.20	0.9445	0.9916	−0.550±0.325
0.2437	24.73	0.6682	0.9564	0.011±0.138
0.3277	24.55	0.8390	0.9776	0.758±1.071
0.3985	24.35	0.8996	0.9855	−0.269±0.461
0.4480	23.87	0.9265	0.9891	−5.002±23.776
0.2531	32.45	0.4220	0.9258	−0.003±0.137
0.3331	33.41	0.6766	0.9574	0.659±0.518
0.4106	32.91	0.8104	0.9739	0.610±1.164
0.4641	32.66	0.8603	0.9803	−4.844±11.585
0.5025	31.83	0.8904	0.9842	−1.857±0.975
0.3425	44.17	0.4131	0.9246	1.045±0.727
0.4145	44.10	0.6269	0.9512	1.557±0.1732
0.4818	43.78	0.7436	0.9656	−4.027±3.908
0.5246	43.15	0.7975	0.9723	−4.764±11.744
0.5001	58.71	0.5274	0.9389	0.732±1.821
0.5528	57.96	0.6382	0.9526	−0.316±0.525
0.2278	22.80			−0.064±0.057

for the two beam energies due to differences in smearing, energy loss, etc. To correct for this we interpolate each measurement to the average x_{true} and $Q_{\text{true}}{}^2$ of both measurements using the final F_2 fit for each energy. We eliminate measurements for which Δx_{true} or $\Delta Q_{\text{true}}{}^2$ is greater than 10% to minimize the sensitivity to this procedure.

The resulting measurements of R are listed in Table VIII and shown in Fig. 42. Points with uncertainties greater than 10 units of R have not been plotted. In Table IX and Fig. 43 we show separately the dependence of R on Q^2 and x. Because no strong dependence is apparent, we average all the measurements and find $R=-0.06$ with a statistical error of 0.06. The kinematic range covered by the measurements is $20<\nu<70$ GeV and $18<Q^2<60$ GeV$^2/c^2$, with $\langle\nu\rangle=53$ GeV and $\langle Q^2\rangle=23$ GeV$^2/c^2$. In this region, QCD predicts that R is everywhere less than 0.06. (See Ref. 53 for a convenient parametrization of R_{QCD}.) In Sec. VII D we observed the effect of varying R on our fitted results. This procedure can be used to infer a model dependent value of R. We find that, at fixed normalization, the χ^2 of our QCD fits is minimized for $R\approx 0.1$ (see Table VII).

The greatest contribution to the systematic uncertainty in R comes from the uncertainty in the relative normalization of the 93-GeV and 215-GeV data sets. This uncertainty was estimated in Sec. VI B to be 2.5%. In Sec.

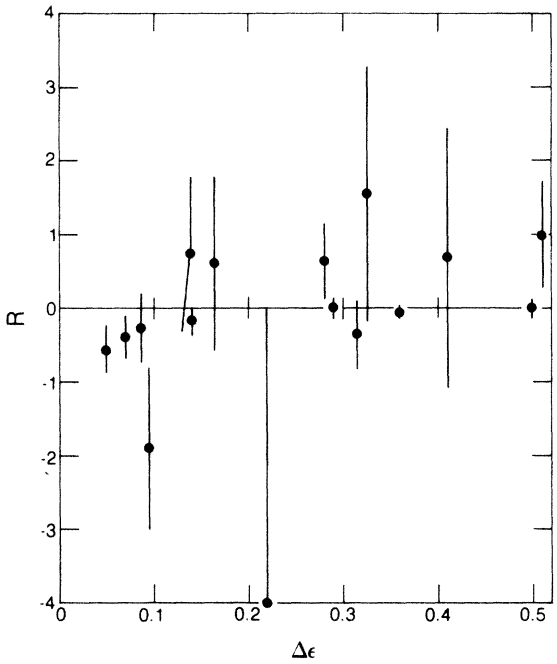

FIG. 42. Measurements of R from the comparison of our 93- and 215-GeV data. All measurements with statistical uncertainties less than 10 are shown vs $\Delta\epsilon$, the difference in virtual-photon polarization due to the different beam energies at each fixed (x,Q^2). Errors are statistical.

VII C we calculated a model-dependent correction to the relative normalization by including it as a variable in our QCD fit (with $R=0$). The result was a −2.0% correction to the 93-GeV normalization. We can attempt a model- and R-independent normalization as suggested in Ref. 56 by looking in the low-ν region where both polarizations are near 1. Unfortunately, if we restrict ourselves to $\epsilon_{1,2}>0.9$, we are left with only three points and a correction to the 93-GeV normalization of $(-2.8\pm3.6)\%$. If we make these corrections, R becomes 0.01 ± 0.06 or 0.04 ± 0.06 for the −2.0% or −2.8% corrections, respectively.

We also estimate the contributions to the systematic uncertainty in R from the rest of the effects considered previously in fitting F_2. These uncertainties are shown in Table X. Included in the table is the contribution of a 2.5% relative normalization uncertainty. Our final result is $R=-0.06\pm0.06(\text{stat})\pm0.11(\text{syst})$. For comparison, the EMC has reported $R=0.00\pm0.10$ in muon-proton interactions for $60<\nu<160$ GeV and the same average Q^2 (Ref. 56). Electron-nucleon scattering experiments at SLAC found $R=0.22\pm0.1$ at lower Q^2 (Ref. 57). No experiment observes any significant kinematic dependence in R.

TABLE IX. R vs Q^2, R vs x.

Q^2 (GeV$^2/c^2$)	$\langle x\rangle$	R	x	$\langle Q^2\rangle$	R
18.2	0.197	−0.120±0.073	0.194	19.8	−0.055±0.067
24.7	0.258	−0.004±0.130	0.274	30.4	0.02 ±0.12
32.5	0.265	0.034±0.133	0.392	21.4	−0.37 ±0.25
44.2	0.358	0.95 ±0.65	0.541	52.3	−0.57 ±0.43
58.0	0.549	−0.27 ±0.47			

TABLE X. Systematic uncertainty in R. The total shows the sum of the other entries in quadrature.

Source	Uncertainty	δR
MMS B-field calibration	0.5%	0.0049
Beam energy	0.5%	0.0644
Trigger efficiency (systematic)	0.5%	0.0102
Trigger efficiency (statistical)	(see text)	0.0018
Resolution	(see text)	0.0509
93/215-GeV normalization	2.5%	0.0743
Total		0.1113

G. Search for a μ^+-μ^- asymmetry

In considering only the radiatively corrected process of Fig. 44(a), we have neglected both the higher-order QED process of Fig. 44(b) and the weak-neutral-current interaction of Fig. 44(c). Although too small to measure directly, these processes can give measurable effects through their interference with the one-photon-exchange diagram.[58] Weak-interaction effects have been observed in eN interactions in atomic physics[59] and in high-energy eN interactions[60] by searching for a parity-violating signal.

Recently the Bologna-CERN-Dubna-Munich-Saclay (BCDMS) Collaboration at CERN reported an asymmetry between the cross sections for μ^+N and μ^-N interactions:[61]

$$A \equiv \frac{d\sigma_L^+ - d\sigma_R^-}{d\sigma_L^+ + d\sigma_R^-} . \tag{30}$$

The L and R refer to the predominant helicities of the μ^+ and μ^- beams due to their production in the forward decay of pions. Because this asymmetry violates neither parity nor charge conjugation, both the two-photon and weak neutral processes contribute. After correction for the former, BCDMS finds an asymmetry consistent with the Weinberg-Salam model prediction.

Although all of our 93-GeV data and nearly all of our 215-GeV data was taken with a μ^+ beam, Table I shows that we do have a small amount of μ^- data. While statistically insufficient to probe the expected level of asymmetry (see below), the measurement has value as a check of the systematic consistency of our data. It should be pointed out that a serious attempt to measure this asymmetry would require more than additional μ^- statistics. It would also demand better control of possible systematic differences. Although both the μ^+ and μ^- data sets represent roughly equal amounts of east- and west-bending spectrometer settings, the μ^- running was done all in one block and at a beam intensity of only about $\frac{1}{3}$ that of the μ^+ beam. Our Monte Carlo simulation takes into account known time-, intensity-, and beam-space-dependent effects, but no attempt was made to make these the same for the μ^+ and μ^- running.

The asymmetry[62] predicted by the parton and Weinberg-Salam models is

$$A_{\rm WS} = -4\sin^2\theta_W \left[\frac{9G}{20\sqrt{2}\pi\alpha}\right] g(y)Q^2 ,$$
$$g(y) = \frac{1-(1-y)^2}{1+(1-y)^2} . \tag{31}$$

Here θ_W is the Weinberg angle, $G \approx 10^{-5}/M_p$ is the weak-interaction coupling constant, and $y = \nu/E$. This approximation assumes Bjorken scaling, an isoscalar target, and polarization of ± 1 for the beams. It neglects Cabibbo mixing and nonvalence quarks. Because the currently accepted value of $\sin^2\theta_W \approx 0.23$ is near $\frac{1}{4}$, the asymmetry is nearly independent of the actual polarization of the beam. The expected asymmetry is then $A_{\rm WS} = -1.45\times 10^{-4} g(y)Q^2$. The two-photon asymmetry is expected to be smaller and opposite in sign.[61]

We measure the asymmetry by extracting $F_2(x,Q^2)$ for the μ^+ and μ^- samples separately following the procedures described in Sec. VI C. For each bin of x and Q^2 for which there is an F_2 measurement for both samples, the μ^- measurement is interpolated to the average x and Q^2 of the μ^+ measurement. We then calculate $g(y)Q^2$ and A for each point. Figure 45 shows the asymmetry measurements after binning in $g(y)Q^2$. The line is the best fit of $A = a + bg(y)Q^2$ to all the points before binning. The result of this fit is

$$A = (6.9\pm 6.7)\times 10^{-3} - (1.4\pm 2.4)\times 10^{-4} g(y)Q^2$$

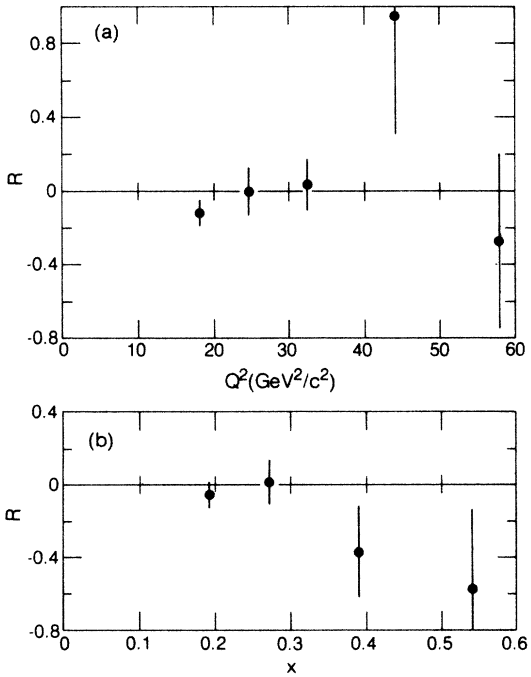

FIG. 43. (a) R vs Q^2; (b) R vs x.

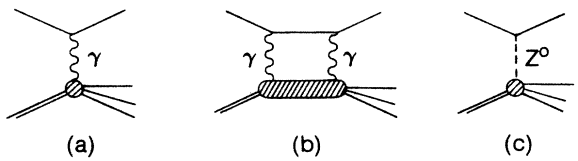

FIG. 44. Contributions to deep-inelastic scattering. (a) One-photon exchange; (b) two-photon exchange; (c) weak neutral current.

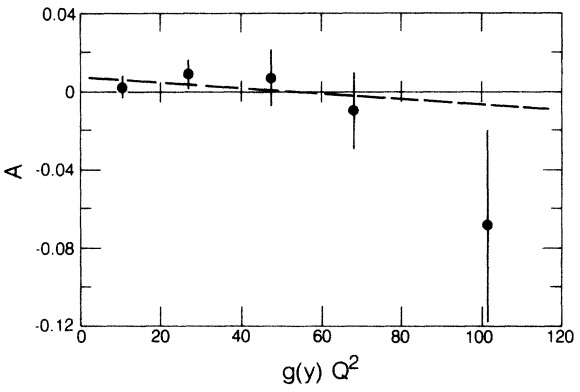

FIG. 45. The $\mu^+ - \mu^-$ asymmetry vs $g(y)Q^2$. The dashed line is a linear fit. Errors are statistical.

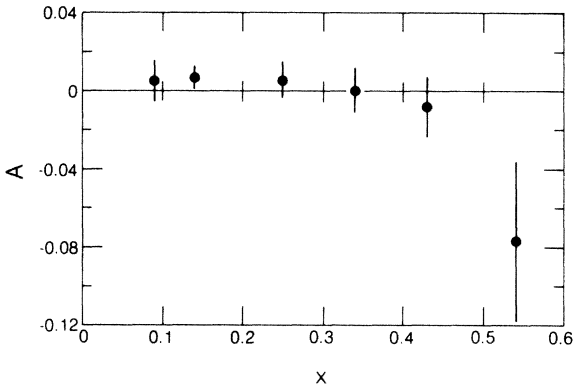

FIG. 46. The $\mu^+ - \mu^-$ asymmetry vs x.

with a χ^2 of 48 for 44 DF. As the statistical error in the slope b indicates, setting $b=0$ has a negligible effect on χ^2.

While, as expected, our lack of μ^- statistics bars us from the realm of the weak interaction asymmetry, this measurement adds to the confidence we have in our ability to correct for systematic effects due to beam intensity and phase space. It also rules out an unexpectedly large contribution from the one-photon—two-photon interference term in muon scattering from iron that might affect the deuterium-iron comparison. Figure 46 shows the asymmetry vs x. There is no significant asymmetry at the 2% level out to $x=0.5$.

VIII. SUMMARY AND CONCLUSIONS

We have built and operated the multimuon spectrometer, an iron-target spectrometer calorimeter in the muon beam at Fermilab, to observe muon-nucleon interactions with high luminosity and broad acceptance. We have measured the cross section for the deep-inelastic scattering of muons on nucleons in iron at incident energies of 93 and 215 GeV. Using the known properties of the electromagnetic interaction, we have extracted from the measured cross-section measurements of the structure function $F_2(x,Q^2)$ with a statistical precision of better than 2% over a wide kinematic range. These measurements, extending in Q^2 from 5 to 200 GeV$^2/c^2$, are presented in Table IV and in Fig. 32. Our measurements are in good agreement with results from similar contemporary experiments. The agreement in x dependence between our data and that of the European Muon Collaboration's iron-target experiments is especially notable in the light of the controversy surrounding the recently discovered A dependence of $F_2(x)$.

We have compared our measurements to the predictions of lowest-order quantum chromodynamics (QCD) in which the Q^2 dependence of F_2 at fixed x is calculable. QCD reproduces the qualitative pattern of scaling violation seen in the data. Within our set of phenomenological assumptions, we measure the QCD scale parameter $\Lambda_{\rm LO}$ to be 230 ± 40(stat) MeV/c. With the same assumptions, we estimate the systematic uncertainty in $\Lambda_{\rm LO}$ to be 80 MeV/c. This value of Λ agrees within quoted errors with the determinations from other deep-inelastic-scattering experiments using muons and neutrinos. While the statistical precision and Q^2 range of the new experiments represent an improvement over those of several years ago, systematic uncertainties still limit the precision with which we measure Λ to about 100 MeV/c. If we relax some of our assumptions about imprecisely known parameters, we can again generate ≈ 100 MeV/c uncertainties in Λ. These uncertainties will diminish as the quantities in question, notably R and the shape of the gluon spectrum, become better known, but progress in this direction has been slow and difficult. We have compared our F_2 measurements from the 93- and 215-GeV beam energies and measured $R=-0.06\pm0.06$(stat)±0.11(syst), a value consistent with zero, but with enough uncertainty to affect Λ substantially. Similarly, the rejection of large contributions to the observed scaling violations from $1/Q^2$ term in favor of the logarithmic behavior predicted by QCD is difficult, especially with little constraint on the form of such terms. Although the confirmation from deep-inelastic-scattering experiments of QCD as the theory of the strong interactions must still be considered somewhat qualitative, the improved agreement between the various experiments represents a distinct clarification of the experimental situation, without which no progress can be possible.

ACKNOWLEDGMENTS

The construction and operation of the multimuon spectrometer were made possible by the technical skills of Fred Goozen, Garvie Hale, Duck Lucas, Tim Nuzum, and Tom Weber. Also instrumental were Leslie Bauman and others of the Fermilab staff. This work was supported by the Director, Office of Energy Research, Office of High Energy and Nuclear Physics, High Energy Physics Division of the United States Department of Energy under Contract Nos. DE-AC03-76SF00098, DE-AC02-76CH03000, and DE-AC02-76ER03072. One of us (P.D.M.) was supported by the National Science Foundation during the years 1975—77.

APPENDIX A: RADIATIVE CORRECTIONS

As summarized in Sec. V C we correct the deep-inelastic-scattering cross section Eq. (17) for processes involving the radiation of photons [Figs. 21(a)—21(d)]. We

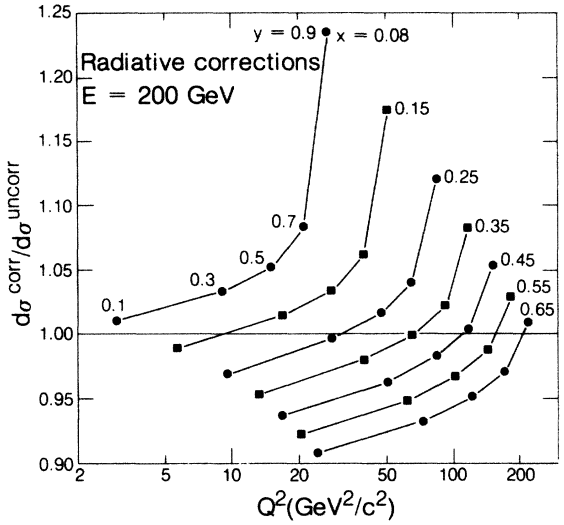

FIG. 47. The effect of radiative corrections on the deep-inelastic-scattering cross section.

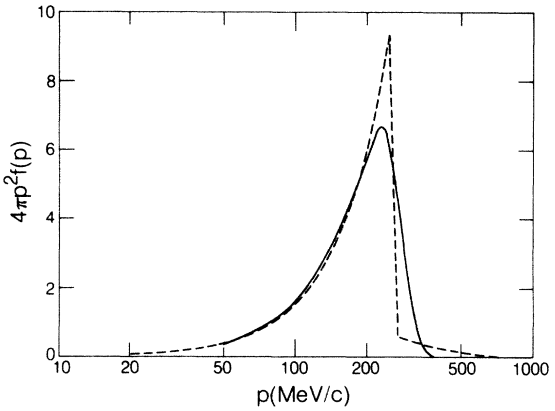

FIG. 48. Fermi-momentum spectrum of nucleons in iron (solid curve). Also shown is the spectrum used in Ref. 66 (dashed curve).

do this by using the method of equivalent radiators[38] in which these internal bremsstrahlung diagrams are replaced by an equivalent amount of radiation emitted separately from the primary (deep-inelastic) scatter. The connection to the primary scatter remains in the amount of radiation, which is effectively that due to a Q^2-dependent number of radiation lengths

$$t=\frac{3\alpha}{4\pi}[\ln(Q^2/m_\mu{}^2)-1]\ . \tag{A1}$$

This radiation has the characteristic spectrum

$$P(y)dy=\left[1-y+\frac{3}{4}y^2\right]\frac{dy}{y}\ , \tag{A2}$$

where $y=(E-E')/E$ is the muon's fractional energy loss in the radiator. We radiatively correct the cross section in our event simulation by explicitly radiating a photon before the interaction with a probability and spectrum given by Eqs. (A1) and (A2). Since the Q^2 of the interaction is not known before the interaction, we use a large limiting value, to be corrected later. The divergent spectrum is cut off at $y_{\min}=0.001$. We invoke the peaking approximation, in which the muon's direction is unaffected by the photon emission, and the incident muon, with its energy degraded, is handed to the deep-inelastic generator. Besides the energy loss due to the process of Fig. 21(a), the cross section is modified by the processes of Fig. 21(b) and 21(c). The vertex and vacuum-polarization corrections [Fig. 21(b)] have the effect of multiplying the cross section by[38]

$$1+\delta(Q^2)=1+\frac{2\alpha}{\pi}[-\tfrac{14}{9}+\tfrac{13}{12}\ln(Q^2/m_\mu{}^2)]\ . \tag{A3}$$

We cogenerate the wide-angle bremsstrahlung (WAB) events of Fig. 21(c) using the per nucleon cross section[63]

$$\frac{d^2\sigma^{\rm WAB}}{dv\,dy}=\frac{1}{A}\frac{4Z^2\alpha^3}{2M_NE}\frac{y(1-y+y^2/2)}{(1-y)v^2}G(Q_{||}{}^2)\ , \tag{A4}$$

where $G(Q_{||}{}^2)$ is the nuclear form factor integrated over the component of q perpendicular to the incident muon direction. Finally, photon emission from the outgoing muon is simulated. The actual Q^2 of the event is then calculated and excess radiation is removed.

To investigate the effects of the radiative corrections, we have convolved numerically the deep-inelastic-scattering cross section with the radiative effects of Eqs. (A1)—(A3). The results of this calculation are shown in Fig. 47 for a beam energy of 200 GeV and the same $F_2(x,Q^2)$ used in the event simulation routine.[37] Plotted as $d\sigma^{\rm corr}/d\sigma^{\rm uncorr}$ as a function of Q^2 for fixed x. For a fixed observed cross section, $d\sigma^{\rm corr}/d\sigma^{\rm uncorr}>1$ corresponds to a *downward* correction in measured F_2. Changing the beam energy to 100 GeV has an effect very similar to sliding the plot down by a factor of 2 in Q^2. Although it was not included in our event simulation, in this calculation we also studied the contribution of the radiative tail from elastic scattering. This correction turns out to be invisible where we have data, reaching a maximum of $<1\%$ at the highest Q^2, lowest x point of the 93-GeV data.

After the cuts restricting the region over which we present $F_2(x,Q^2)$ are applied, the contribution of WAB is never greater than 3%. The number of simulated WAB events found in each bin of measured x and Q^2 is subtracted from both the real and simulated events before the F_2 extraction procedure of Sec. VI C. The iteration of the $F_2^{\rm gen}$ used in the simulation does not modify the WAB events.

APPENDIX B: FERMI MOTION

In analyzing our data we have calculated the various kinematic quantities using Eqs. (1) and thus have assumed that the laboratory frame and the target rest frame were the same. In our experiment, this is fine if the target is considered to be an iron nucleus, as in most of our results where we have presented $F_2^{\rm Fe}/56$. In order to interpret our results in terms of F_2 for a single nucleon, we must remove the effects of nuclear binding, beginning with Fermi motion. Although the energy scale of Fermi motion seems negligible compared to that of our 200-GeV muons, a proton with a Fermi momentum of 240 MeV/c can change the effective beam energy by over 50 GeV. The

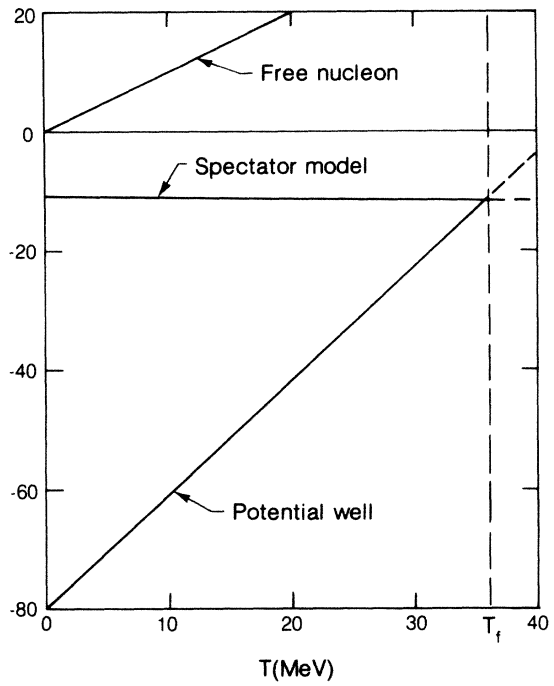

FIG. 49. The effects of binding. Total energy vs kinetic energy is shown for a free nucleon and for the two nuclear models of iron discussed in the text.

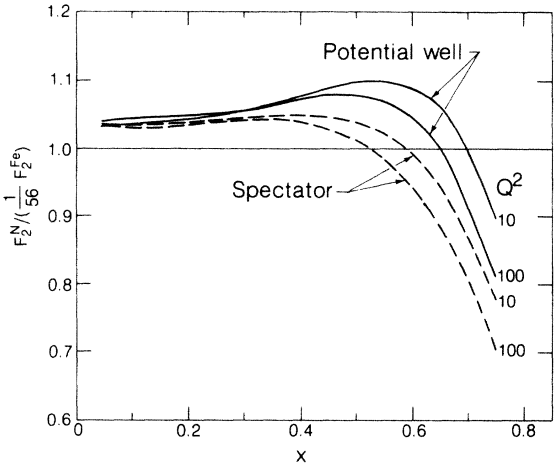

FIG. 50. The effects of Fermi motion on F_2. The two nuclear models discussed in the text have been used to calculate F_2^{Fe} given F_2^N. The result is shown as a function of x for $Q^2=10$ and 100 GeV$^2/c^2$. The dashed curves are the results of Ref. 66.

treatment of Fermi motion and binding can be broken into three nearly independent phases. The first is the determination of the momentum spectrum of the target nucleons. The second is the treatment of binding energy. The third is the calculation of the effect on the cross section, and thus on the measurement of F_2.

The nucleon momentum spectrum we use is derived from measurements of the nuclear form factor,[64] augmented by a tail inferred from studies of antiproton production below threshold.[65] A zero-temperature, spherically symmetric Fermi gas has a kinetic energy (T) spectrum proportional to $T^{1/2}$ below the Fermi energy T_f. Our spectrum has a form corresponding to a finite temperature plus the tail:

$$\frac{dN}{dT} \propto \begin{cases} T^{1/2}/(1+e^{(T-36)/6.4)}), & T<70 \text{ MeV}, \\ T^{-2.6}, & 70<T<385 \text{ MeV}, \\ 0, & T>385 \text{ MeV}. \end{cases} \tag{B1}$$

This spectrum as a function of nucleon momentum is shown as the solid curve in Fig. 48. Also shown in the figure is the spectrum used by Bodek and Ritchie.[66] The interpretation of the tails in these spectra is not entirely clear. Rather than single high-energy nucleons, the tail may represent a collective effect in the nucleus, such as the scattering off a higher-mass cluster of nucleons.

The treatment of binding is, in effect, the calculation of the energy component of the target nucleon's four-momentum. The various models thus provide a function $E(p)$ giving the energy for any momentum chosen from the spectrum of the previous paragraph. We will consider two such models here. The first is an independent-particle model—each nucleon in the potential well formed by the others.[67,68] Bodek and Ritchie use an entirely different model which can be described as the spectator or coherent recoil picture. In their model, the target nucleon is required to conserve energy and momentum by recoiling against an on-shell spectator nucleus with mass number $A-1$. The two models are shown in Fig. 49 for iron ($T_f \approx 36$ MeV).

To apply these Fermi-motion models to deep-inelastic scattering, we follow the work of West.[69] The starting point is the impulse approximation in which the complicated interactions within the nucleus are considered to affect things only by determining the wave function of the target nucleon, that is, the momentum spectrum and $E(p)$. Hence

$$W_{\mu\nu}^A(P^A,q)=A\int_0^\infty 4\pi p^2 dp\, f(p) W_{\mu\nu}^N(p,q)\,, \tag{B2}$$

where $W_{\mu\nu}$ is a tensor representing the square of the hadron current[8] and A and N refer to the nucleus and nucleon. Using the representation of $W_{\mu\nu}$ in terms of the structure functions $W_{1,2}$ and inspecting the 3-3 component of Eq. (B2) we find

$$W_2^A(P^A,q)=A\int_0^\infty 4\pi p^2 dp\, f(p) \times\left[\left[1+\frac{p_3 Q^2}{M_N \nu' q_3}\right]^2\left[\frac{\nu'}{\nu}\right]^2 + \frac{p_\perp{}^2 Q^2}{M_N{}^2 q_3{}^2}\right] W_2^N(p,q)\,, \tag{B3}$$

where we have chosen the 3 axis along the direction of $\mathbf{q}$, and $\nu' \equiv p\cdot q/M_N$, $\nu \equiv P^A\cdot q/M_A$. The remaining difficulty is that W_2^N in Eq. (B3) still refers to the structure function of an off-shell nucleon. That this might complicate the situation is evident. The derivation of $W_{\mu\nu}$ was based on the presence of only two relevant scalars (see Sec. I A).

Now, with $p^2 \neq M_N^2$, W_2^N can be a function not only of Q^2 and ν', but also p^2. Following Bodek and Ritchie, we identify the off-shell $W_2^N(p,q)$ with the on-shell version at the same Q^2 and invariant mass W^2. Hence

$$W_2^{N,\text{off shell}}(p,q)=F_2^N(x',Q^2)/\nu ,$$
$$Q^2=-q^2 , \tag{B4}$$
$$x'=\frac{Q^2}{2M_N\nu'+p^2-M_N^2} ,$$

where F_2^N is the standard on-shell structure function.

With $f(p)$, $E(p)$, and an assumed $F_2^N(x,Q^2)$, one can perform the integration in Eq. (B3) numerically and calculate the Fermi-motion correction defined as $F_2^N(x,Q^2)/[\frac{1}{56}F_2^{\text{Fe}}(x,Q^2)]$. The results of such a calculation are shown in Fig. 50 for the independent-particle model and our spectrum. For comparison, the dashed curves are the results of Bodek and Ritchie using the spectator model. Both calculations used the Buras-Gaemers parametrization of F_2^N as input.[37] The two calculations agree fairly well in Q^2 dependence, which is minor below $x=0.45$. However, the x dependence differs substantially above $x=0.4$. It should be noted that a calculation which neglects the effects of binding entirely, that is, with $E(p)=[(p^2+M_N^2)]^{1/2}$, yields a correction with a similar shape to those shown, but which is everywhere less than one. Applying these corrections to our measured $F_2^{\text{Fe}}(x,Q^2)/56$ before fitting resulted in the changes noted in the text. The independent-particle model yielded the smaller correction to Λ, although others have found corrections nearly as small using the model of Bodek and Ritchie.[52]

*Present address: Joseph Henry Laboratories, Princeton University, Princeton, NJ 08544.
†Present address: Motorola, Inc., Phoenix, AZ 85008.
‡Present address: CH-1211, Geneva 23, Switzerland.
§Present address: Nevis Laboratories, Irvington, NY 10533.
**Present address: Physics Department, Lawrence Livermore National Laboratory, Livermore, CA 94550.
††Present address: Bell Laboratories, Murray Hill, NJ 07974.

[1]H. Geiger and E. Marsden, Proc. R. Soc. London **A82**, 495 (1909).
[2]E. Rutherford, Philos. Mag. Ser. VI **21**, 669 (1911).
[3]H. Geiger and E. Marsden, Philos. Mag. Ser. VI **25**, 604 (1913).
[4]R. Hofstadter, Annu. Rev. Nucl. Sci. **7**, 231 (1957).
[5]E. D. Bloom *et al.*, Phys. Rev. Lett. **23**, 930 (1969); M. Breidenbach *et al.*, *ibid.* **23**, 935 (1969).
[6]J. D. Bjorken and E. A. Paschos, Phys. Rev. **185**, 1975 (1969).
[7]J. D. Bjorken and S. D. Drell, *Relativistic Quantum Mechanics* (McGraw-Hill, New York, 1964).
[8]S. D. Drell and J. D. Walecka, Ann. Phys. (N.Y.) **28**, 18 (1964).
[9]L. N. Hand, Phys. Rev. **129**, 1834 (1963).
[10]J. D. Bjorken, Phys. Rev. **179**, 1547 (1969).
[11]C. G. Callan and D. J. Gross, Phys. Rev. Lett. **22**, 156 (1969).
[12]F. E. Close, *An Introduction to Quarks and Partons* (Academic, London, 1979), p. 221.
[13]D. J. Gross and F. Wilczek, Phys. Rev. Lett. **30**, 1343 (1973); H. D. Politzer, *ibid.* **30**, 1346 (1973).
[14]M. Bace, Phys. Lett. **78B**, 132 (1978).
[15]H. D. Politzer, Phys. Rep. **14**, 129 (1974).
[16]G. Altarelli and G. Parisi, Nucl. Phys. **B126**, 298 (1977).
[17]F. J. Ynduráin, *Quantum Chromodynamics: An Introduction to the Theory of Quarks and Gluons* (Springer, New York, 1983).
[18]H. Abramowicz *et al.*, Z. Phys. C **12**, 289 (1982).
[19]T. Markiewicz, University of California Ph.D. thesis, Lawrence Berkeley Laboratory Report No. LBL-19287, 1981 (unpublished).
[20]S. L. Glashow, Nucl. Phys. **22**, 579 (1961); A. Salam and J. C. Ward, Phys. Lett. **13**, 168 (1964); S. Weinberg, Phys. Rev. Lett. **19**, 1264 (1967).
[21]P. Langacker, Phys. Rep. **72**, 185 (1981).
[22]H. Georgi and S. L. Glashow, Phys. Rev. Lett. **32**, 438 (1974).
[23]M. Goldhaber, P. Langacker, and R. Slansky, Science **210**, 851 (1980).
[24]R. M. Bionta *et al.*, Phys. Rev. Lett. **51**, 27 (1983); H. S. Park *et al.*, *ibid.* **54**, 22 (1985).
[25]B. A. Gordon *et al.*, Phys. Rev. D **20**, 2645 (1979).
[26]D. Nelson, Lawrence Berkeley Laboratory Engineering Report No. MT-260, 1977 (unpublished).
[27]D. Evans, Kerth Group Internal Report No. GIN-65, Lawrence Berkely Laboratory 1978 (unpublished).
[28]G. Gollin *et al.*, IEEE Trans. Nucl. Sci. **NS-26**, 59 (1979).
[29]B. Barish *et al.*, in *Proceedings of the Calorimeter Workshop,* edited by M. Atac (Fermilab, Batavia, IL, 1975), p. 229.
[30]A. R. Clark *et al.*, Phys. Rev. Lett. **43**, 187 (1979).
[31]A. R. Clark *et al.*, Phys. Rev. Lett. **45**, 682 (1980).
[32]A. R. Clark *et al.*, Phys. Rev. Lett. **45**, 686 (1980).
[33]A. R. Clark *et al.*, Phys. Rev. Lett. **45**, 1465 (1980).
[34]A. R. Clark *et al.*, Phys. Rev. Lett. **51**, 1826 (1983).
[35]G. D. Gollin *et al.*, Phys. Rev. D **24**, 559 (1981).
[36]M. Strovink, Kerth Group Internal Report No. GIN-100, Lawrence Berkeley Laboratory, 1978 (unpublished).
[37]A. J. Buras and K. J. F. Gaemers, Nucl. Phys. **B132**, 249 (1978).
[38]L. W. Mo and Y. S. Tsai, Rev. Mod. Phys. **41**, 205 (1969).
[39]R. H. Siemann *et al.*, Phys. Rev. Lett. **22**, 421 (1969).
[40]F. C. Shoemaker, Kerth Group Internal Report Nos. GIN-153, 1980 and GIN-155, 1980, Lawrence Berkeley Laboratory (unpublished).
[41]G. Moliére, Z. Naturforsch. **3a**, 78 (1984); H. A. Bethe, Phys. Rev. **89**, 1256 (1953).
[42]L. F. Abbott, W. B. Atwood, and R. M. Barnett, Phys. Rev. D **22**, 582 (1980).
[43]F. James and M. Roos, Comput. Phys. Commun. **10**, 343 (1975).
[44]R. M. Barnett, Phys. Rev. Lett. **48**, 1657 (1982).
[45]J. J. Aubert *et al.*, Phys. Lett. **123B**, 275 (1983).
[46]A. Bodek *et al.*, Phys. Rev. Lett. **51**, 534 (1983).
[47]R. G. Arnold *et al.*, Phys. Rev. Lett. **52**, 727 (1984).
[48]R. M. Barnett and D. Schlatter, Phys. Lett. **112B**, 475 (1982).
[49]A. Devoto *et al.*, Phys. Rev. D **27**, 508 (1983).
[50]J. J. Aubert *et al.*, Phys. Lett. **114B**, 291 (1982).
[51]H. Georgi and H. D. Politzer, Phys. Rev. D **14**, 1829 (1976).
[52]J. J. Aubert *et al.*, Phys. Lett. **105B**, 322 (1981).
[53]D. B. MacFarlane *et al.*, Z. Phys. C **26**, 1 (1984).
[54]S. Wu, in *Physics at Very High Energies,* proceedings of the SLAC Summer Institute, 1982, edited by A. Mosher (SLAC Report No. 259, 1983), and references therein.
[55]P. B. Mackenzie and G. P. Lepage, Phys. Rev. Lett. **47**, 1244

(1981).
[56]J. J. Aubert *et al.*, Phys. Lett. **121B**, 87 (1983).
[57]M. D. Mestayer *et al.*, Phys. Rev. D **27**, 285 (1983).
[58]E. Derman, Phys. Rev. D **7**, 2755 (1973).
[59]E. Commins and P. Bucksbaum, *Weak Interactions of Leptons and Quarks* (Cambridge University Press, Cambridge, 1983), pp. 343–52.
[60]C. Y. Prescott *et al.*, Phys. Lett. **77B**, 347 (1978); **84B**, 524 (1979).
[61]A. Argento *et al.*, Phys. Lett. **120B**, 245 (1983).
[62]S. M. Berman and J. R. Primack, Phys. Rev. D **9**, 2171 (1974); **10**, 3895(E) (1974).
[63]M. Strovink, internal memorandum, 1974 (unpublished).
[64]B. Hahn, D. G. Ravenhall, and R. Hofstadter, Phys. Rev. **101**, 1131 (1956).
[65]D. E. Dorfan *et al.*, Phys. Rev. Lett. **14**, 995 (1965).
[66]A. Bodek and J. L. Ritchie, Phys. Rev. D **23**, 1070 (1981); **24**, 1400 (1981).
[67]A. Bohr and B. R. Mottelson, *Nuclear Structure* (Benjamin, New York, 1969), Vol. I, p. 146.
[68]V. F. Weisskopf, Nucl. Phys. **3**, 423 (1957).
[69]G. B. West, Ann. Phys. (N.Y.) **74**, 464 (1972).